COPERNICUS SPACE COMPONENT SENTINEL OPTICAL IMAGING

MISSION PERFORMANCE CLUSTER SERVICE

Data Quality Report

Sentinel-3 OLCI

January 2024

Ref.: OMPC.ACR.DQR.03.01-2024
Issue: 1.0
Date: 09/02/2024
Contract: 4000136252/21/I-BG

Customer:	ESA	Document Ref.:	OMPC.ACR.DQR.03.01-2024
Contract No.:	4000136252/21/I-BG	Date:	09/02/2024
		Issue:	1.0

Project:	COPERNICUS SPACE COMPONENT SENTINEL OPTICAL IMAGING MISSION PERFORMANCE CLUSTER SERVICE		
Title:	Data Quality Report - OLCI		
Author(s):	OLCI ESL team		
Approved by:	L. Bourg, OPT-MPC OLCI ESL Coordinator S. Clerc, OPT-MPC Optical ESL Coordinator	Authorized by	C. Hénocq, OPT-MPC S3 Technical Manager
Distribution:	ESA, EUMETSAT, published in Sentinel Online		
Accepted by ESA	S. Dransfeld, ESA TO		
Filename	OMPC.ACR.DQR.03.01-2024 - i1r0 - OLCI DQR January 2024.docx		

Changes Log

Version	Date	Changes
1.0	09/02/2024	First version

List of Changes

Version	Section	Answers to RID	Changes

Table of content

TABLE OF CONTENT ..... **IV**
LIST OF FIGURES ..... **VI**
LIST OF TABLES ..... **XII**
1 PROCESSING BASELINE VERSION **1**
1.1 Sentinel3-A 1
1.2 Sentinel3-B 1
2 INSTRUMENT MONITORING **2**
2.1 CCD temperatures 2
2.1.1 OLCI-A 2
2.1.2 OLCI-B 4
2.2 Radiometric Calibration 5
2.2.1 Dark Offsets [OLCI-L1B-CV-230] 8
2.2.3 Instrument response and degradation modelling [OLCI-L1B-CV-250] 18
2.2.4 Ageing of nominal diffuser [OLCI-L1B-CV-240] 36
2.2.5 Updating of calibration ADF [OLCI-L1B-CV-260] 36
2.3 Spectral Calibration [OLCI-L1B-CV-400] 36
2.3.1 OLCI-A 36
2.3.2 OLCI-B 37
2.4 Signal to Noise assessment [OLCI-L1B-CV-620] 37
2.4.1 SNR from Radiometric calibration data 37
2.5 Geometric Calibration/Validation 44
2.5.1 OLCI-A 44
2.5.2 OLCI-B 47
3 OLCI LEVEL 1 PRODUCT VALIDATION **51**
3.1 [OLCI-L1B-CV-300], [OLCI-L1B-CV-310] – Radiometric Validation 51
3.1.1 S3ETRAC Service 51
3.1.2 Radiometric validation with DIMITRI 53
3.1.3 Radiometric validation with OSCAR 59
3.1.4 Radiometric validation with Moon observations: LIME results 63
4 LEVEL 2 LAND PRODUCTS VALIDATION **64**
4.1 [OLCI-L2LRF-CV-300] 64
4.1.1 Routine extractions 64
4.1.2 Comparison with MERIS MTCI Climatology 74
4.1.3 Comparison with GBOV (Ground-Based Observations for Validation) data v3 78
4.1.4 Sentinel-3A and 3B biophysical variables inter-annual variability results 78
4.2 [OLCI-L2LRF-CV-410 & OLCI-L2LRF-CV-420] – Cloud Masking & Surface Classification for Land Products 78

5 VALIDATION OF INTEGRATED WATER VAPOUR OVER LAND & WATER 79

6 LEVEL 2 SYN PRODUCTS VALIDATION 81

6.1 SYN L2 SDR products 81

6.2 SY_2_VGP, SY_2_VG1 and SY_2_V10 products 81

6.3 SYN L2 AOD NTC products 85

7 EVENTS 90

8 APPENDIX A 91

List of Figures

Figure 1: long term monitoring of OLCI-A CCD temperatures using minimum value (top), time averaged values (middle), and maximum value (bottom) provided in the annotations of the Radiometric Calibration Level 1 products, for the shutter frames, all radiometric calibrations so far except the first one (absolute orbit 183) for which the instrument was not yet thermally stable. ---- 2

Figure 2: Same as Figure 1 for diffuser frames. ---- 3

Figure 3: long term monitoring of OLCI-B CCD temperatures using minimum value (top), time averaged values (middle), and maximum value (bottom) provided in the annotations of the Radiometric Calibration Level 1 products, for the Shutter frames, all radiometric calibrations so far except the first one (absolute orbit 167) for which the instrument was not yet thermally stable. ---- 4

Figure 4: same as Figure 3 for diffuser frames. ---- 5

Figure 5: Sun azimuth angles during acquired OLCI-A Radiometric Calibrations (diffuser frame) on top of nominal yearly cycle (black curve). Diffuser 1 with diamonds, diffuser 2 with crosses. Different colours correspond to different years of acquisition (see the legend inside the figure). ---- 6

Figure 6: same as Figure 5 for OLCI-B. ---- 6

Figure 7: OLCI-A Sun geometry during radiometric Calibrations on top of characterization ones (diffuser frame) ---- 7

Figure 8: same as Figure 7 for OLCI-B ---- 7

Figure 9: Dark Offset table for band Oa06 with (red) and without (black) HEP filtering (Radiometric Calibration of 22 July 2017). The strong HEP event near pixel 400 has been detected and removed by the HEP filtering. ---- 8

Figure 10: OLCI-A Dark Offset for band Oa1 (top) and Oa21 (bottom), all radiometric calibrations so far except the first one (orbit 183) for which the instrument was not thermally stable yet. ---- 9

Figure 11: map of OLCI-A periodic noise for the 5 cameras, for band Oa21. X-axis is detector number (East part, from 540 to 740, where the periodic noise occurs), Y-axis is the orbit number. Y-axis range is focused on the most recent 5000 orbits. The counts have been corrected from the West detectors mean value (not affected by periodic noise) in order to remove mean level gaps and consequently to have a better visualisation of the long term evolution of the periodic noise structure. At the beginning of the mission the periodic noise for band Oa21 had strong amplitude in camera 2, 3 and 5 compared to camera 1 and 4. However PN evolved through the mission and these discrepancies between cameras have been reduced. At the time of this Cyclic Report Camera 2 still shows a slightly higher PN than other cameras. ---- 10

Figure 12: same as Figure 11 for smear band. ---- 11

Figure 13: OLCI-A Dark Current for band Oa1 (top) and Oa21 (bottom), all radiometric calibrations so far except the first one (orbit 183) for which the instrument was not thermally stable yet. ---- 12

Figure 14: left column: ACT mean on 400 first detectors of OLCI-A Dark Current coefficients for spectral band Oa01 (top) and Oa21 (bottom). Right column: same as left column but for Standard deviation instead of mean. We see an increase of the DC level as a function of time especially for band Oa21. ---- 12

Figure 15: OLCI-A Dark current increase rates with time (in counts per year) vs. band (left) and vs. band width (right) ---- 13

Figure 16: OLCI-B Dark Offset for band Oa1 (top) and Oa21 (bottom), all radiometric calibrations so far except the first one (orbit 167) for which the instrument was not thermally stable yet. ---- 14

Figure 17: OLCI-B map of periodic noise for the 5 cameras, for band Oa21. X-axis is detector number (East part, from 540 to 740, where the periodic noise occurs), Y-axis is the orbit number. The counts have been corrected from the West detectors mean value (not affected by periodic noise) in order to remove mean level gaps and consequently to have a better visualization of the long term evolution of the periodic noise structure. ---- 15

Figure 18: same as Figure 17 for smear band. ---- 15

Figure 19: OLCI-B Dark Current for band Oa1 (top) and Oa21 (bottom), all radiometric calibrations so far except the first one (orbit 167) for which the instrument was not thermally stable yet. ---- 16

Figure 20: left column: ACT mean on 400 first detectors of OLCI-B Dark Current coefficients for spectral band Oa01 (top) and Oa21 (bottom). Right column: same as left column but for Standard deviation instead of mean. We see an increase of the DC level as a function of time especially for band Oa21. ---- 17

Figure 21: OLCI-B Dark Current increase rates with time (in counts per year) vs. band (left) and vs. band width (right) ---- 17

Figure 22: OLCI-A Gain Coefficients for band Oa1 (top) and Oa21 (bottom), derived using the in-flight BRDF model. The dataset is made of all diffuser 1 radiometric calibrations since orbit 979. ---- 18

Figure 23: camera averaged gain relative evolution with respect to calibration of 25/04/2016 (change of OLCI channel settings), as a function of elapsed time since the beginning of the mission; one curve for each band (see colour code on plots), one plot for each module. The diffuser ageing is taken into account.-- 19

Figure 24: OLCI-B Gain Coefficients for band Oa1 (top) and Oa21 (bottom), derived using the in-flight BRDF model. The dataset is made of all diffuser 1 radiometric calibrations since orbit 758. ---- 20

Figure 25: OLCI-B camera averaged gain relative evolution with respect to first calibration after channel programming change (18/06/2018), as a function of elapsed time since the beginning of the mission; one curve for each band (see colour code on plots), one plot for each module. The diffuser ageing is taken into account. ---- 21

Figure 26: RMS performance of the OLCI-A Gain Model of the current processing baseline as a function of orbit. ---- 23

Figure 27: RMS performance of the OLCI-A Gain Model of the previous Processing Baseline as a function of orbit. ---- 23

Figure 28: OLCI-A Camera-averaged instrument evolution since channel programming change (25/04/2016) and up to the most recent calibration (26/01/2024) versus wavelength. ---- 24

Figure 29: For the 5 cameras: OLCI-A Evolution model performance, as camera-average and standard deviation of ratio of Model over Data vs. wavelength, for each orbit of the test dataset, including 14 calibrations in extrapolation, with a colour code for each calibration from blue (oldest) to red (most recent). ---- 25

Figure 30: OLCI-A evolution model performance, as ratio of Model over Data vs. pixels, all cameras side by side, over the whole current calibration dataset (since instrument programming update), including 14 calibrations in extrapolation, channels Oa1 to Oa6. ---- 26

Figure 31: same as Figure 30 for channels Oa7 to Oa14. ---- 27

Figure 32: same as Figure 30 for channels Oa15 to Oa21. ---- 28

Figure 33: RMS performance of the OLCI-B Gain Model of the current processing baseline as a function of orbit. ---- 29

Figure 34: RMS performance of the OLCI-B Gain Model of the previous processing baseline as a function of orbit (please note the different vertical scale with respect to Figure 33).------------------------------------ 30

Figure 35: OLCI-B Camera-averaged instrument evolution since channel programming change (18/06/2018) and up to most recent calibration (13/01/2024) versus wavelength. -------------------------- 31

Figure 36: For the 5 cameras: OLCI-B Evolution model performance, as camera-average and standard deviation of ratio of Model over Data vs. wavelength, for each orbit of the test dataset, including 13 calibrations in extrapolation, with a colour code for each calibration from blue (oldest) to red (most recent). -- 32

Figure 37: OLCI-B evolution model performance, as ratio of Model over Data vs. pixels, all cameras side by side, over the whole current calibration dataset (since instrument programming update), including 13 calibrations in extrapolation, channels Oa1 to Oa6. -- 33

Figure 38: same as Figure 37 for channels Oa7 to Oa14. -- 34

Figure 39: same as for channels Oa15 to Oa21.--- 35

Figure 40: OLCI-A Signal to Noise ratio as a function of the spectral band for the 5 cameras. These results have been computed from radiometric calibration data. All calibrations except first one (orbit 183) are presents with the colours corresponding to the orbit number (see legend). The SNR is very stable with time: the curves for all orbits are almost superimposed. The dashed curve is the ESA requirement.----- 38

Figure 41: long-term stability of the SNR estimates from Calibration data, example of channel Oa1. ---- 39

Figure 42: OLCI-B Signal to Noise ratio as a function of the spectral band for the 5 cameras. These results have been computed from radiometric calibration data. All calibrations except first one (orbit 167) are presents with the colours corresponding to the orbit number (see legend). The SNR is very stable with time: the curves for all orbits are almost superimposed. The dashed curve is the ESA requirement.----- 41

Figure 43: long-term stability of the OLCI-B SNR estimates from Calibration data, example of channel Oa1. --- 42

Figure 44: overall OLCI-A georeferencing RMS performance time series (left) and number of validated control points corresponding to the performance time series (right) over the whole monitoring period 44

Figure 45: across-track (left) and along-track (right) OLCI-A georeferencing biases time series for Camera 1. Blue line is the average, black lines are average plus and minus 1 sigma.------------------------------------ 45

Figure 46: same as Figure 45 for Camera 2. -- 45

Figure 47: same as Figure 45 for Camera 3. -- 45

Figure 48: same as Figure 45 for Camera 4. -- 46

Figure 49: same as Figure 45 for Camera 5. -- 46

Figure 50: OLCI-A spatial across-track misregistration at each camera transition (left) and maximum amplitude of the across-track error within each camera (left). --- 46

Figure 51: OLCI-A spatial along-track misregistration at each camera transition (left) and maximum amplitude of the along-track error within each camera (left). -- 47

Figure 52: overall OLCI-B georeferencing RMS performance time series over the whole monitoring period (left) and corresponding number of validated control points (right)--- 47

Figure 53: across-track (left) and along-track (right) OLCI-B georeferencing biases time series for Camera 1. --- 48

Figure 54: same as Figure 53 for Camera 2. -- 48

Figure 55: same as Figure 53 for Camera 3. ---- 48

Figure 56: same as Figure 53 for Camera 4. ---- 49

Figure 57: same as Figure 53 for Camera 5. ---- 49

Figure 58: OLCI-B spatial across-track misregistration at each camera transition (left) and maximum amplitude of the across-track error within each camera (left). ---- 49

Figure 59: OLCI-B spatial along-track misregistration at each camera transition (left) and maximum amplitude of the along-track error within each camera (left). ---- 50

Figure 60: summary of S3ETRAC products generation for OLCI-A (number of OLCI-A L1 products Ingested, blue – number of S3ETRAC extracted products generated, green – number of S3ETRAC runs without generation of output product (data not meeting selection requirements), yellow – number of runs ending in error, red, one plot per site type). ---- 52

Figure 61: summary of S3ETRAC products generation for OLCI-B (number of OLCI-B L1 products Ingested, yellow – number of S3ETRAC extracted products generated, blue – number of S3ETRAC runs without generation of output product (data not meeting selection requirements), green – number of runs ending in error, red, one plot per site type). ---- 53

Figure 62: Time-series of the elementary ratios (observed/simulated) signal from OLCI-A for (top to bottom) bands Oa03 and Oa17 respectively over January 2024 from the six PICS Cal/Val sites. Dashed-green and orange lines indicate the 2% and 5% respectively. Error bars indicate the desert methodology uncertainty. ---- 54

Figure 63: Time-series of the elementary ratios (observed/simulated) signal from OLCI-B for (top to bottom) bands Oa08 and Oa17 respectively over January 2024 from the six PICS Cal/Val sites. Dashed-green and orange lines indicate the 2% and 5% respectively. Error bars indicate the desert methodology uncertainty. ---- 55

Figure 64: The estimated gain values for OLCI-A and OLCI-B over the 6 PICS sites identified by CEOS over the period January 2024 as a function of wavelength. Dashed-green and orange lines indicate the 2% and 5% respectively. Error bars indicate the desert methodology uncertainty. ---- 56

Figure 65: The estimated gain values for OLCI-A and OLCI-B from Glint, Rayleigh and PICS methods over the period January 2022 – end December 2023 as a function of wavelength. We use the gain value of Oa8 from PICS-Desert method as reference gain for Glint method. Dashed-green and orange lines indicate the 2% and 5% respectively. Error bars indicate the method uncertainties. ---- 57

Figure 66: Ratio of observed TOA reflectance to simulated one for (black) MERIS, (pale-green) S2A/MSI, (white) S2B/MSI, (blue) S3A/OLCI, (green) S3B/OLCI, (red) S3A/SLSTR-NADIR, and (cyan) S3B/SLSTR-NADIR averaged over the six PICS test sites over different periods as a function of wavelength. ---- 58

Figure 67: OSCAR Rayleigh S3A and S3B Calibration results as a function of wavelength for January 2024. The results are obtained with a new climatology derived from CMEMS OLCI monthly CHL products. ---- 60

Figure 68: OSCAR Rayleigh OLCI-A and OLCI-B Calibration results as a function of wavelength for all acquisitions of 2023 and January 2024. The results are obtained with a new climatology derived from CMEMS OLCI monthly CHL products. ---- 60

Figure 69: OSCAR Glitter OLCI-A & OLCI-B Calibration results as a function of wavelength for December 2023. The results are obtained with a new climatology derived from CMEMS OLCI monthly CHL products. ---- 62

Figure 70: OSCAR Glitter OLCI-A & OLCI-B Calibration results as a function of wavelength for all acquisitions of 2023. The results are obtained with a new climatology derived from CMEMS OLCI monthly CHL products. ---- 62
Figure 71: DeGeb time series over current report period ---- 64
Figure 72: ITCat time series over current report period ---- 65
Figure 73: ITIsp time series over current report period ---- 65
Figure 74: ITSro time series over current report period ---- 66
Figure 75: ITTra time series over current report period ---- 66
Figure 76: SPAli time series over current report period ---- 67
Figure 77: UKNFo time series over current report period ---- 67
Figure 78: USNe1 time series over current report period ---- 68
Figure 79: USNe2 time series over current report period ---- 68
Figure 80: USNe3 time series over current report period ---- 69
Figure 81: DeGeb time series over current report period ---- 69
Figure 82: ITCat time series over current report period ---- 70
Figure 83: ITIsp time series over current report period ---- 70
Figure 84: ITSro time series over current report period ---- 71
Figure 85: ITTra time series over current report period ---- 71
Figure 86: SPAli time series over current report period ---- 72
Figure 87: UKNFo time series over current report period ---- 72
Figure 88: USNe1 time series over current report period ---- 73
Figure 89: USNe2 time series over current report period ---- 73
Figure 90: USNe3 time series over current report period ---- 74
Figure 91: Time series (left) of GIFAPAR and MGVI and a corresponding scatterplot of the monthly mean for site Barlett and Konza (representing S3A) and Aurade and Warra Tall (representing S3B). The climatology of MERIS FAPAR (black and grey colours) is compared against 2023 (blue colours) and 2024(red colours). ---- 76
Figure 92: Time series (left) of OTCI and MTCI and a corresponding scatterplot of the monthly mean for sites Brasschaat and Cape Tribulation (representing S3A), and Smithsonian Environmental and Litchfield (representing S3B). The climatology of MERIS MTCI (black and grey colours) is compared against 2023 (blue colours) and 2024 (red colours). ---- 77
Figure 93: Upper: Scatter plot of the IWV products, derived from OLCI (A left, B right) above land and from SUOMI NET GNSS measurements. Middle: Histogram of the difference between OLCI (A: left, B: right) and GNSS (blue: original OLCI, orange: bias corrected OLCI). Lower: Positions of the GNSS (A: left, B: right). 80
Figure 94: Temporal evolution of different quality measures for OLCI A (left) and OLCI B (right) with respect to SUOMI Net. From top to bottom: systematic deviation factor, bias, root mean squared difference (with and without bias correction), explained variance (number in boxes are the numbers of matchups)------ 80
Figure 95: Scatter density plots between SY_V10 S3A (top) or S3B (bottom) and PROBA-V C2 S10-TOC for BLUE, RED, NIR and SWIR bands (left to right), January/2024 vs. January/2020 ---- 82

Figure 96: Temporal evolution of APU statistics between SY_2_V10 S3A (left) or S3B (right) and PROBA-V S10-TOC for BLUE, RED, NIR and SWIR bands (top to bottom), January/2021 – January/2024 (S3 SYN VGT) vs. January/2017 – January/2020 (PROBA-V) ---------- 83

Figure 97: Temporal evolution of APU statistics between S3A_SY_2_V10 and S3B_SY_2_V10 for BLUE, RED, NIR and SWIR bands (top to bottom), January/2021 – January/2024 ---------- 84

Figure 98: Histogram of number of satellite pixels in FMI matchups (±0.25°) with AERONET, for August 2023 ---------- 85

Figure 99: Histogram of valid satellite pixels retrieved in FMI matchup (+- 0.25°) area. For August 2023 85

Figure 100: Dependence of validation results on minimum number of required Sy_2 ADO pixels (minNpix in each figure title) around AERONET matchup. For 2020, Aug-Dec, FMI matchups. Note that density (number of matchups per bin) is shown in logarithmic scale. Validation statistics are provided (offset and slope from the linear fit, N – number of matchups, r – correlation coefficient, σ- standard deviation, rms – root mean square error, EE – number of pixels in the MODFIS error envelope defined as ±0.05±0.2*AOD, GCOS – fraction of matchups which satisfy GCOS requirements of 0.03 or 10% of AOD).---------- 87

Figure 101: Scatter density plots for syAOD vs aAOD for years 2020, 2021 and 2023, months Aug-Dec. Note that density (number of matchups per bin) is shown in logarithmic scale. Validation statistics are provided (offset and slope from the linear fit, N – number of matchups, r – correlation coefficient, σ- standard deviation, rms – root mean square error, EE – number of pixels in the MODFIS error envelope defined as ±0.05±0.2*AOD, GCOS – fraction of matchups which satisfy GCOS requirements of 0.03 or 10% of AOD). ---------- 88

Figure 102: For Aug-Dec of 2020 (red), 2021 (blue) and 2023 (green), Sy AOD offsets (dAOD, binned to Aeronet AOD, aAOD) for matchups created by FMI. Left : results for aAOD∈ [0, 0.65]. Right : aAOD∈ [0, 2.5]. ---------- 89

List of Tables

Table 1: OLCI-A SNR figures as derived from Radiometric Calibration data. Figures are given for each camera (time average and standard deviation), and for the whole instrument. The requirement and its reference radiance level are recalled (in $mW.sr^{-1}.m^{-2}.nm^{-1}$). ---------- 40

Table 2: OLCI-B SNR figures as derived from Radiometric Calibration data. Figures are given for each camera (time average and standard deviation), and for the whole instrument. The requirement and its reference radiance level are recalled (in $mW.sr^{-1}.m^{-2}.nm^{-1}$). ---------- 43

Table 3: S3ETRAC Rayleigh Calibration sites ---------- 59

Table 4. OSCAR Rayleigh calibration results for S3A and S3B (average and standard deviation over all 2023 acquisitions and 2024) over all scenes currently (re)processed with the new climatology and observed difference (in %) between OLCIA and OLCIB ---------- 61

Table 5: OSCAR Glitter calibration results for OLCI-A and OLCI-B (average and standard deviation over all acquisitions of 2023) currently processed with the new climatology and observed difference (in %) ---- 63

Table 6: S3VT, CEOS and GBOV validation sites analysed. ---------- 75

1 Processing Baseline Version

1.1 Sentinel3-A

IPF	IPF / Processing Baseline version	Date of deployment
OL1	06.17 / OL__L1_.003.03.01 (with uncertainties activated)	16/10/2023
OL2 LAND	06.18 / OL__L2L.002.11.02	25/07/2023
SY2	06.25 / SYN_L2_.002.18.01	25/07/2023
SY2_VGS	06.12 / SYN_L2V.002.09.01	25/07/2023
SY2_AOD	01.08 / AOD_NTC.002.08.01	25/07/2023

1.2 Sentinel3-B

IPF	IPF / Processing Baseline version	Date of deployment
OL1	06.17 / OL__L1_.003.03.01 (with uncertainties activated)	24/10/2023
OL2 Land	06.18 / OL__L2L.002.11.02	18/07/2023
SY2	06.25 / SYN_L2_.002.18.01	18/07/2023
SY2_VGS	06.12 / SYN_L2V.002.09.01	18/07/2023
SY2_AOD	01.08 / AOD_NTC.002.08.01	18/07/2023

2 Instrument monitoring

2.1 CCD temperatures

2.1.1 OLCI-A

The long-term monitoring of the CCD temperatures is based on Radiometric Calibration Annotations (see Figure 1). Variations are very small (0.09 C peak-to-peak) and no trend can be identified. Data from current reporting period (rightmost data points) do not show any specificity.

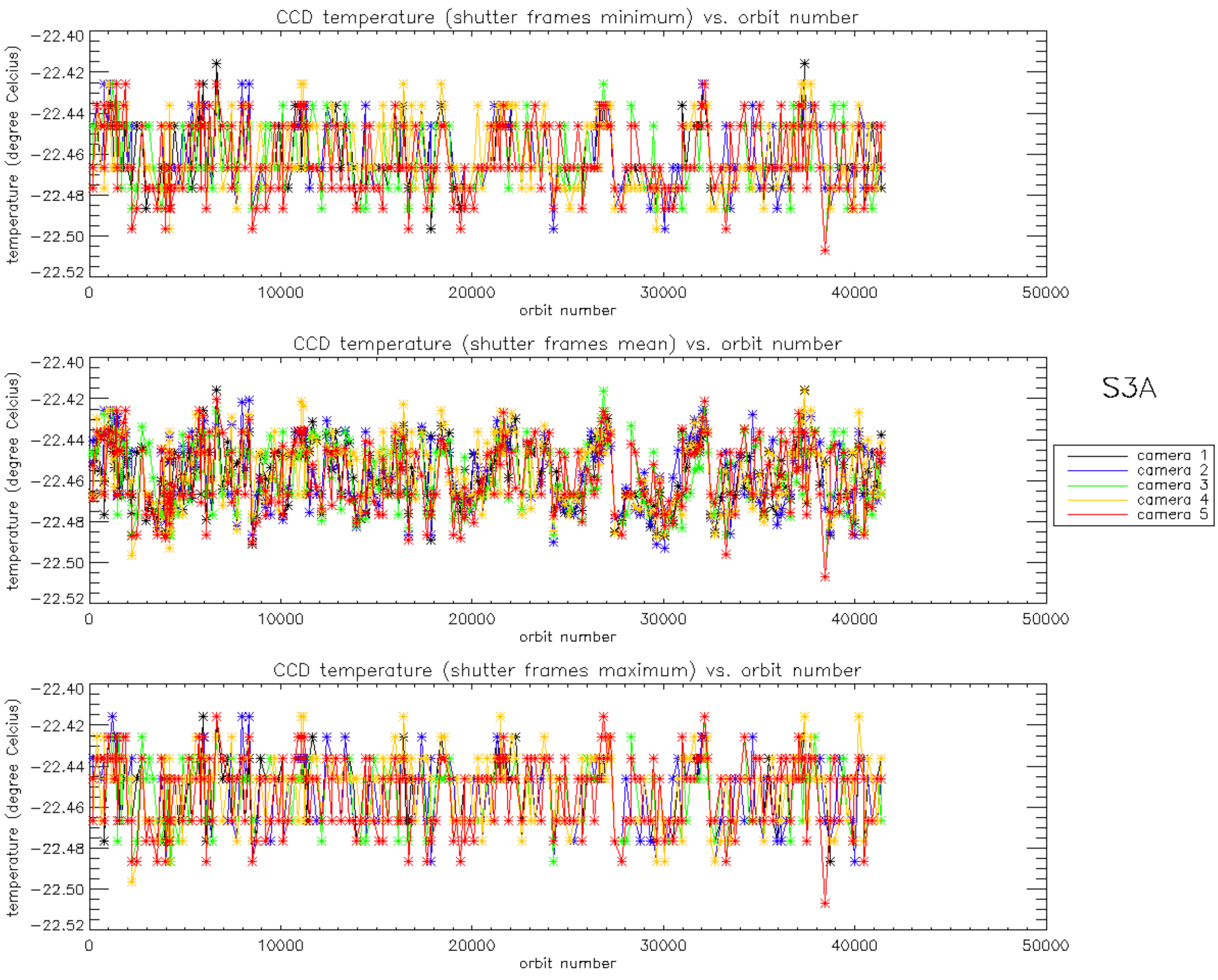

Figure 1: long term monitoring of OLCI-A CCD temperatures using minimum value (top), time averaged values (middle), and maximum value (bottom) provided in the annotations of the Radiometric Calibration Level 1 products, for the shutter frames, all radiometric calibrations so far except the first one (absolute orbit 183) for which the instrument was not yet thermally stable.

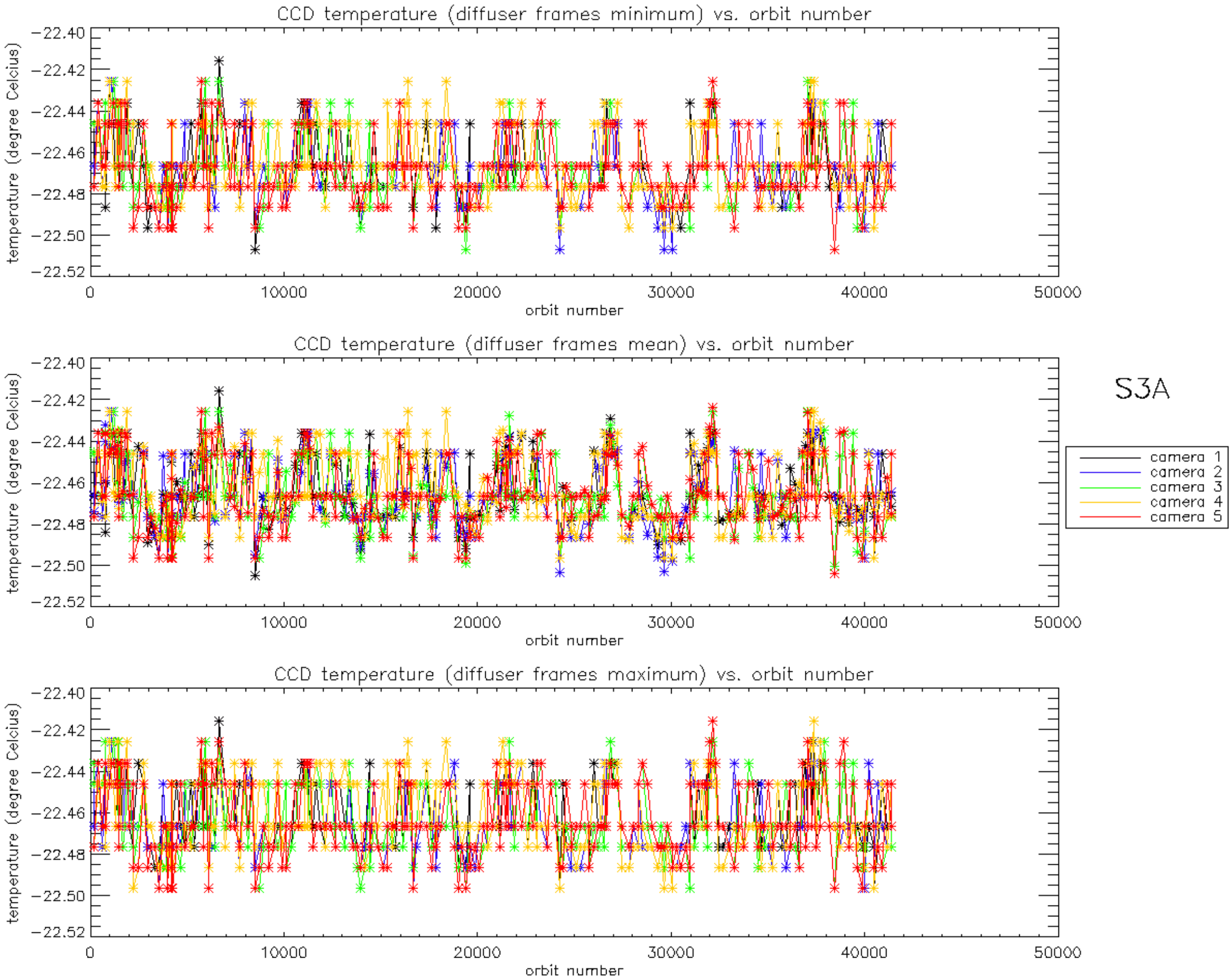

Figure 2: Same as Figure 1 for diffuser frames.

2.1.2 OLCI-B

As for OLCI-A, the variations of CCD temperature are very small (0.08 C peak-to-peak) and no trend can be identified. Data from current reporting period (rightmost data points) do not show any specificity.

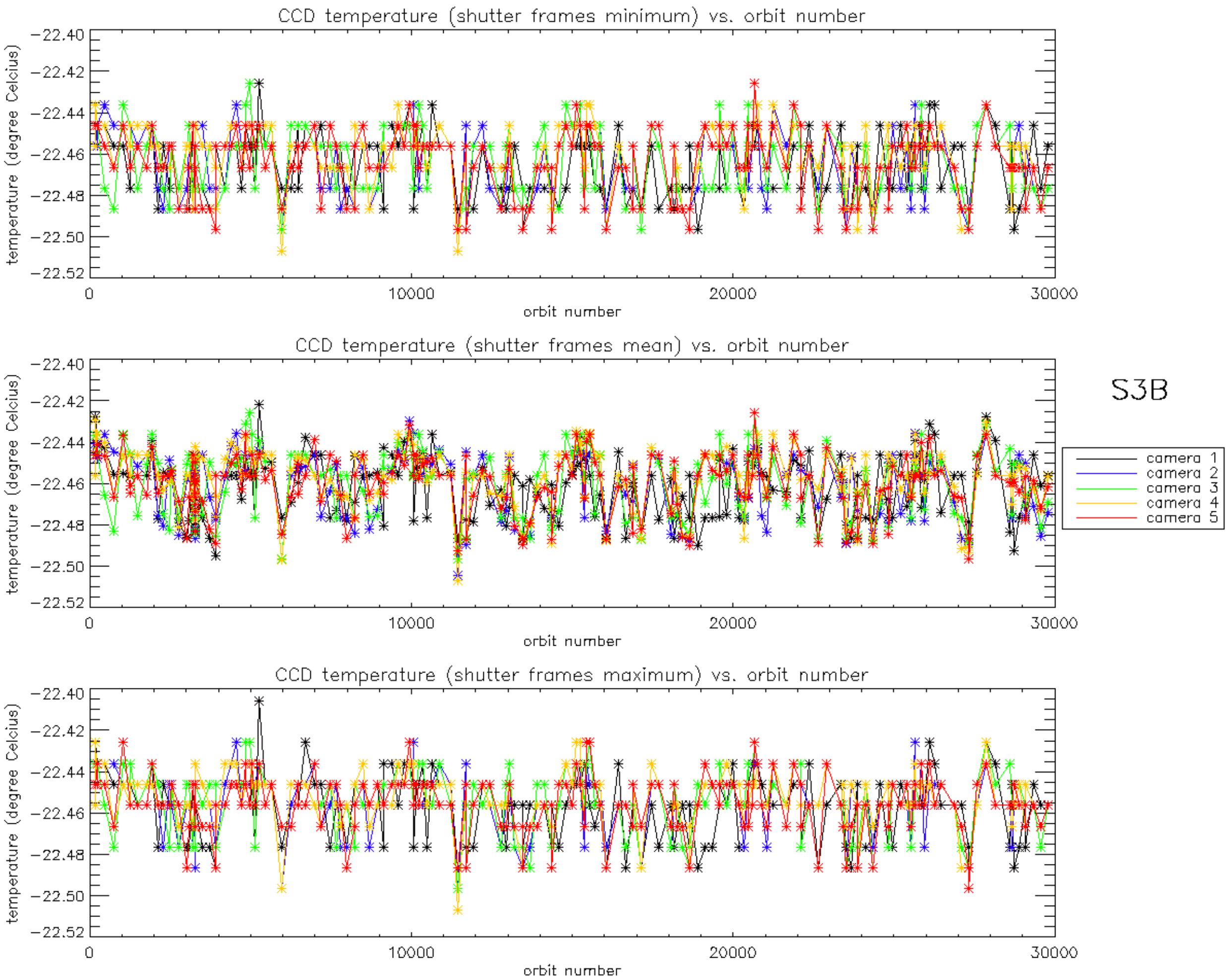

Figure 3: long term monitoring of OLCI-B CCD temperatures using minimum value (top), time averaged values (middle), and maximum value (bottom) provided in the annotations of the Radiometric Calibration Level 1 products, for the Shutter frames, all radiometric calibrations so far except the first one (absolute orbit 167) for which the instrument was not yet thermally stable.

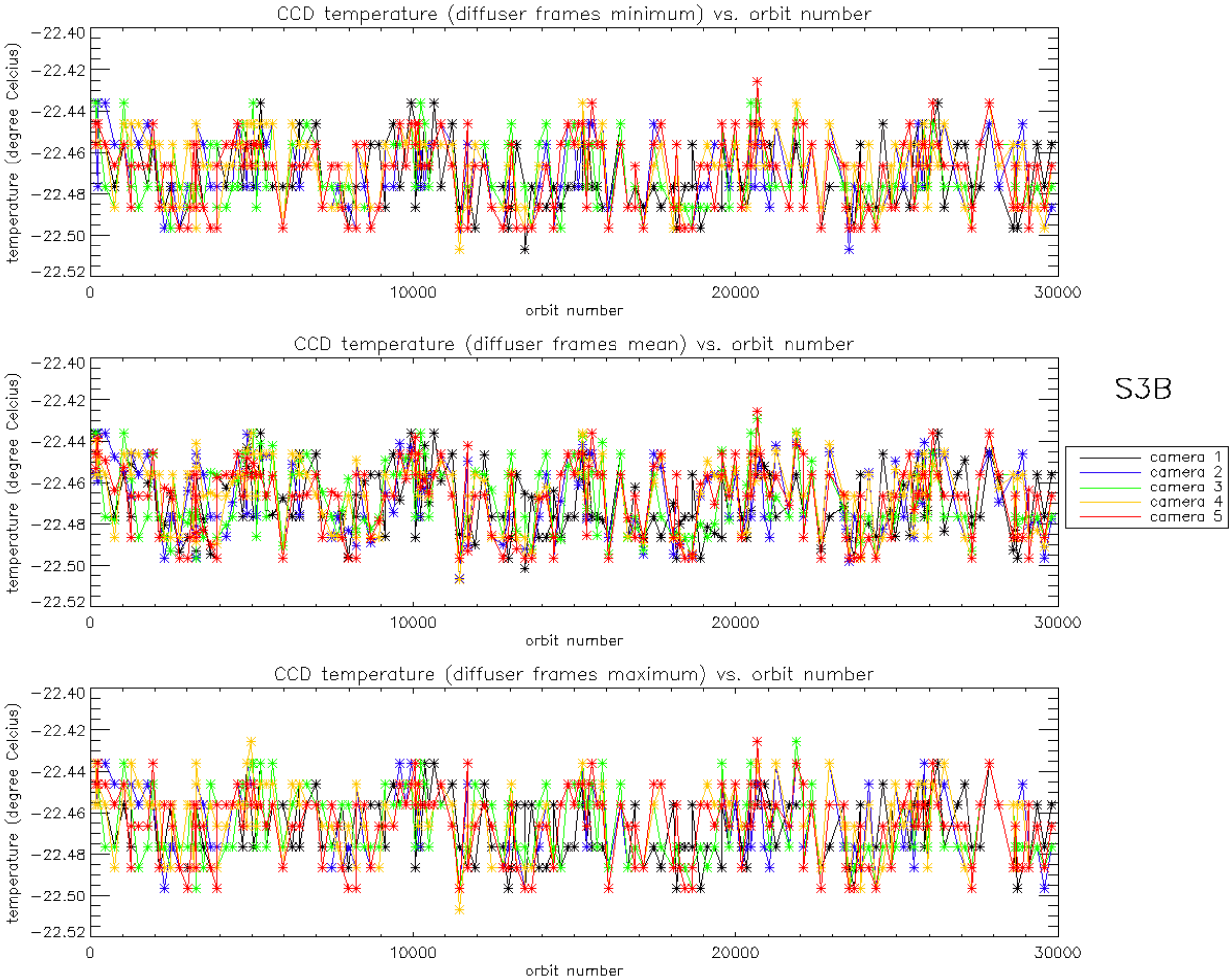

Figure 4: same as Figure 3 for diffuser frames.

2.2 Radiometric Calibration

For OLCI-A, three Radiometric Calibration sequences have been acquired during the reported period:

- S01 sequence (diffuser 1) on 11/01/2024 20:21 to 20:22 (absolute orbit 41153)
- S01 sequence (diffuser 1) on 26/01/2024 13:47 to 13:49 (absolute orbit 41363)
- S05 sequence (diffuser 5) on 26/01/2024 15:28 to 15:30 (absolute orbit 41364)

For OLCI-B, one Radiometric Calibration sequence has been acquired during the reported period:

- S01 sequence (diffuser 1) on 13/01/2024 15:27 to 15:29 (absolute orbit 29785)

The acquired Sun azimuth angles are presented on Figure 5 for OLCI-A and Figure 6 for OLCI-B, on top of the nominal values without Yaw Manoeuvre (i.e. with nominal Yaw Steering control of the satellite).

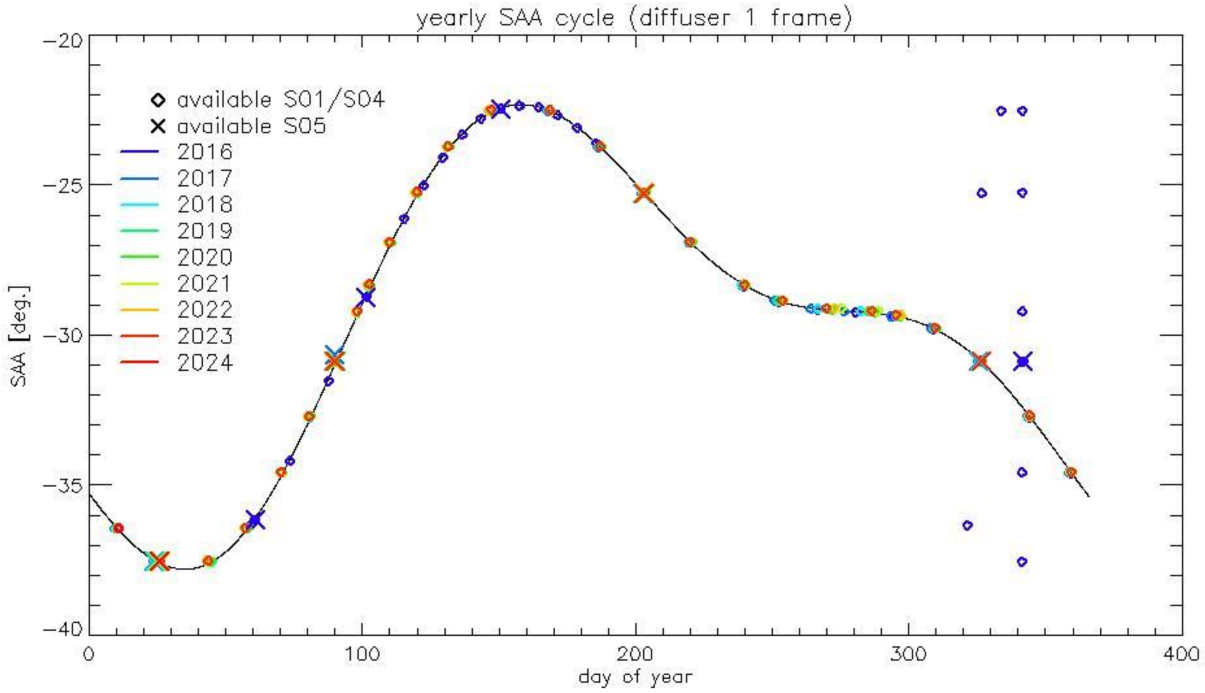

Figure 5: Sun azimuth angles during acquired OLCI-A Radiometric Calibrations (diffuser frame) on top of nominal yearly cycle (black curve). Diffuser 1 with diamonds, diffuser 2 with crosses. Different colours correspond to different years of acquisition (see the legend inside the figure).

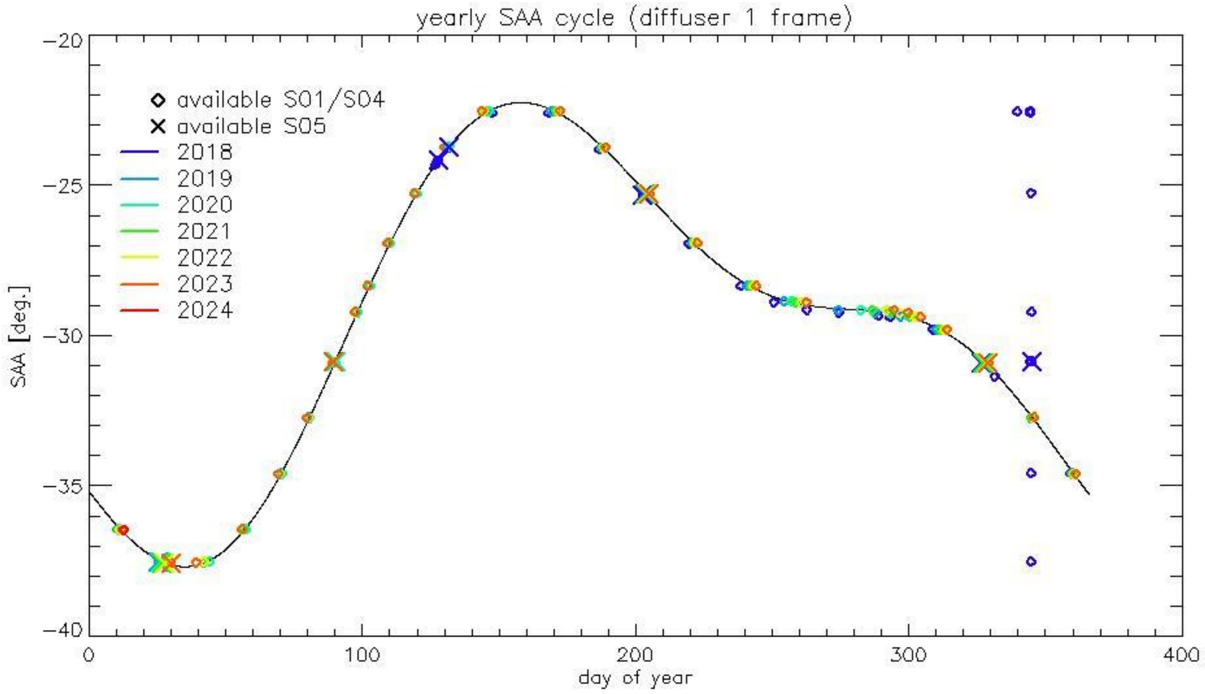

Figure 6: same as Figure 5 for OLCI-B.

Sun Zenith Angles as a function of Sun Azimuth Angles are presented in Figure 7 for OLCI-A and Figure 8 for OLCI-B.

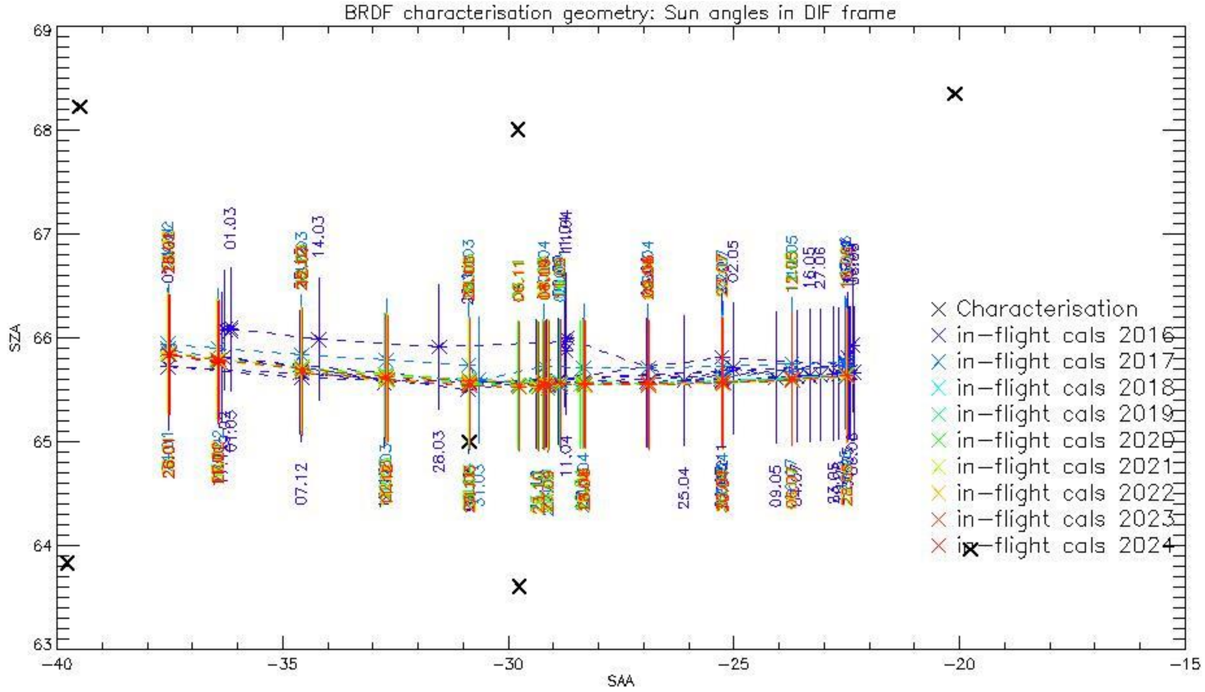

Figure 7: OLCI-A Sun geometry during radiometric Calibrations on top of characterization ones (diffuser frame)

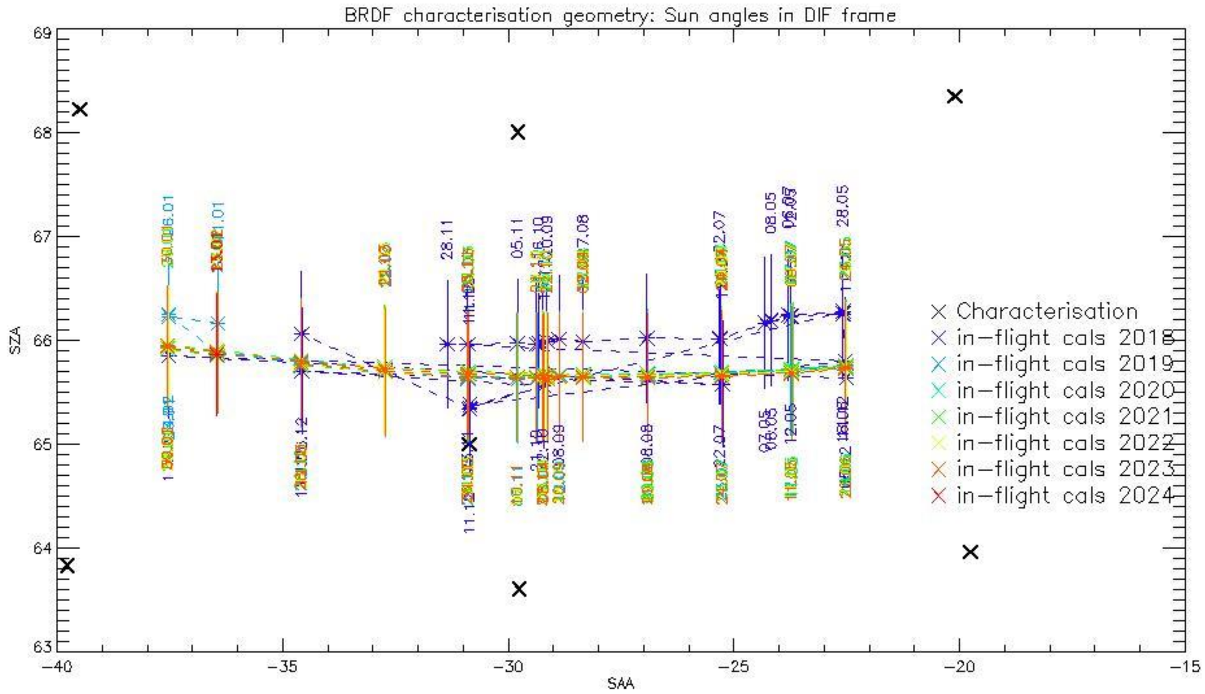

Figure 8: same as Figure 7 for OLCI-B

2.2.1 Dark Offsets [OLCI-L1B-CV-230]

Note about the High Energy Particles:

The filtering of High Energy Particle (HEP) events from radiometric calibration data has been implemented (for shutter frames only) in a post processor, allowing generating Dark Offset and Dark Current tables computed on filtered data. The post-processor starts from IPF intermediate data (corrected counts), applies the HEP detection and filtering and finally computes the Dark Offset and Dark Current tables the same way as IPF. An example of the impact of HEP filtering is given in Figure 9.

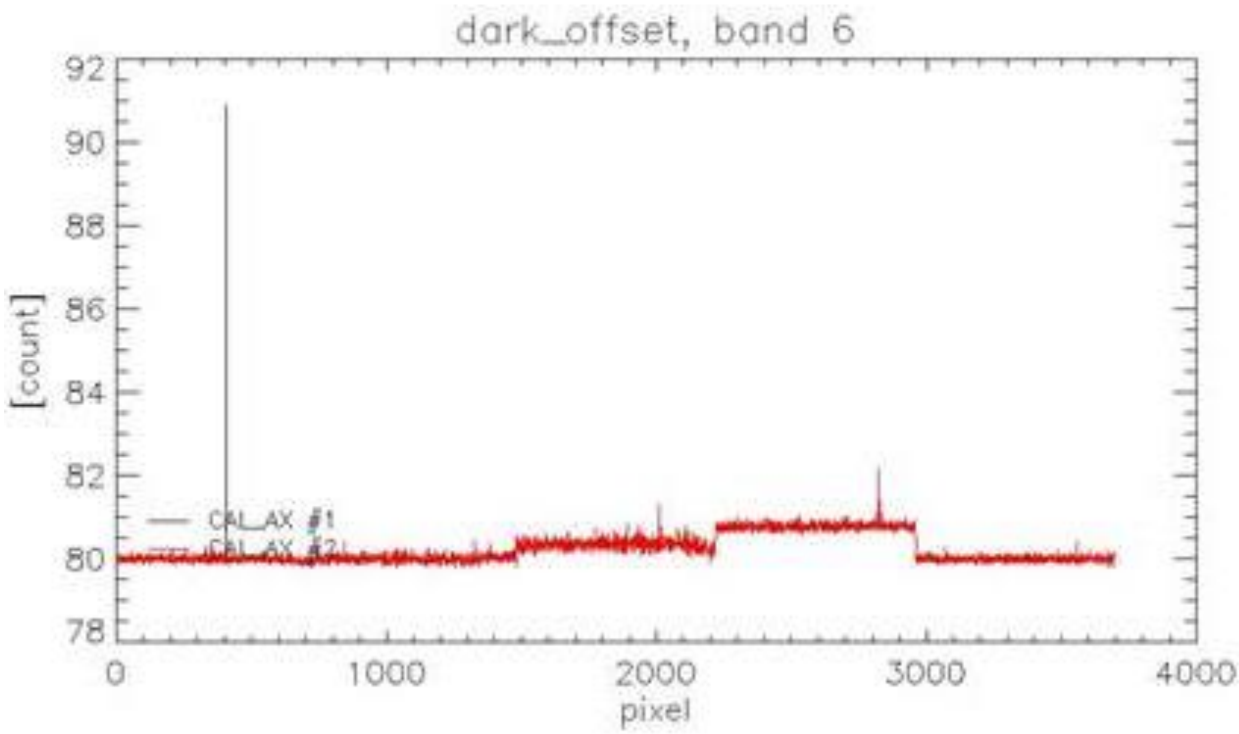

Figure 9: Dark Offset table for band Oa06 with (red) and without (black) HEP filtering (Radiometric Calibration of 22 July 2017). The strong HEP event near pixel 400 has been detected and removed by the HEP filtering.

All results presented below in this section have been obtained using the HEP filtered Dark Offset and Dark Current tables.

2.2.1.2 OLCI-A

Dark offsets

Dark offsets are continuously affected by the global offset induced by the Periodic Noise on the OCL (Offset Control Loop) convergence. Current reporting period calibrations are affected the same way as others. The amplitude of the shift varies with band and camera from virtually nothing (e.g. camera 2, band 0a1) to up to 5 counts (Oa21, camera 3). The Periodic Noise itself comes on top of the global shift with its known signature: high frequency oscillations with a rapid damp. This effect remains more or less stable with time in terms of amplitude, frequency and decay length, but its phase varies with time, introducing the global offset mentioned above.

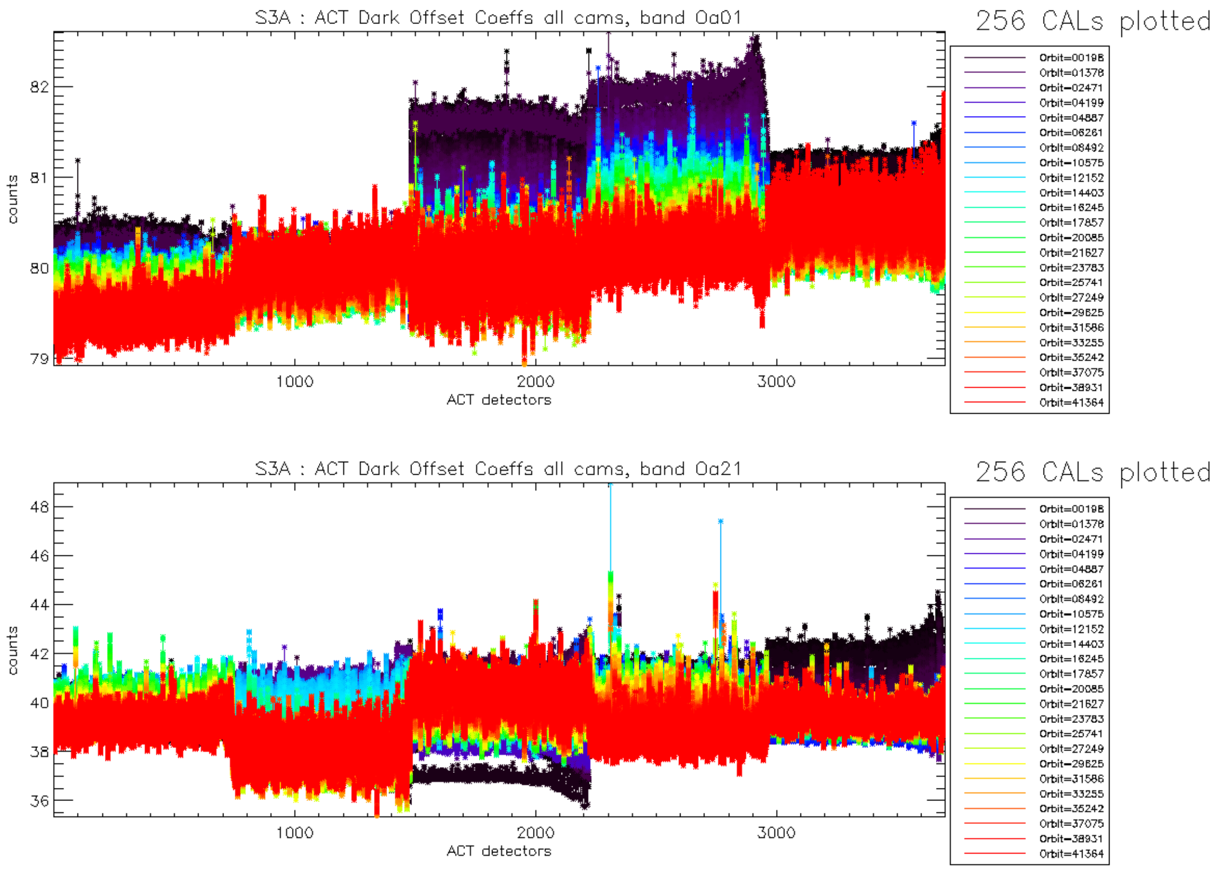

Figure 10: OLCI-A Dark Offset for band Oa1 (top) and Oa21 (bottom), all radiometric calibrations so far except the first one (orbit 183) for which the instrument was not thermally stable yet.

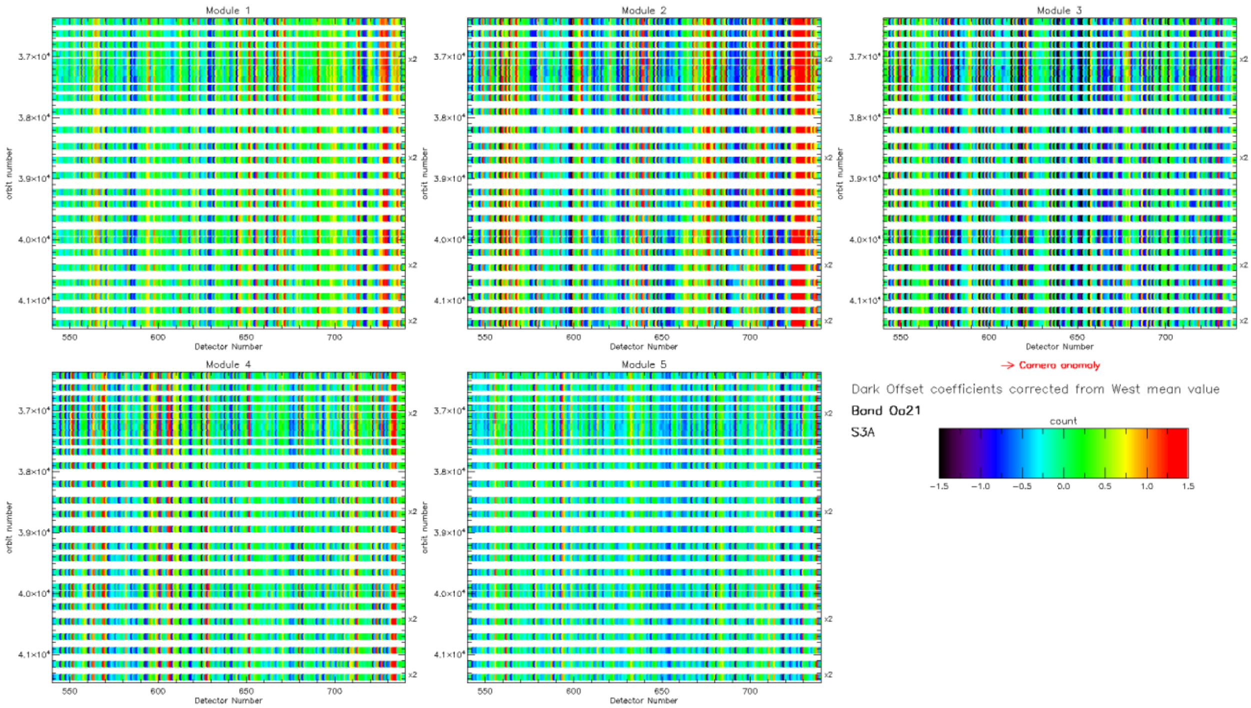

Figure 11: map of OLCI-A periodic noise for the 5 cameras, for band Oa21. X-axis is detector number (East part, from 540 to 740, where the periodic noise occurs), Y-axis is the orbit number. Y-axis range is focused on the most recent 5000 orbits. The counts have been corrected from the West detectors mean value (not affected by periodic noise) in order to remove mean level gaps and consequently to have a better visualisation of the long term evolution of the periodic noise structure. At the beginning of the mission the periodic noise for band Oa21 had strong amplitude in camera 2, 3 and 5 compared to camera 1 and 4. However PN evolved through the mission and these discrepancies between cameras have been reduced. At the time of this Cyclic Report Camera 2 still shows a slightly higher PN than other cameras.

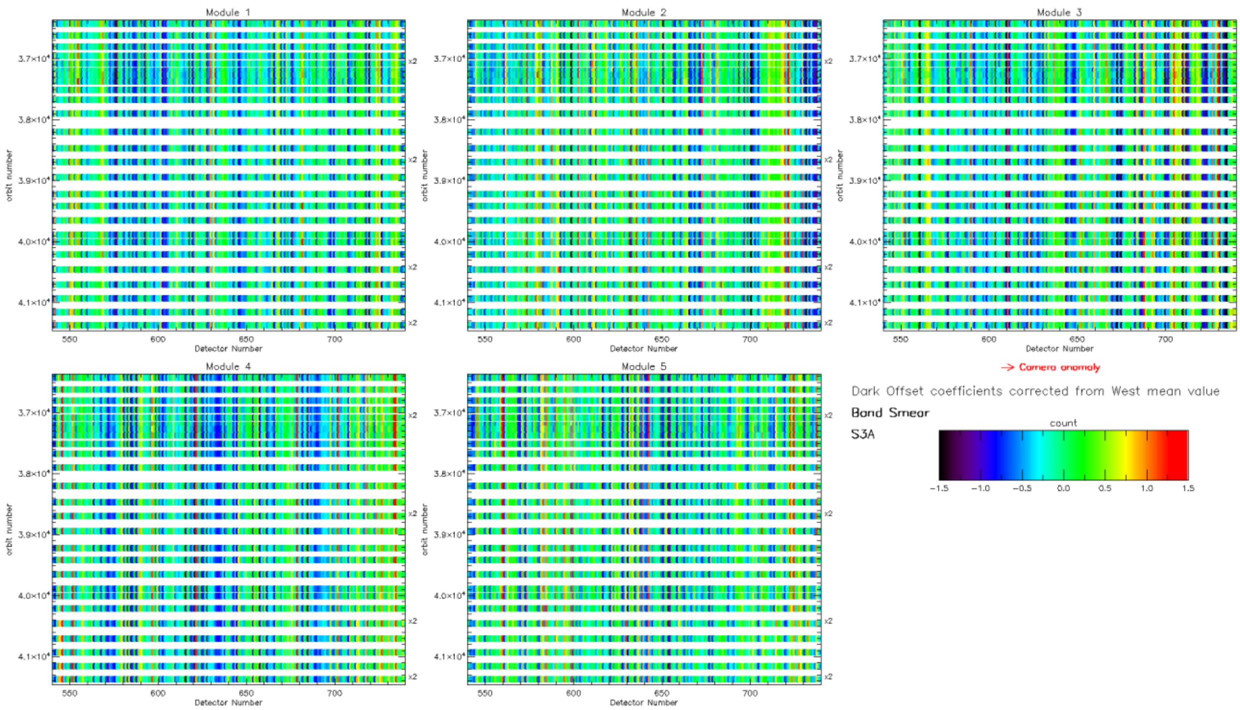

Figure 12: same as Figure 11 for smear band.

Figure 11 and Figure 12 show the so-called 'map of periodic noise' in the 5 cameras, for respectively band 21 and smear band. These maps have been computed from the dark offsets after removal of the mean level of the WEST detectors (not impacted by PN) in order to remove mean level gaps from one CAL to the other and consequently to highlight the shape of the PN. Maps are focused on the last 200 EAST detectors where PN occurs and on a time range covering only the last 5000 orbits in order to better visualize the CALs of the current reporting period.

Figure 11 and Figure 12 show that at this stage of the mission the PN is very stable in all cameras. There is no special behaviour noticed during the reporting period.

Dark Currents

Dark Currents (Figure 13) are not affected by the global offset of the Dark Offsets, thanks to the clamping to the average blind pixels value. However, the oscillations of Periodic Noise remain visible. There is no significant evolution of this parameter during the current reporting period except the small regular increase (almost linear), for all detectors, since the beginning of the mission (see Figure 14).

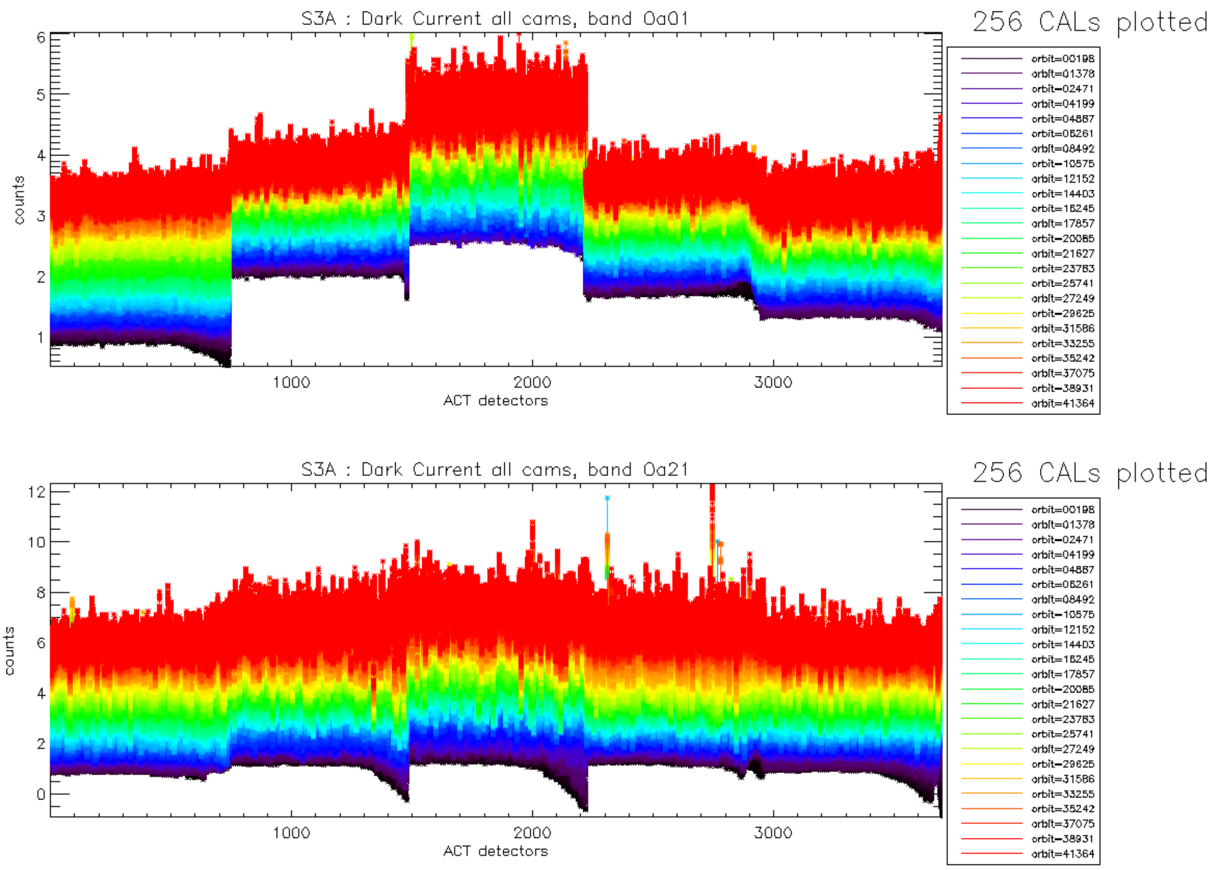

Figure 13: OLCI-A Dark Current for band Oa1 (top) and Oa21 (bottom), all radiometric calibrations so far except the first one (orbit 183) for which the instrument was not thermally stable yet.

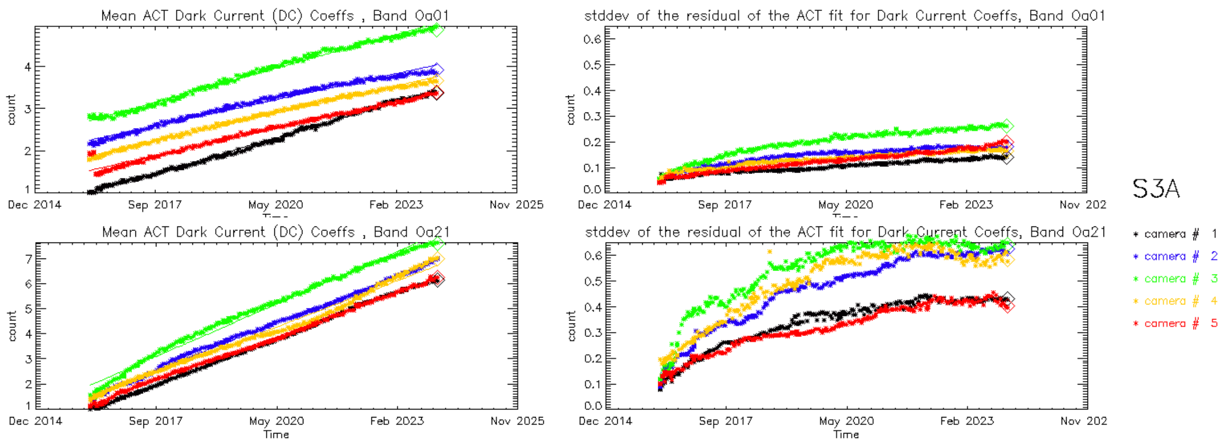

Figure 14: left column: ACT mean on 400 first detectors of OLCI-A Dark Current coefficients for spectral band Oa01 (top) and Oa21 (bottom). Right column: same as left column but for Standard deviation instead of mean. We see an increase of the DC level as a function of time especially for band Oa21.

A possible explanation of the regular increase of DC could be the increase of the number of hot pixels which is more important in Oa21 because this band is made of more CCD lines than band Oa01 and thus receives more cosmic rays impacts. It is known that cosmic rays degrade the structure of the CCD, generating more and more hot pixels at long term scales. Indeed, when computing the time slopes of the spatially averaged Dark Current as a function of band, i.e. the slopes of curves in left plots of Figure 14, one can see that Oa21 is by far the most affected, followed by the smear band (Figure 15, left); when plotting these slopes against total band width (in CCD rows, regardless of the number of micro-bands), the correlation between the slope values and the width becomes clear (Figure 15, right).

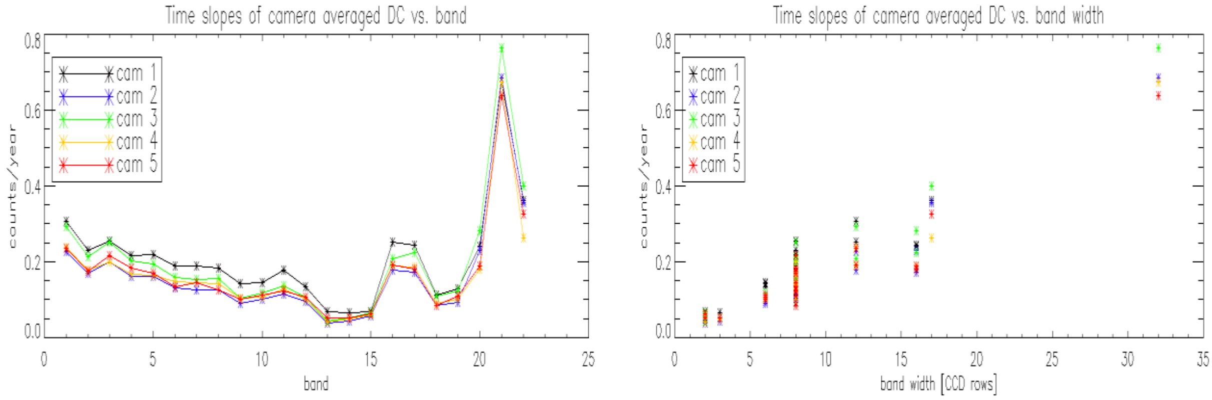

Figure 15: OLCI-A Dark current increase rates with time (in counts per year) vs. band (left) and vs. band width (right)

2.2.1.3 OLCI-B

<u>**Dark Offsets**</u>

Dark offsets for OLCI-B show a similar behaviour than for OLCI-A: mean level gaps between different orbits, induced by the presence of a pseudo periodic noise on the east edge of the cameras with a drifting phase.

Evolution of OLCI-B Dark Offset coefficients for band Oa01 and Oa21 are represented in Figure 16.

The periodic noise maps are shown for band Oa21 and smear band respectively in Figure 17 and Figure 18. As it happened for OLCI-A after a few thousands of orbits, the strong periodic noise phase and amplitude drift, present at the very beginning of the mission is now showing a clear stabilization.

Despite this overall stabilization, small evolutions are still noticeable in some bands/camera, like for example camera 1 in band Oa21 (upper left map in Figure 17) or in camera 1 band smear (upper left map in Figure 18).

Globally, OLCI-B PN is slightly less stabilized than OLCI-A PN.

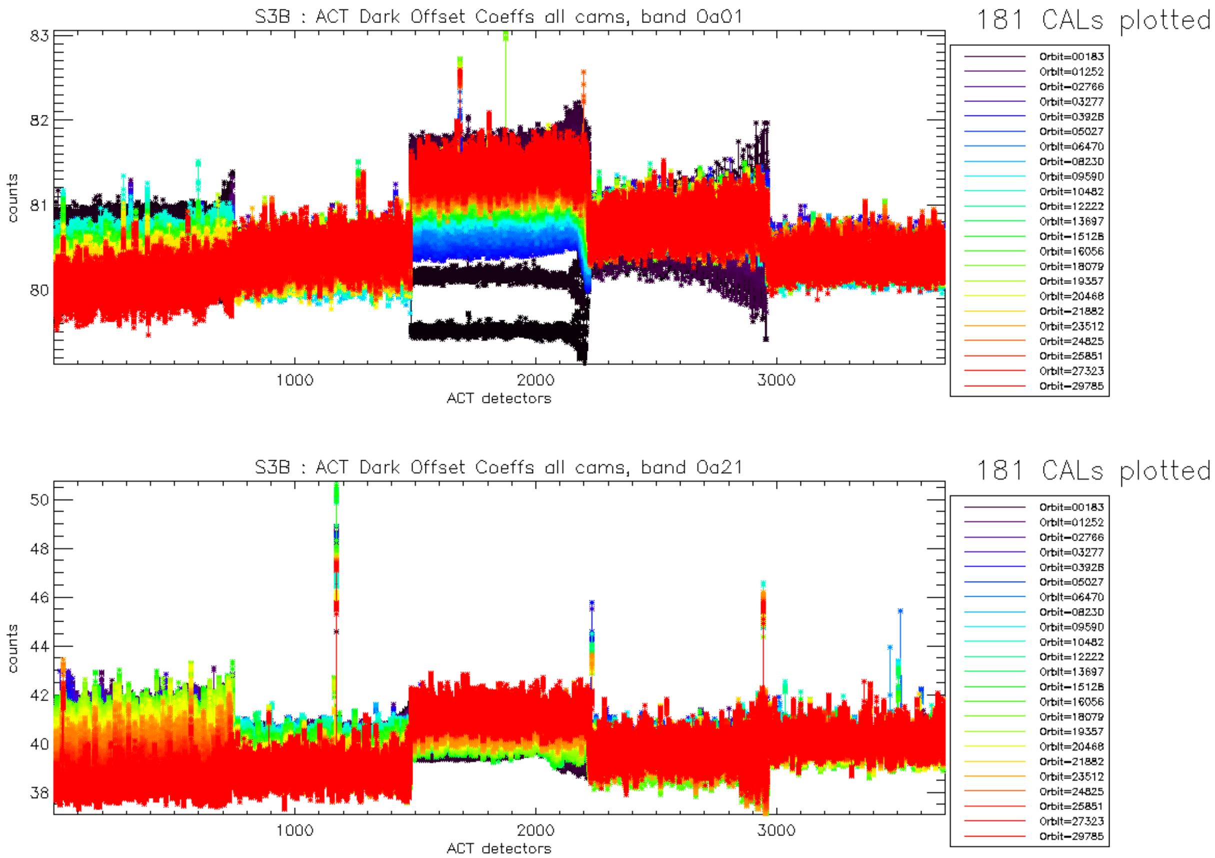

Figure 16: OLCI-B Dark Offset for band Oa1 (top) and Oa21 (bottom), all radiometric calibrations so far except the first one (orbit 167) for which the instrument was not thermally stable yet.

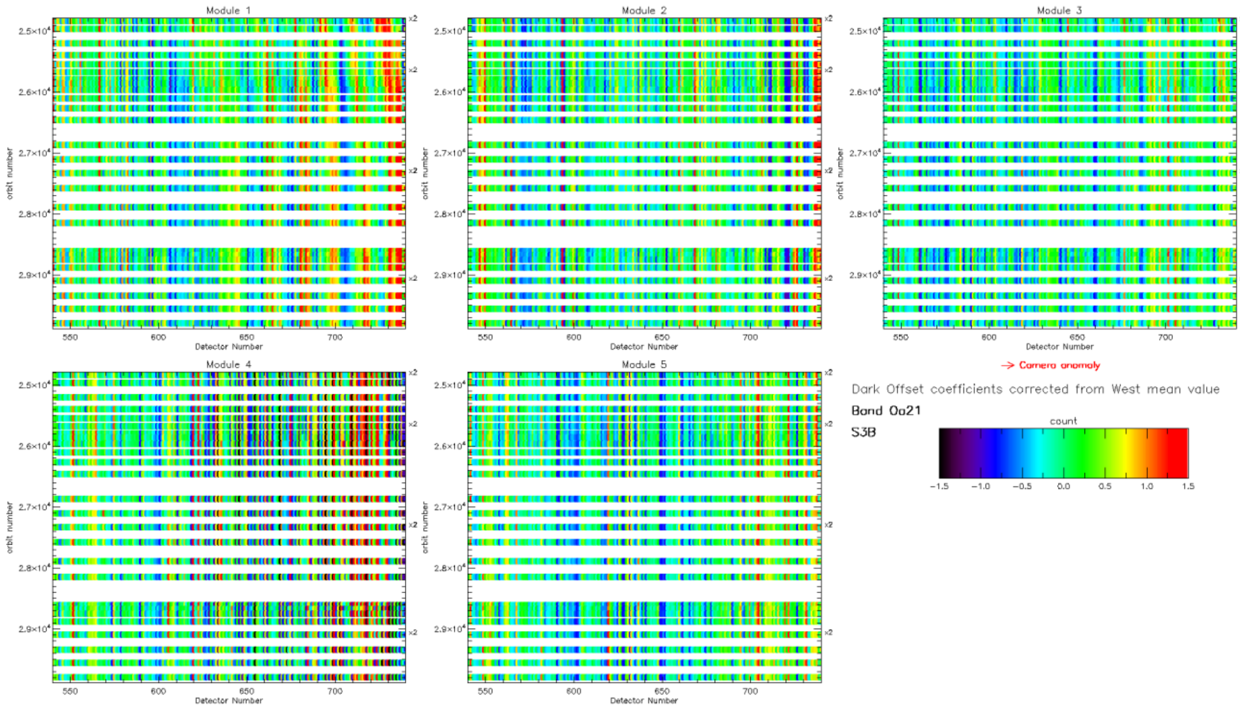

Figure 17: OLCI-B map of periodic noise for the 5 cameras, for band Oa21. X-axis is detector number (East part, from 540 to 740, where the periodic noise occurs), Y-axis is the orbit number. The counts have been corrected from the West detectors mean value (not affected by periodic noise) in order to remove mean level gaps and consequently to have a better visualization of the long term evolution of the periodic noise structure.

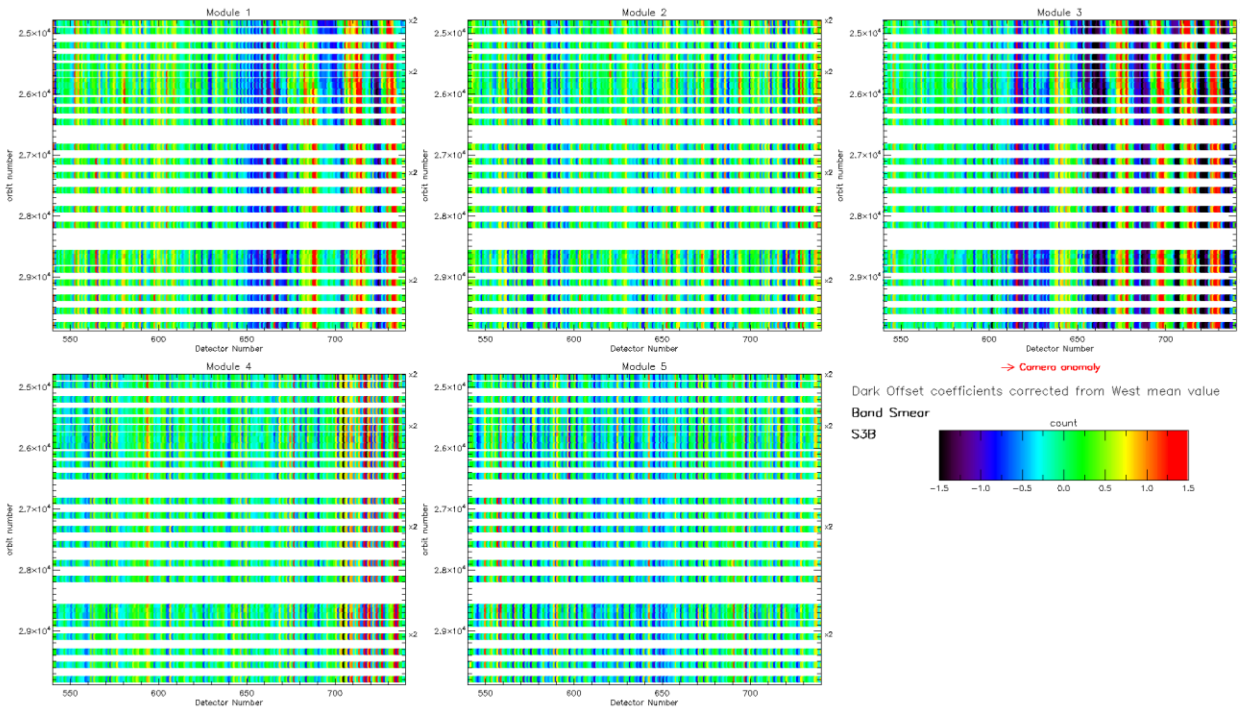

Figure 18: same as Figure 17 for smear band.

Dark Currents

As for OLCI-A there is no significant evolution of the Dark Current coefficients (Figure 19) during the current reporting period except the small regular increase (almost linear), for all detectors, since the beginning of the mission (see Figure 20) probably due to an increase of hot pixels (see Figure 21).

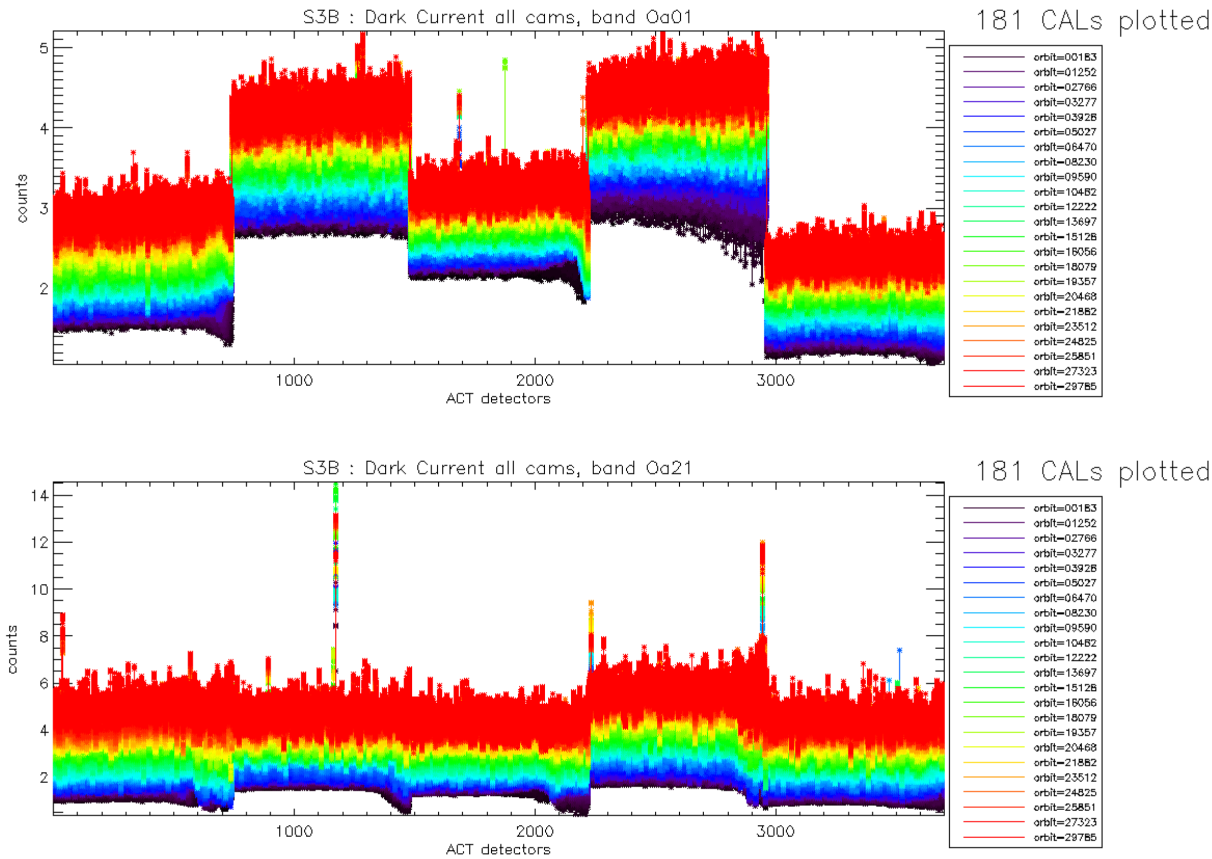

Figure 19: OLCI-B Dark Current for band Oa1 (top) and Oa21 (bottom), all radiometric calibrations so far except the first one (orbit 167) for which the instrument was not thermally stable yet.

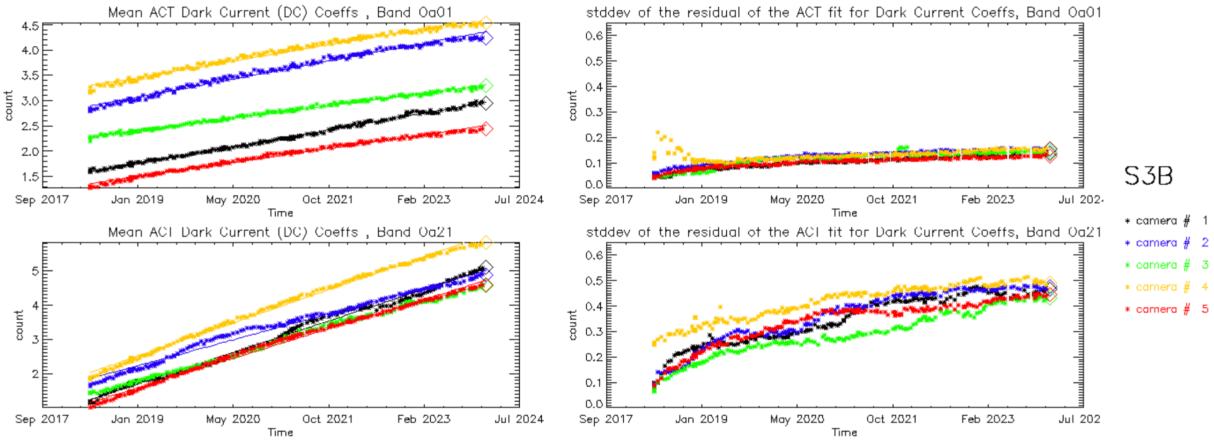

Figure 20: left column: ACT mean on 400 first detectors of OLCI-B Dark Current coefficients for spectral band Oa01 (top) and Oa21 (bottom). Right column: same as left column but for Standard deviation instead of mean. We see an increase of the DC level as a function of time especially for band Oa21.

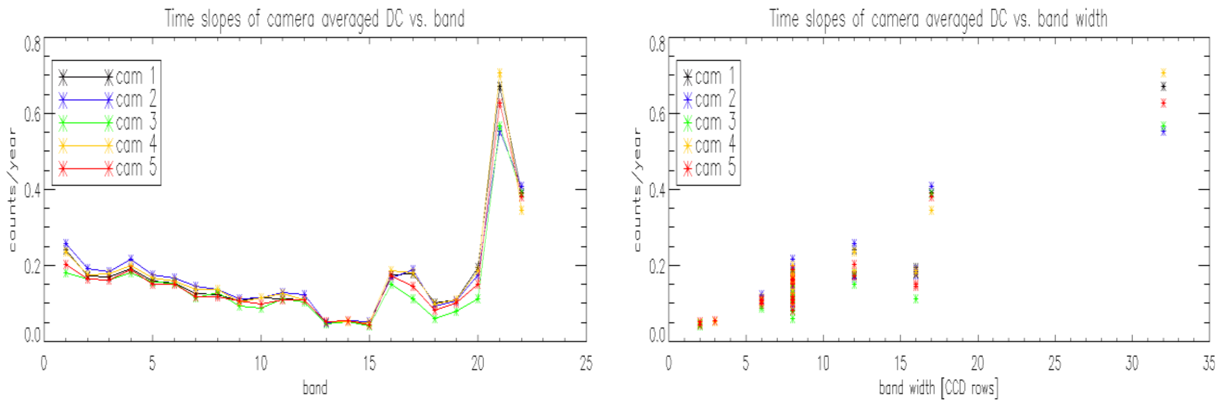

Figure 21: OLCI-B Dark Current increase rates with time (in counts per year) vs. band (left) and vs. band width (right)

2.2.3 Instrument response and degradation modelling [OLCI-L1B-CV-250]

2.2.3.1 Instrument response monitoring

2.2.3.1.1 OLCI-A

Figure 22 shows the gain coefficients of every pixel for two OLCI-A channels, Oa1 (400 nm) and Oa21 (1020 nm), highlighting the significant evolution of the instrument response since early mission.

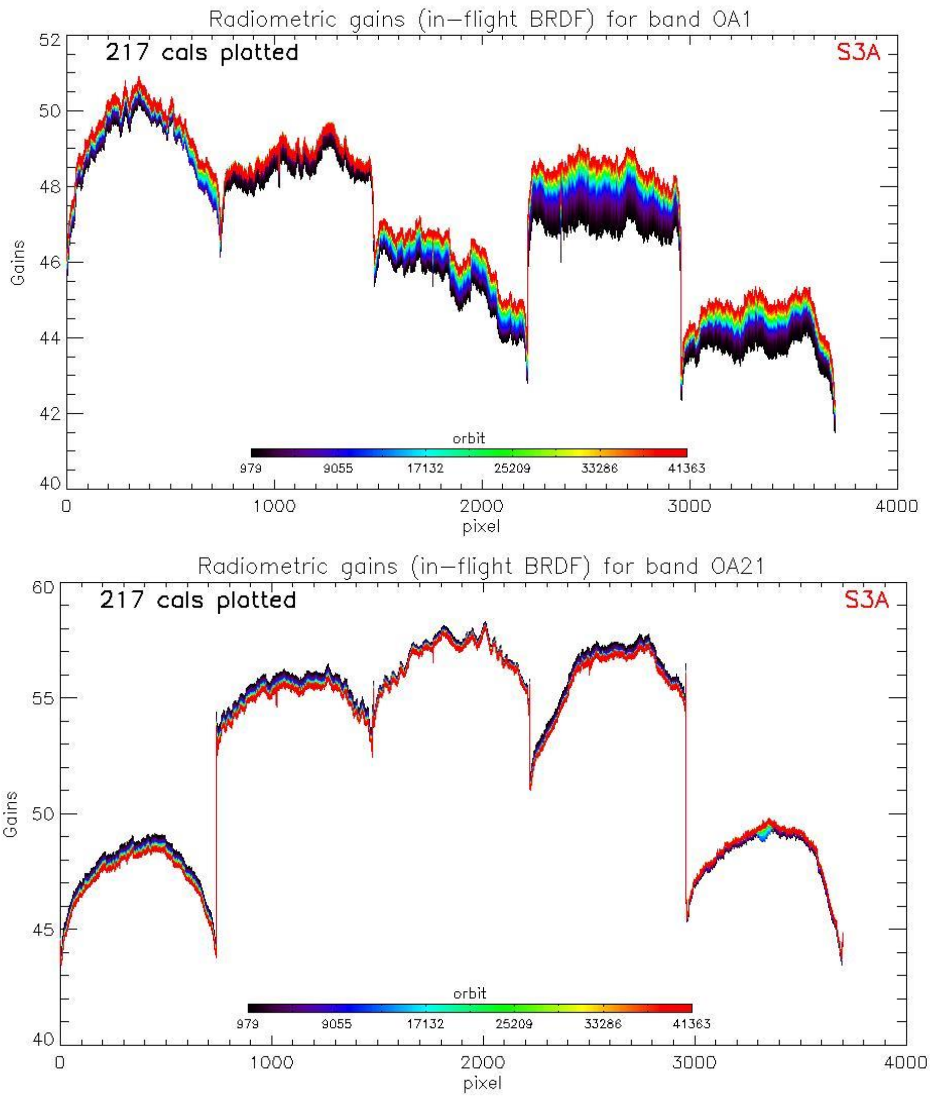

Figure 22: OLCI-A Gain Coefficients for band Oa1 (top) and Oa21 (bottom), derived using the in-flight BRDF model. The dataset is made of all diffuser 1 radiometric calibrations since orbit 979.

Figure 23 displays a summary of the time evolution of the cross-track average of the gains (in-flight BRDF, taking into account the diffuser ageing), for each module, relative to a given reference calibration (the 25/04/2016, change of OLCI channel settings). It shows that, if a significant evolution occurred during the early mission, the trends tend in general to stabilize, with some exceptions (e.g. band 1 of camera 1 and 4, bands 2 & 3 of camera 5).

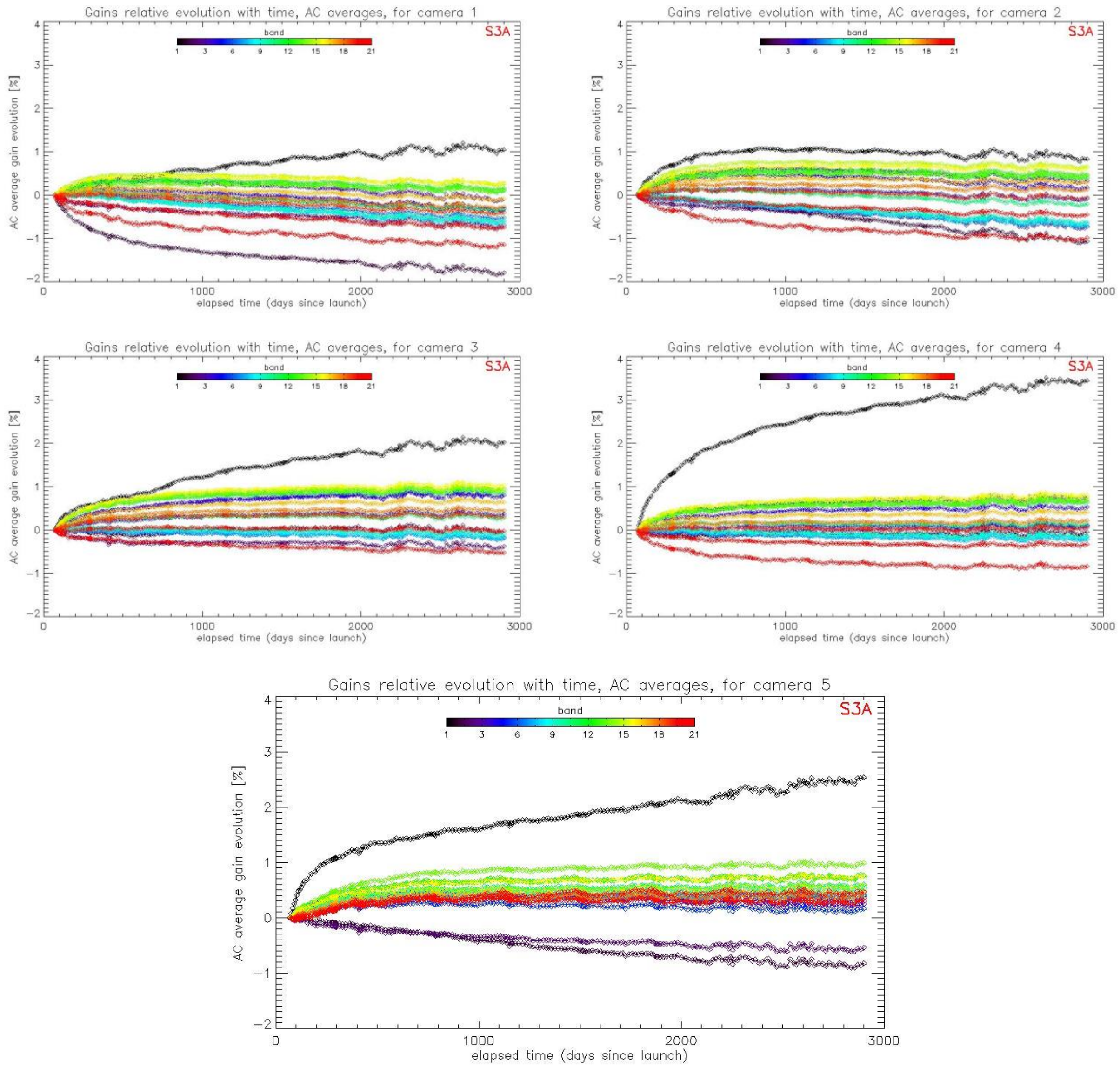

Figure 23: camera averaged gain relative evolution with respect to calibration of 25/04/2016 (change of OLCI channel settings), as a function of elapsed time since the beginning of the mission; one curve for each band (see colour code on plots), one plot for each module. The diffuser ageing is taken into account.

2.2.3.1.2 OLCI-B

Figure 24 shows the gain coefficients of every pixel for two OLCI-B channels, Oa1 (400 nm) and Oa21 (1020 nm), highlighting the significant evolution of the instrument response since early mission.

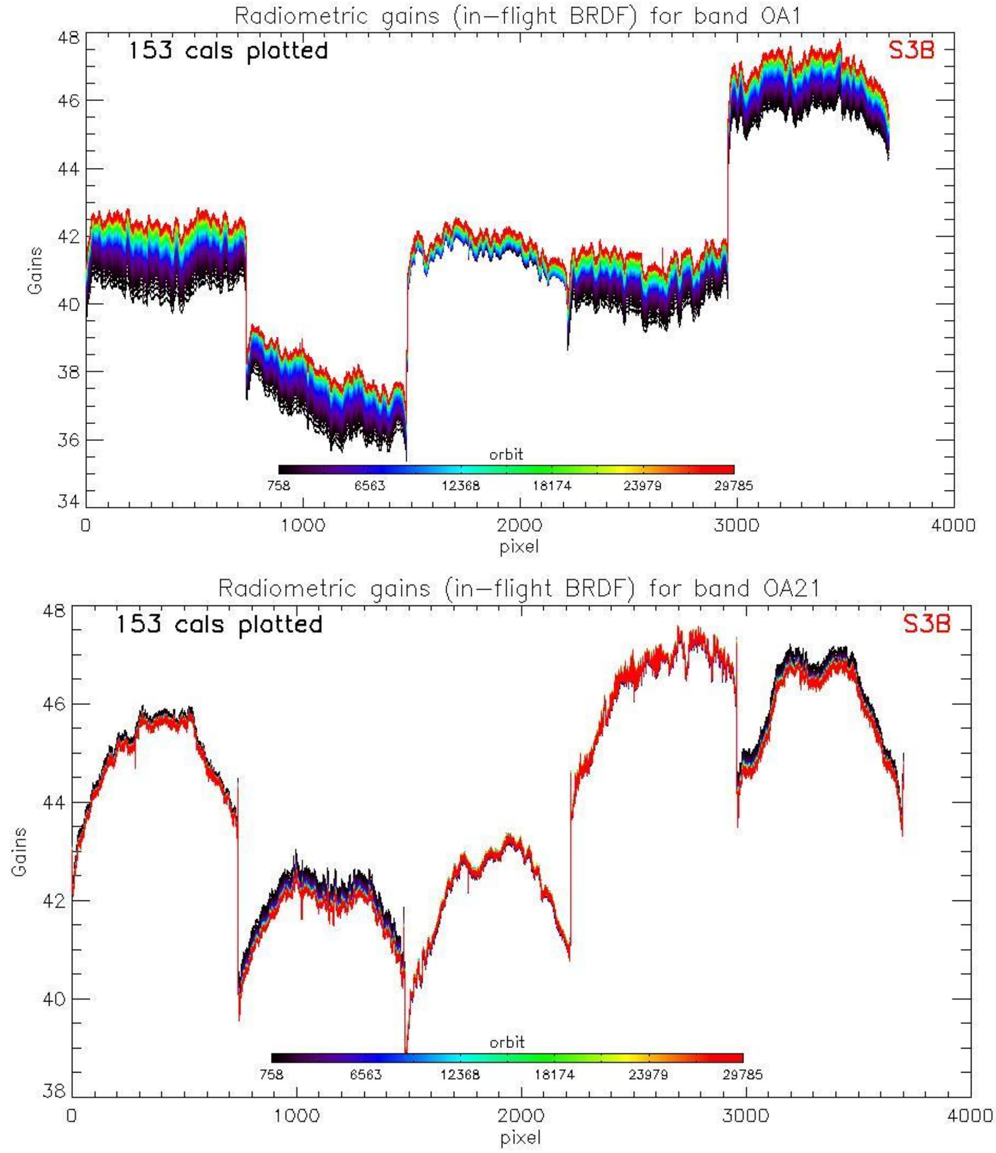

Figure 24: OLCI-B Gain Coefficients for band Oa1 (top) and Oa21 (bottom), derived using the in-flight BRDF model. The dataset is made of all diffuser 1 radiometric calibrations since orbit 758.

Figure 25 displays a summary of the time evolution of the cross-track average of the gains (in-flight BRDF, taking into account diffuser ageing), for each module, relative to a given reference calibration (first calibration after channel programming change: 18/06/2018). It shows that, if a significant evolution occurred during the early mission, the trends tend to stabilize. The large amount of points near elapsed time = 220 days is due to the yaw manoeuvre campaign. The slight discontinuity near "day 920 since launch" is due to the upgrade of the Ageing model.

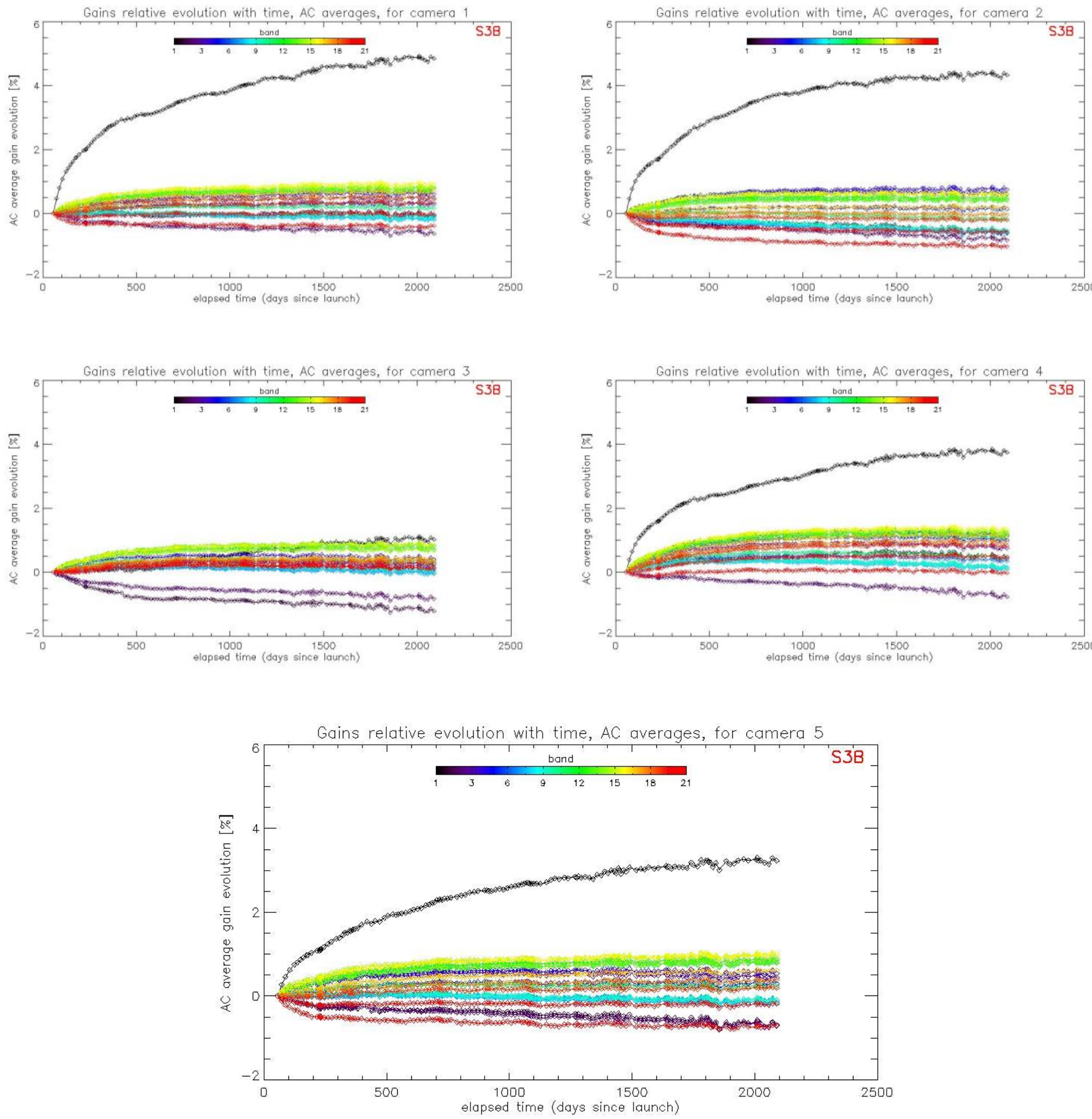

Figure 25: OLCI-B camera averaged gain relative evolution with respect to first calibration after channel programming change (18/06/2018), as a function of elapsed time since the beginning of the mission; one curve for each band (see colour code on plots), one plot for each module. The diffuser ageing is taken into account.

2.2.3.2 Instrument evolution modelling

2.2.3.2.1 OLCI-A

A new OLCI-A Radiometric Gain Model has been put in operations at PDGS the 25/07/2023 (Processing Baseline 3.23). This model has been derived on the basis of an extended (compared to the previous model) Radiometric Calibration dataset, going from 11/04/2016 to 28/05/2023. It includes the correction of the diffuser ageing for the six bluest bands (Oa1 to Oa6) for which it is clearly measurable. The model performance over the complete dataset (including the 14 calibrations in extrapolation over about 8 months) remains better than about 0.13% for all bands. The previous model, trained on a Radiometric Dataset limited to 30/04/2022, shows a clear drift of the model with respect to most recent data (Figure 27), that motivated the change. Comparison of the two figures shows the improvement brought by the updated model over almost all the mission. Performance shown on Figure 26 adopts, as for OLCI-B, the multiple model approach, i.e. different models (two for OLCI-A since this new PB, three for OLCI-B since PB 1.57) are used to cover the whole mission (red dashed line on Figure 26), each model being fitted on a partial dataset (green dashed line on Figure 26) whose coverage is optimized to provide best performance.

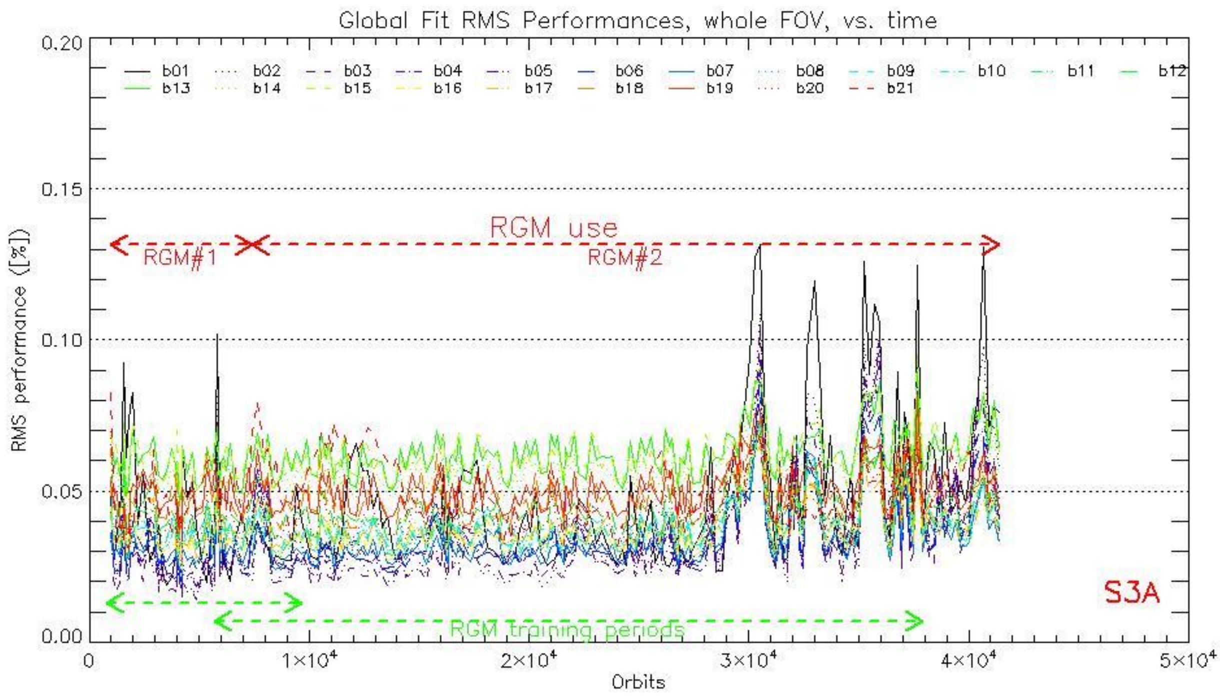

Figure 26: RMS performance of the OLCI-A Gain Model of the current processing baseline as a function of orbit.

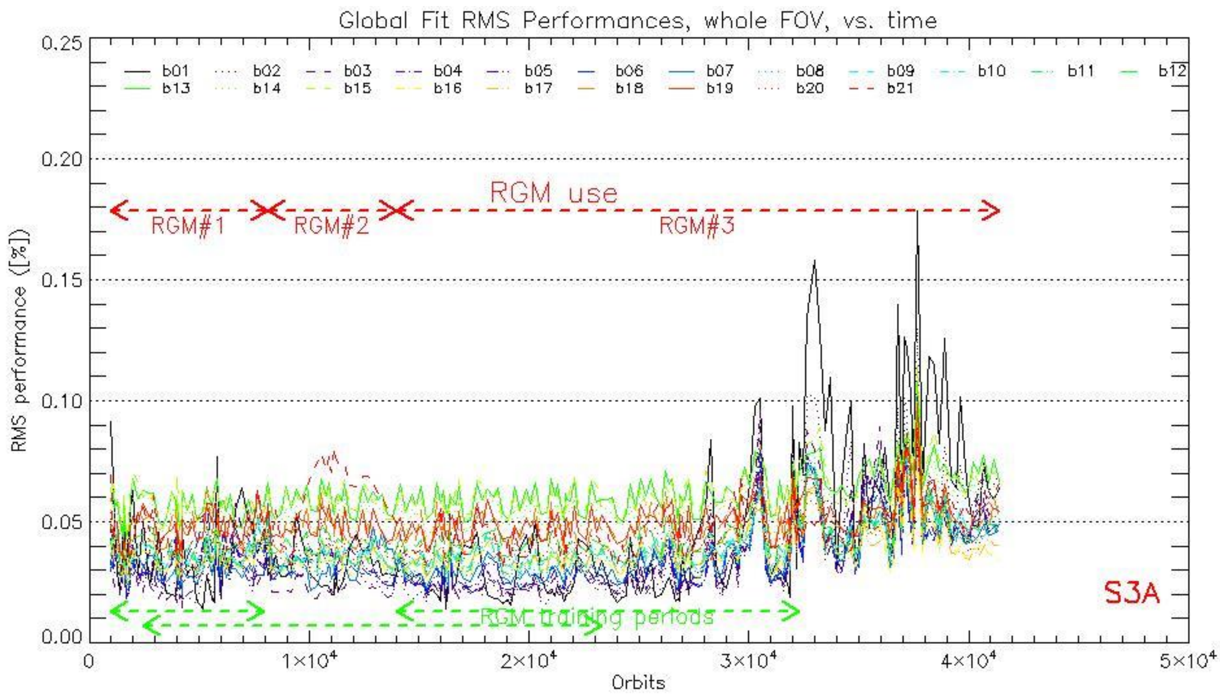

Figure 27: RMS performance of the OLCI-A Gain Model of the previous Processing Baseline as a function of orbit.

The overall instrument evolution since channel programming change (25/04/2016) is shown on Figure 28.

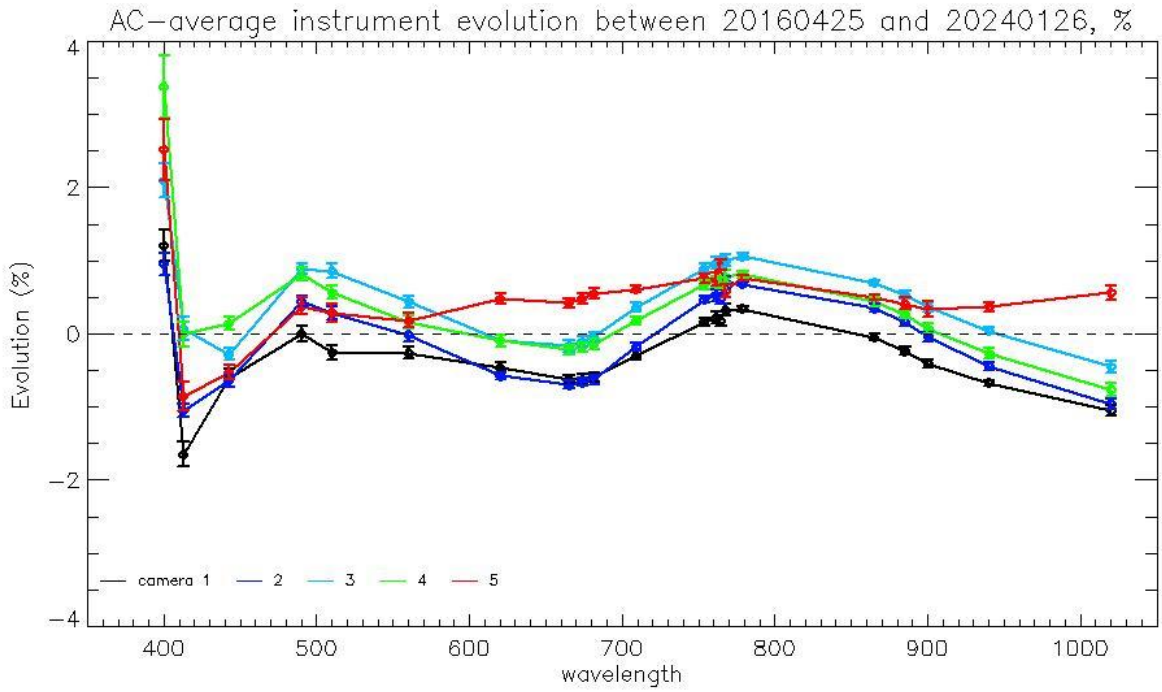

Figure 28: OLCI-A Camera-averaged instrument evolution since channel programming change (25/04/2016) and up to the most recent calibration (26/01/2024) versus wavelength.

The overall per camera performance, as a function of wavelength, and at each orbit is shown on Figure 29 as the average and standard deviation of the model over data ratio.

Finally, Figure 30 to Figure 32 show the detail of the model performance, with across-track plots of the model over data ratios at each orbit, one plot for each channel.

Comparisons of Figure 30 to Figure 32 with their counterparts in DQR of July 2023 clearly demonstrate the improvement brought by the new model whatever the level of detail.

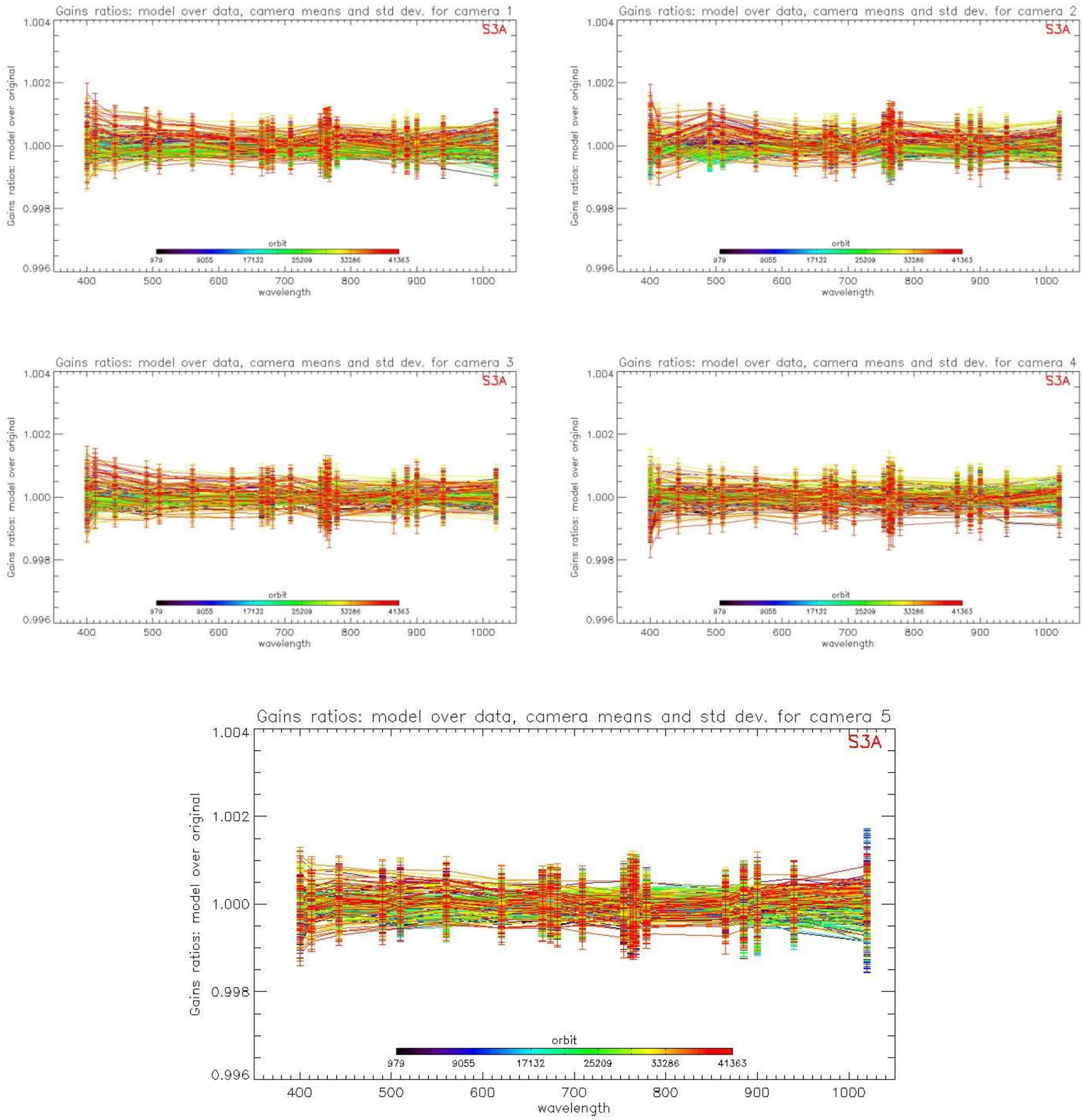

Figure 29: For the 5 cameras: OLCI-A Evolution model performance, as camera-average and standard deviation of ratio of Model over Data vs. wavelength, for each orbit of the test dataset, including 14 calibrations in extrapolation, with a colour code for each calibration from blue (oldest) to red (most recent).

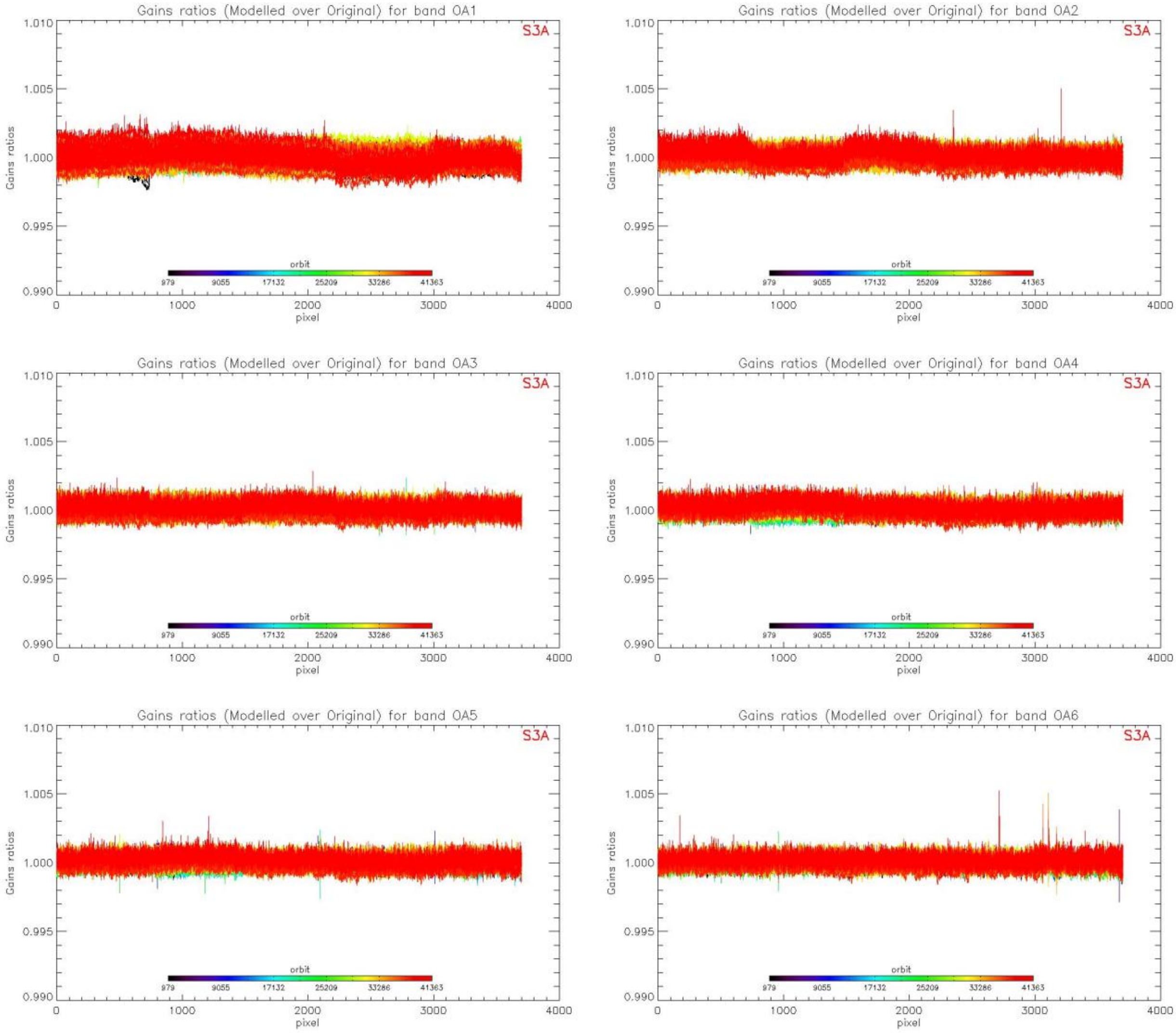

Figure 30: OLCI-A evolution model performance, as ratio of Model over Data vs. pixels, all cameras side by side, over the whole current calibration dataset (since instrument programming update), including 14 calibrations in extrapolation, channels Oa1 to Oa6.

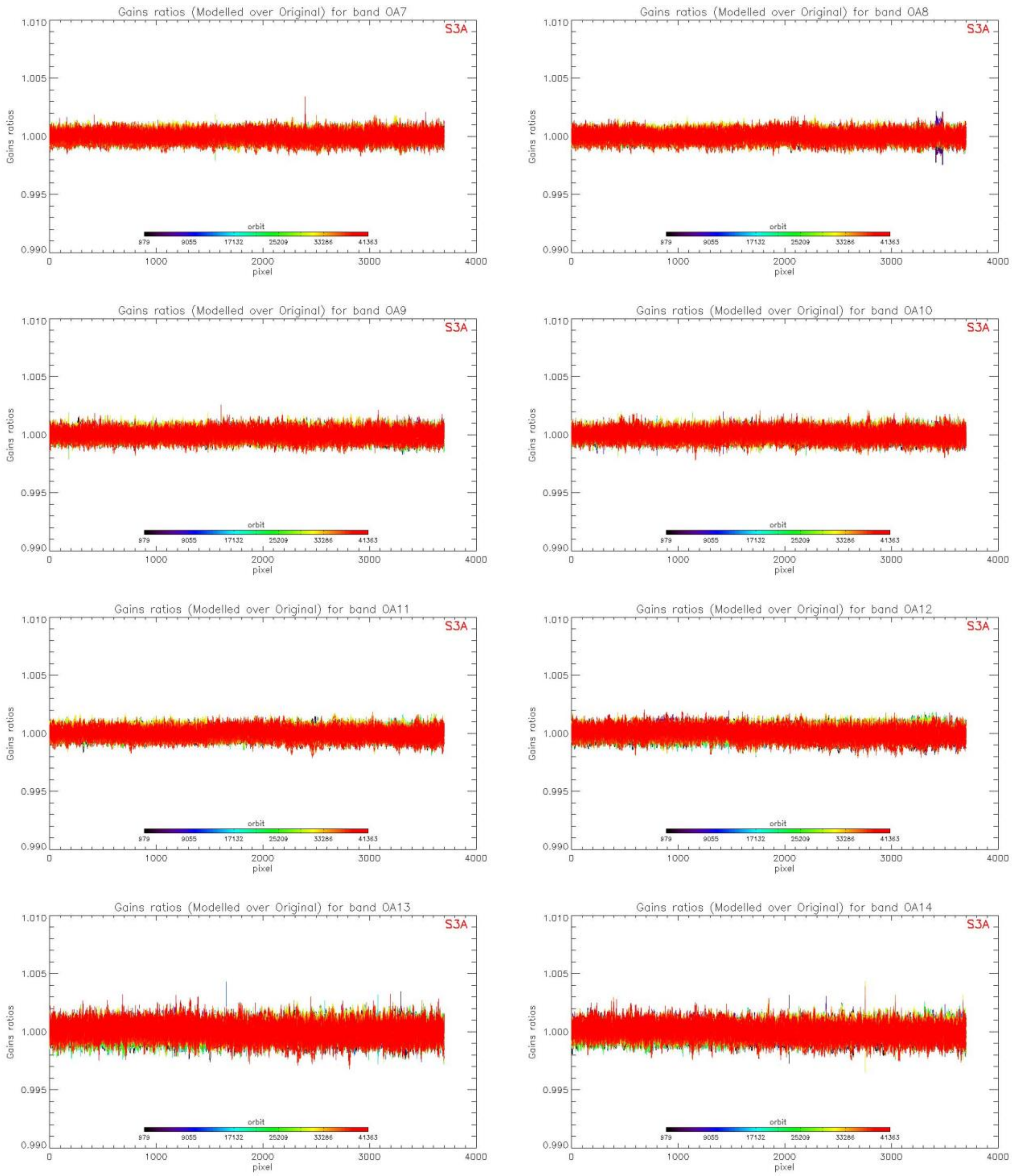

Figure 31: same as Figure 30 for channels Oa7 to Oa14.

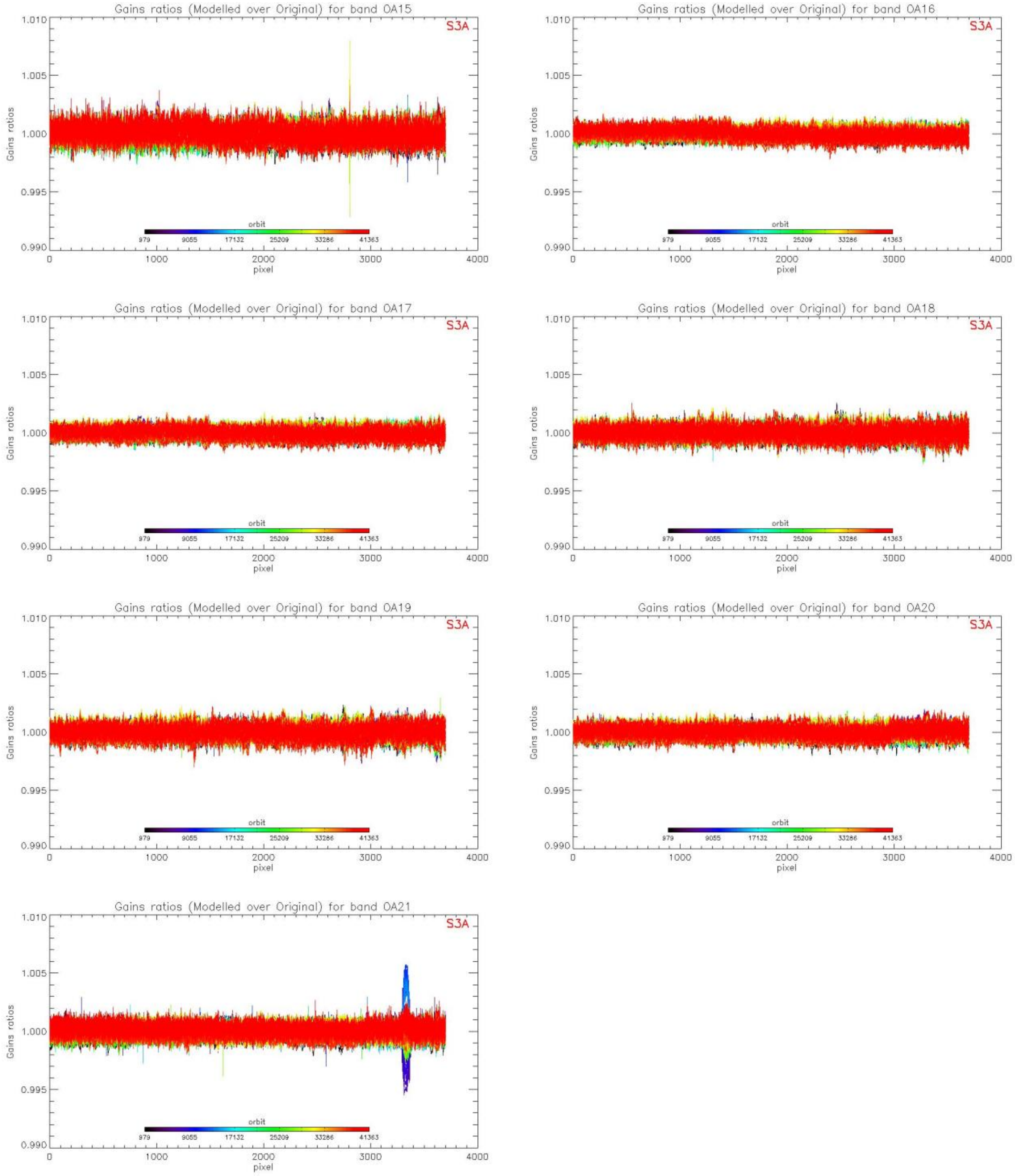

Figure 32: same as Figure 30 for channels Oa15 to Oa21.

2.2.3.2.2 OLCI-B

A new OLCI-B Radiometric Gain Model has been put in operations at PDGS on 18/07/2023 (Processing Baseline 3.23). This model has been derived on the basis of an extended Radiometric Calibration dataset (from 08/05/2018 to 24/05/2023). It includes the correction of the diffuser ageing for the five bluest bands (Oa1 to Oa5) for which it is clearly measurable. The model performance over the complete dataset (including 13 calibrations in extrapolation over about 8 months) is illustrated in Figure 33. It remains better than about 0.14% when averaged over the whole field of view for all bands at the exception of a spike near orbit 26500 reaching about up to 0.20 % for Oa02 and another spike near orbit 29000 reaching about up to 0.17 % for Oa01. The previous model, trained on a Radiometric Dataset limited to 29/04/2022, shows a significant drift of the model with respect to most recent data (Figure 34). Comparison of the two figures shows the improvement brought by the updated Model over all the mission.

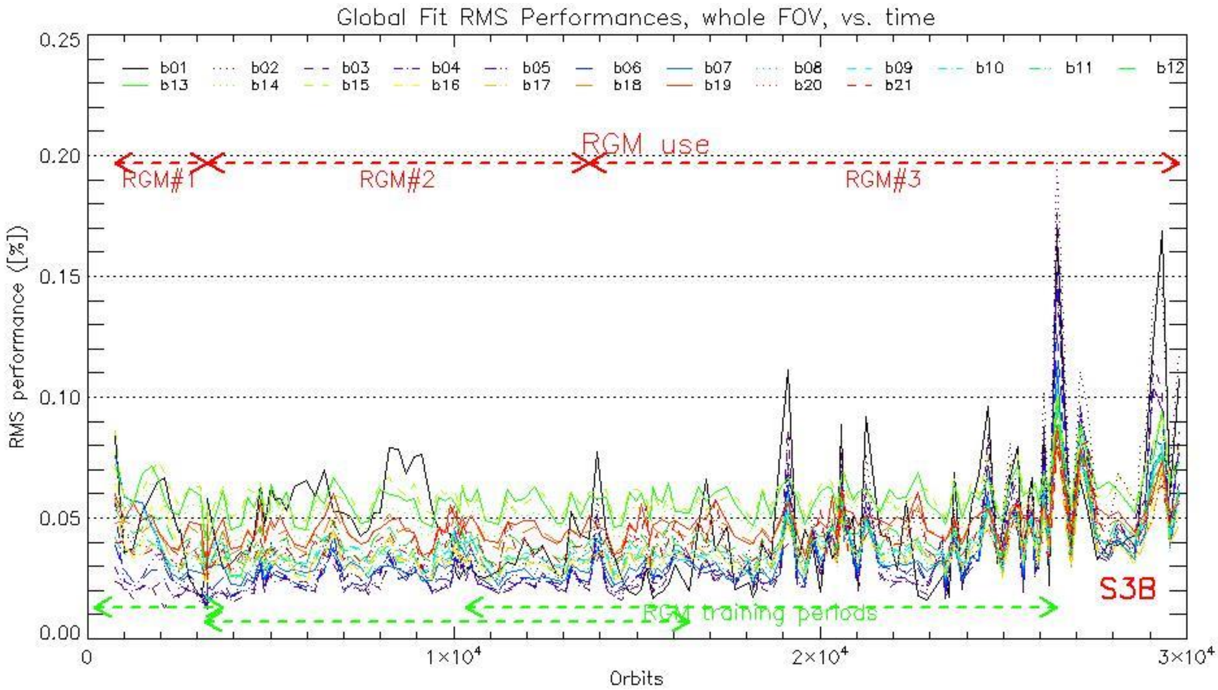

Figure 33: RMS performance of the OLCI-B Gain Model of the current processing baseline as a function of orbit.

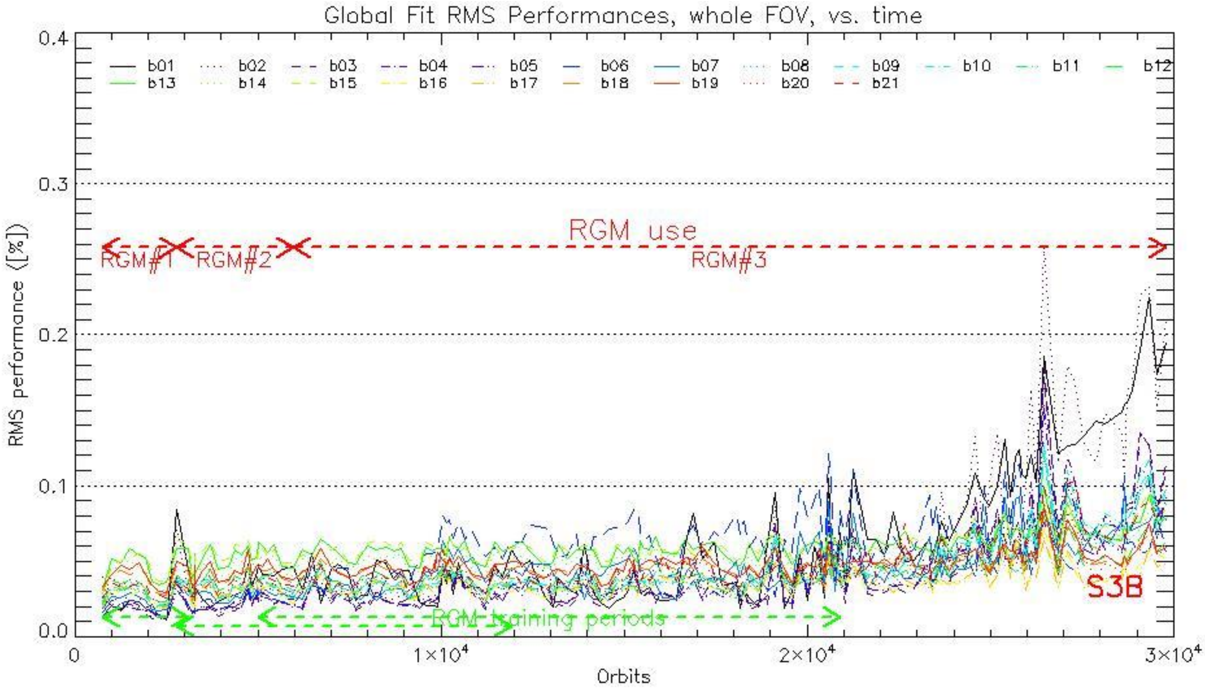

Figure 34: RMS performance of the OLCI-B Gain Model of the previous processing baseline as a function of orbit (please note the different vertical scale with respect to Figure 33).

The overall instrument evolution since channel programming change (18/06/2018) is shown on Figure 35.

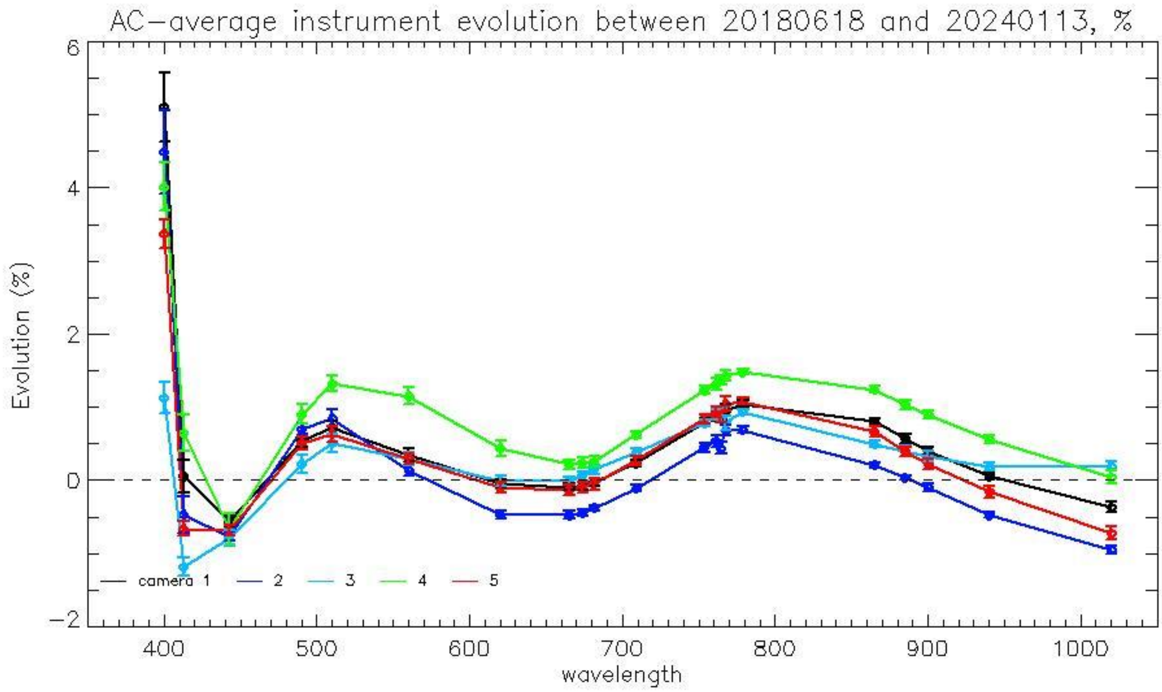

Figure 35: OLCI-B Camera-averaged instrument evolution since channel programming change (18/06/2018) and up to most recent calibration (13/01/2024) versus wavelength.

The overall per camera performance, as a function of wavelength, and at each orbit is shown on Figure 36 as the average and standard deviation of the model over data ratio.

Finally, Figure 37 to Figure 39 show the detail of the model performance, with across-track plots of the model over data ratios at each orbit, one plot for each channel.

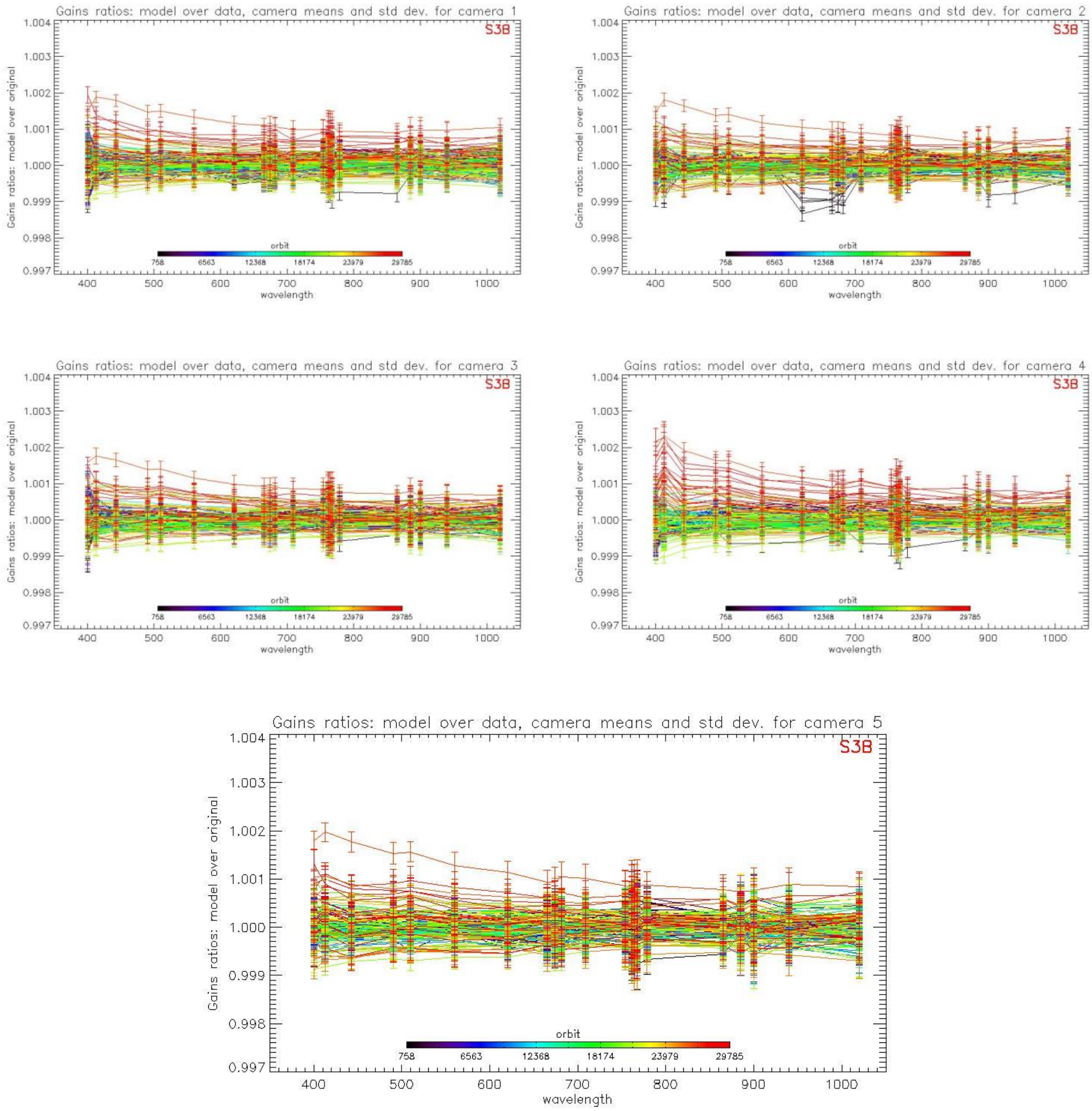

Figure 36: For the 5 cameras: OLCI-B Evolution model performance, as camera-average and standard deviation of ratio of Model over Data vs. wavelength, for each orbit of the test dataset, including 13 calibrations in extrapolation, with a colour code for each calibration from blue (oldest) to red (most recent).

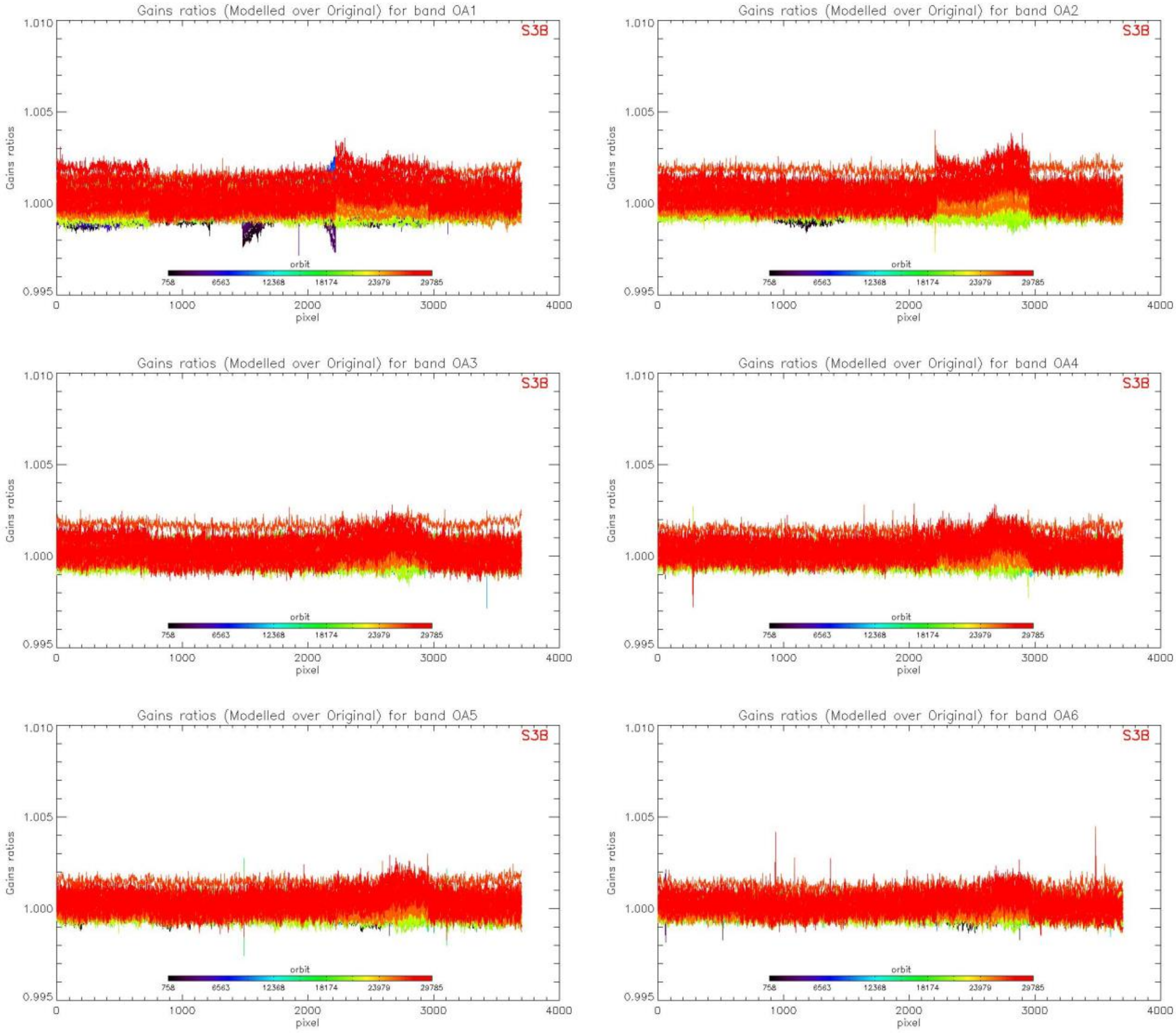

Figure 37: OLCI-B evolution model performance, as ratio of Model over Data vs. pixels, all cameras side by side, over the whole current calibration dataset (since instrument programming update), including 13 calibrations in extrapolation, channels Oa1 to Oa6.

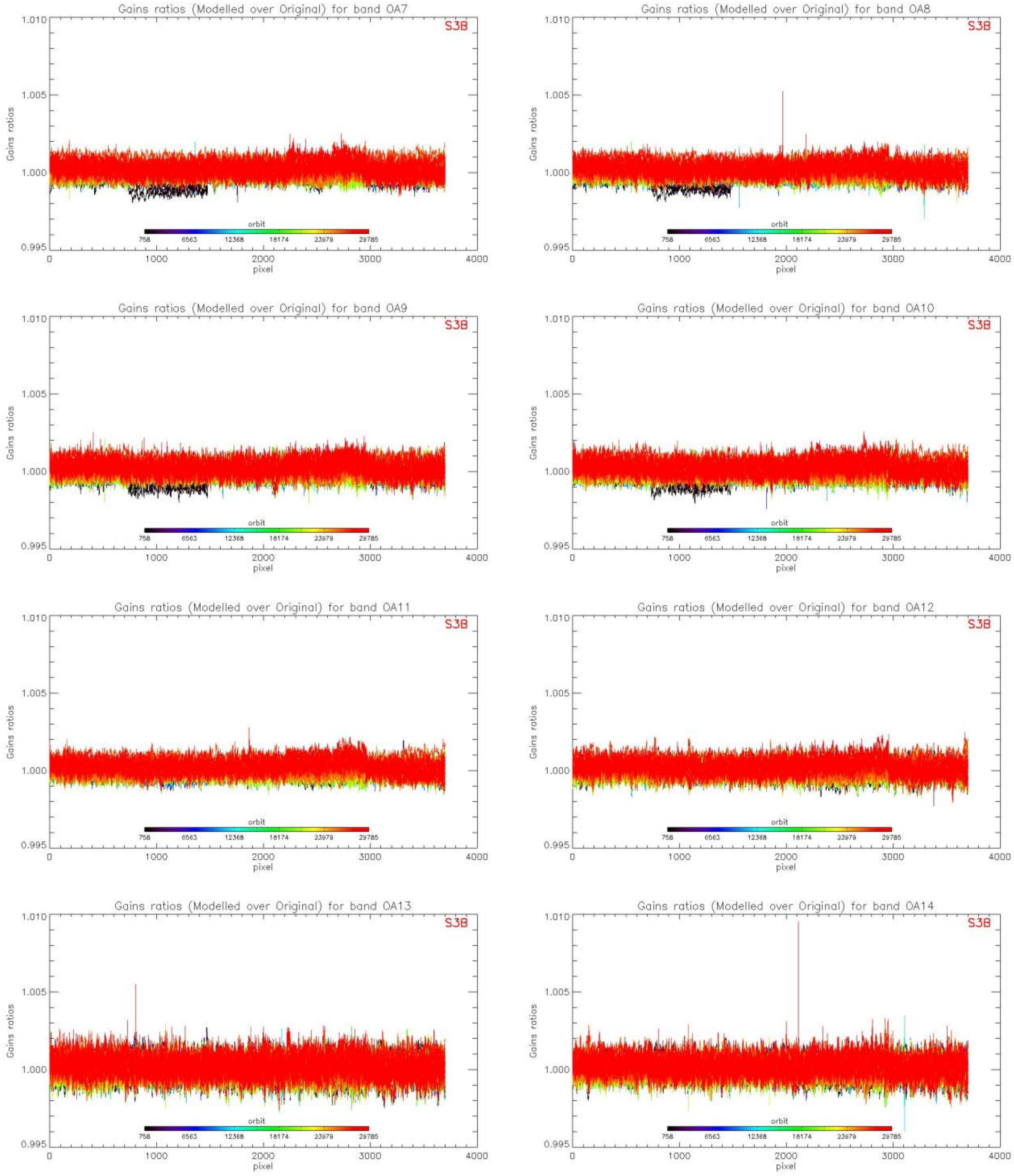

Figure 38: same as Figure 37 for channels Oa7 to Oa14.

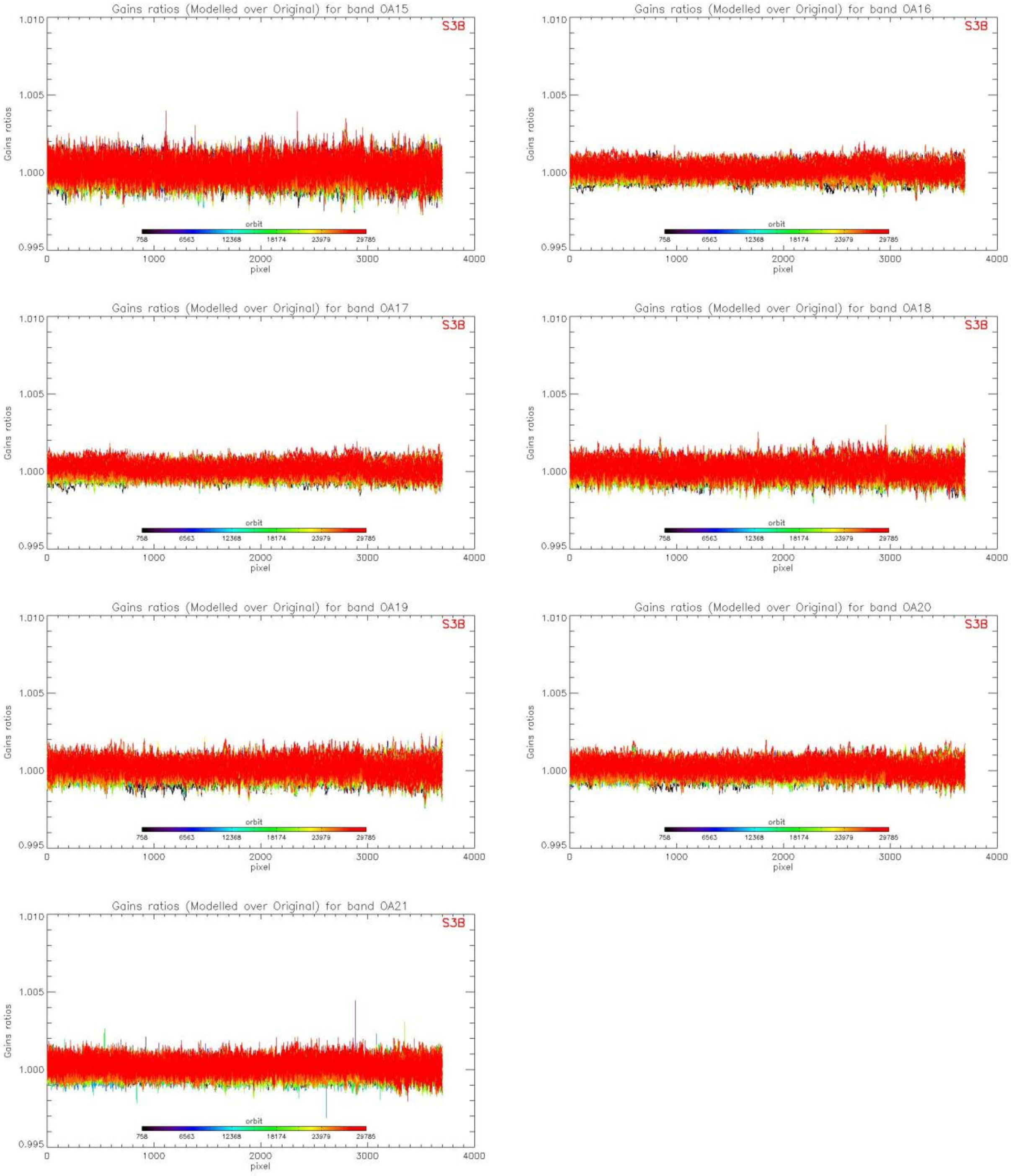

Figure 39: same as for channels Oa15 to Oa21.

2.2.4 Ageing of nominal diffuser [OLCI-L1B-CV-240]

2.2.4.1 OLCI-A

There has been one calibration sequence S05 (reference diffuser) for OLCI-A during the current reported period:

- S05 sequence (diffuser 5) on 26/01/2024 15:28 to 15:30 (absolute orbit 41364)

With the associated S01 sequence (nominal diffuser) in order to compute ageing:

- S01 sequence (diffuser 1) on 26/01/2024 13:47 to 13:49 (absolute orbit 41363)

The ageing results derived from these measurements will be presented in the February DQR at the same time as the OLCI-B ageing results derived from the planned OLCI-B S01/S05 February 2024 acquisitions.

2.2.4.2 OLCI-B

There has been no calibration sequence S05 (reference diffuser) for OLCI-B during the current reporting period.

Consequently, the last ageing results, presented in November 2023 DQR, remain valid.

2.2.5 Updating of calibration ADF [OLCI-L1B-CV-260]

2.2.5.1 OLCI-A

No CAL_AX ADF has been delivered to PDGS during the report period for OLCI-A.

2.2.5.2 OLCI-B

No CAL_AX ADF has been delivered to PDGS during the report period for OLCI-B.

2.3 Spectral Calibration [OLCI-L1B-CV-400]

2.3.1 OLCI-A

There has been no S02+S03 nor S09 Spectral Calibration for OLCI-A in the reporting period.

Consequently, the last spectral calibration results, presented in January 2024 DQR, remains valid.

2.3.2 OLCI-B

There has been no S02+S03 nor S09 Spectral Calibration for OLCI-B in the reporting period.

Consequently, the last spectral calibration results, presented in January 2024 DQR, remains valid.

2.4 Signal to Noise assessment [OLCI-L1B-CV-620]

2.4.1 SNR from Radiometric calibration data

2.4.1.1 OLCI-A

SNR computed for all calibration data (S01, S04 and S05 sequences) as a function of band number is presented in Figure 40.

SNR computed for all calibration data as a function of orbit number for band Oa01 (the less stable band) is presented in Figure 41.

There is no significant evolution of this parameter during the current reporting period and the ESA requirement is fulfilled for all bands.

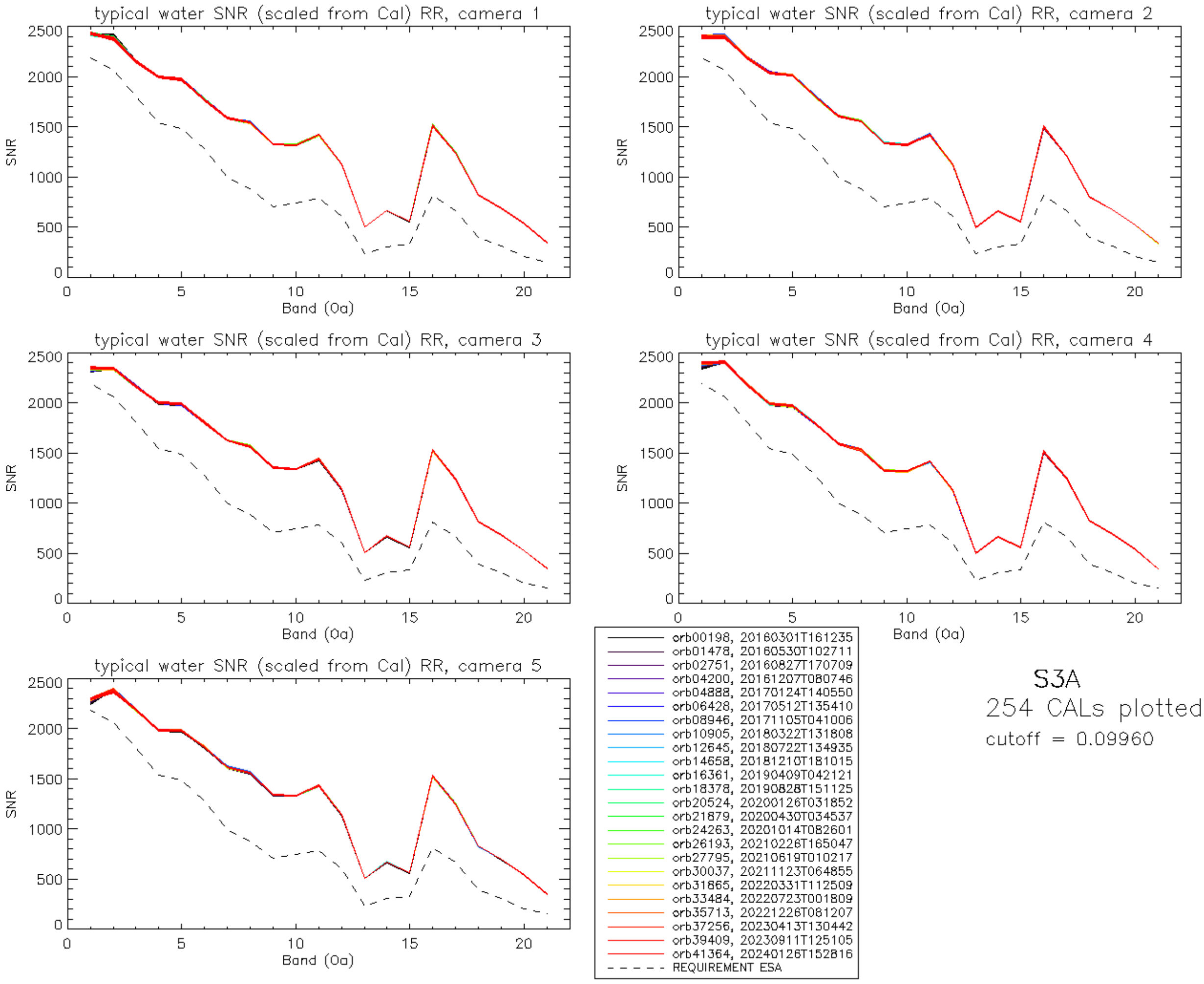

Figure 40: OLCI-A Signal to Noise ratio as a function of the spectral band for the 5 cameras. These results have been computed from radiometric calibration data. All calibrations except first one (orbit 183) are presents with the colours corresponding to the orbit number (see legend). The SNR is very stable with time: the curves for all orbits are almost superimposed. The dashed curve is the ESA requirement.

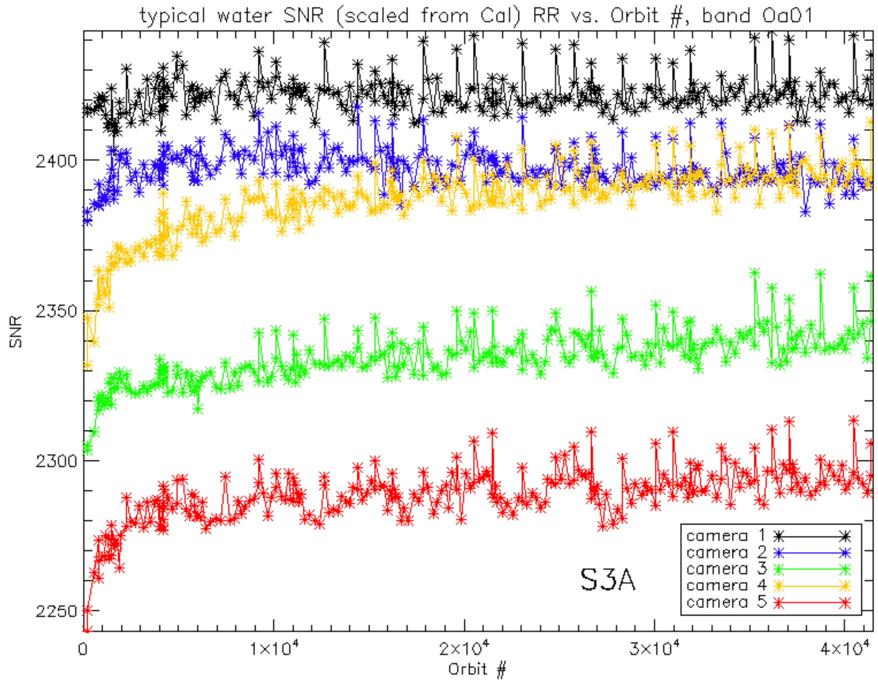

Figure 41: long-term stability of the SNR estimates from Calibration data, example of channel Oa1.

The mission averaged SNR figures are provided in Table 1 below, together with their radiance reference level. According to the OLCI SNR requirements, these figures are valid at these radiance levels and at Reduced Resolution (RR, 1.2 km). They can be scaled to other radiance levels assuming shot noise (CCD sensor noise) is the dominating term, i.e. radiometric noise can be considered Gaussian with its standard deviation varying as the square root of the signal; in other words: $SNR(L) = SNR(L_{ref}) \cdot \sqrt{\frac{L}{L_{ref}}}$. Following the same assumption, values at Full Resolution (300m) can be derived from RR ones as 4 times smaller.

Table 1: OLCI-A SNR figures as derived from Radiometric Calibration data. Figures are given for each camera (time average and standard deviation), and for the whole instrument. The requirement and its reference radiance level are recalled (in mW.sr^{-1}.m^{-2}.nm^{-1}).

	L_{ref}	SNR	C1		C2		C3		C4		C5		All	
nm	LU	RQT	avg	*std*	avg	*std*	avg	*std*	avg	*std*	avg	*std*	avg	*std*
400.000	63.0	2188	2422	6.3	2397	6.3	2334	8.7	2386	12.1	2288	9.3	2365	7.1
412.000	74.1	2061	2385	9.7	2402	7.9	2339	5.0	2401	5.2	2378	9.5	2381	6.0
442.000	65.6	1811	2157	6.2	2195	6.2	2163	5.0	2185	4.3	2193	5.9	2178	4.3
490.000	51.2	1541	1999	4.8	2036	4.8	1998	4.3	1984	4.4	1988	4.3	2001	3.1
510.000	44.4	1488	1978	5.3	2014	4.8	1986	4.5	1967	4.3	1985	4.1	1986	3.3
560.000	31.5	1280	1774	4.7	1802	4.1	1803	4.8	1794	3.8	1819	3.3	1799	2.9
620.000	21.1	997	1590	4.1	1608	4.3	1624	3.2	1593	3.3	1615	3.4	1606	2.5
665.000	16.4	883	1545	4.2	1556	4.5	1566	3.9	1533	3.6	1561	3.6	1552	3.0
674.000	15.7	707	1328	3.4	1336	3.7	1350	2.8	1323	3.2	1343	3.3	1336	2.4
681.000	15.1	745	1319	3.6	1325	3.4	1338	2.7	1314	2.5	1334	3.3	1326	2.1
709.000	12.7	785	1420	4.1	1420	4.0	1435	3.4	1414	3.5	1431	3.0	1424	2.6
754.000	10.3	605	1127	3.0	1121	2.8	1136	3.1	1125	2.5	1140	2.6	1130	2.1
761.000	6.1	232	502	1.1	499	1.1	505	1.1	501	1.1	508	1.3	503	0.8
764.000	7.1	305	662	1.5	658	1.5	668	2.0	662	1.5	670	1.9	664	1.2
768.000	7.6	330	558	1.4	555	1.2	563	1.3	557	1.3	564	1.2	559	0.9
779.000	9.2	812	1516	4.5	1498	4.4	1527	5.0	1512	4.8	1527	4.7	1516	3.9
865.000	6.2	666	1243	3.5	1213	3.4	1240	3.8	1247	3.5	1250	2.7	1239	2.7
885.000	6.0	395	823	1.7	801	1.6	814	2.0	824	1.5	831	1.6	819	1.1
900.000	4.7	308	690	1.6	673	1.2	683	1.6	693	1.6	698	1.4	688	1.0
940.000	2.4	203	534	1.2	522	1.2	525	1.0	539	1.1	542	1.3	532	0.7
1020.000	3.9	152	345	0.9	337	0.8	348	0.7	345	0.8	351	0.8	345	0.5

2.4.1.2 OLCI-B

SNR computed for all OLCI-B calibration data (S01, S04 (but not the dark-only S04) and S05 sequences) as a function of band number is presented in Figure 42.

SNR computed for all OLCI-B calibration data as a function of orbit number for band Oa01 (the less stable band) is presented in Figure 43.

As for OLCI-A the SNR is very stable in time. There is no significant evolution of this parameter during the current reporting and the ESA requirement is fulfilled for all bands.

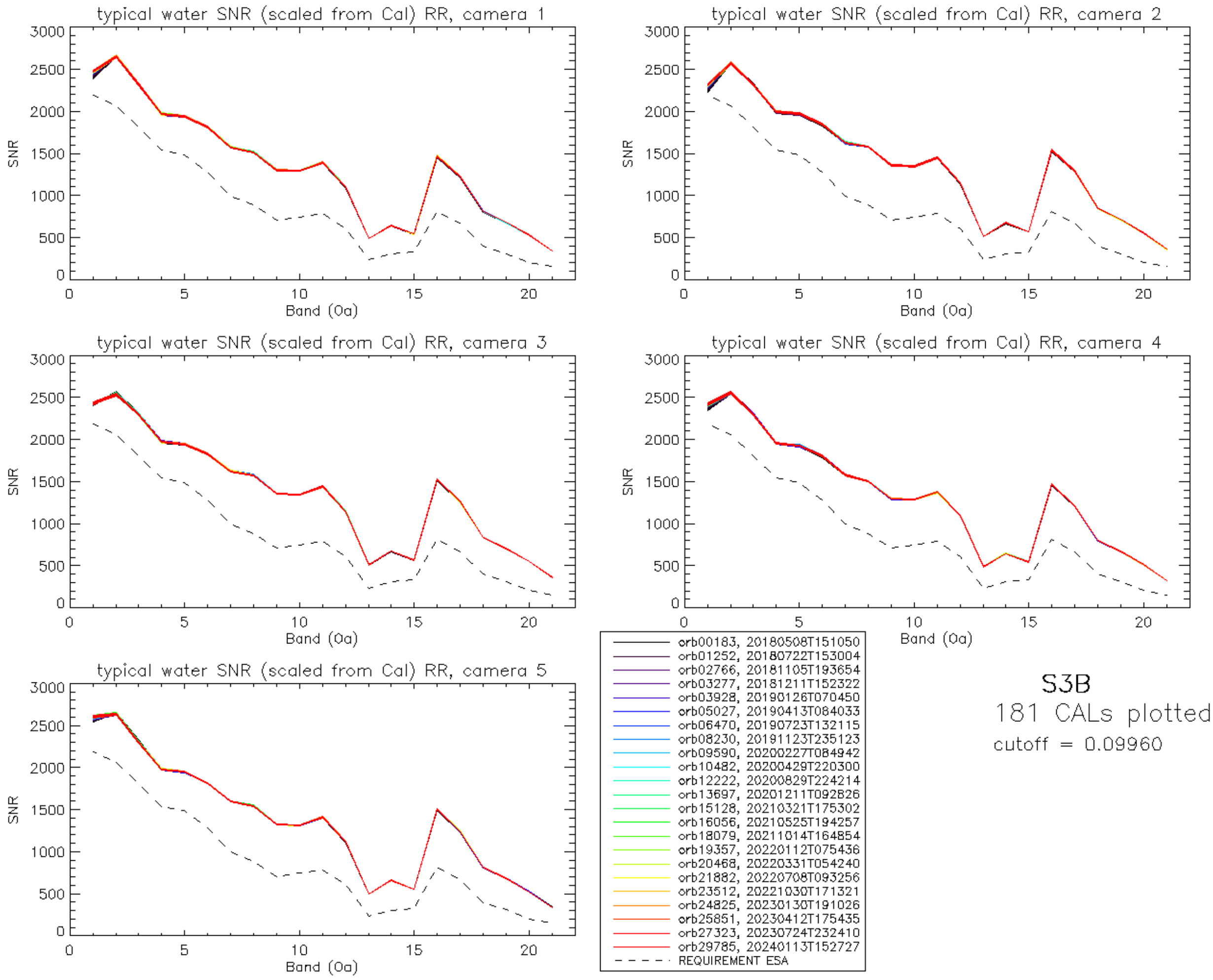

Figure 42: OLCI-B Signal to Noise ratio as a function of the spectral band for the 5 cameras. These results have been computed from radiometric calibration data. All calibrations except first one (orbit 167) are presents with the colours corresponding to the orbit number (see legend). The SNR is very stable with time: the curves for all orbits are almost superimposed. The dashed curve is the ESA requirement.

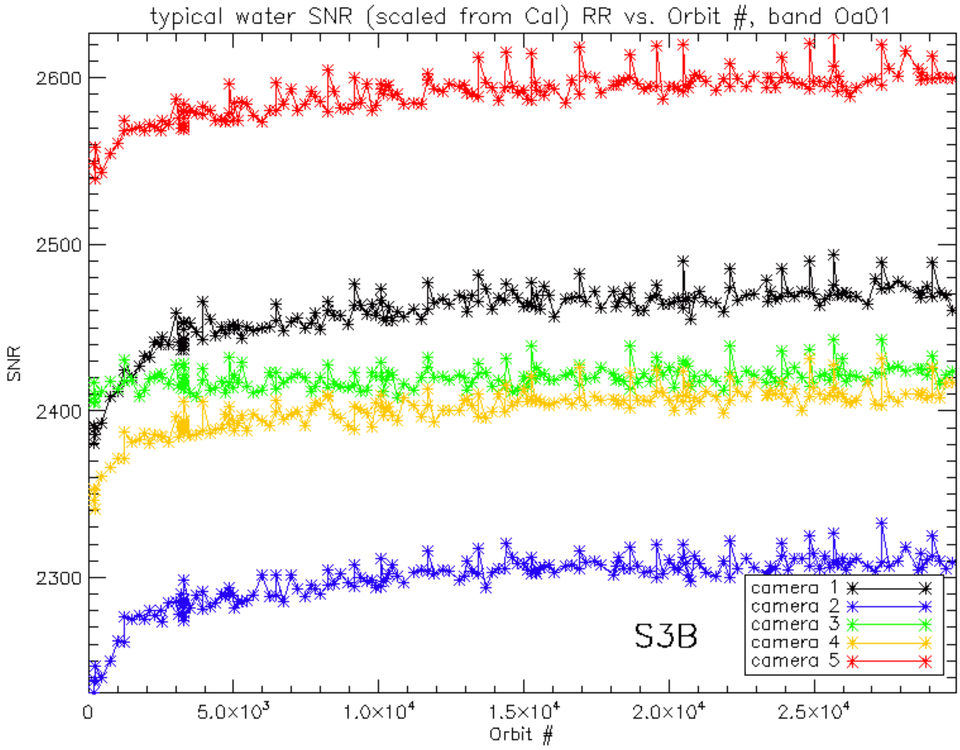

Figure 43: long-term stability of the OLCI-B SNR estimates from Calibration data, example of channel Oa1.

Table 2: OLCI-B SNR figures as derived from Radiometric Calibration data. Figures are given for each camera (time average and standard deviation), and for the whole instrument. The requirement and its reference radiance level are recalled (in mW.sr^{-1}.m^{-2}.nm^{-1}).

	L_{ref}	SNR	C1		C2		C3		C4		C5		All	
nm	LU	RQT	avg	*std*	avg	*std*	avg	*std*	avg	*std*	avg	*std*	avg	*std*
400.000	63.0	2188	2459	18.4	2298	16.4	2420	6.7	2401	13.9	2590	14.3	2434	13.0
412.000	74.1	2061	2654	7.1	2568	6.8	2541	9.1	2550	6.6	2636	8.1	2590	6.0
442.000	65.6	1811	2323	7.0	2315	6.4	2298	7.2	2301	7.2	2307	6.9	2309	6.0
490.000	51.2	1541	1966	4.8	1990	5.5	1971	5.0	1952	4.6	1979	4.5	1972	3.8
510.000	44.4	1488	1939	4.9	1969	6.1	1942	4.9	1925	4.9	1951	4.7	1945	4.0
560.000	31.5	1280	1813	4.6	1848	4.8	1829	4.6	1805	4.6	1817	3.9	1822	3.5
620.000	21.1	997	1572	4.3	1625	4.5	1624	3.8	1576	3.6	1600	3.6	1600	2.9
665.000	16.4	883	1513	4.0	1578	3.8	1573	3.7	1501	3.1	1546	3.6	1542	2.8
674.000	15.7	707	1300	3.9	1358	3.5	1353	3.2	1292	2.6	1327	2.9	1326	2.3
681.000	15.1	745	1293	3.5	1347	3.3	1343	3.0	1285	2.8	1316	2.8	1317	2.2
709.000	12.7	785	1390	3.9	1447	3.9	1443	4.1	1373	2.9	1412	3.6	1413	2.9
754.000	10.3	605	1096	3.5	1143	3.5	1142	3.2	1090	2.8	1116	3.1	1117	2.7
761.000	6.1	232	488	1.1	509	1.2	509	1.3	486	1.2	498	1.3	498	0.9
764.000	7.1	305	643	1.6	673	2.0	672	1.8	642	1.8	658	1.8	658	1.5
768.000	7.6	330	541	1.4	568	1.4	564	1.3	541	1.3	555	1.5	554	1.0
779.000	9.2	812	1467	4.0	1536	4.7	1527	5.0	1468	4.0	1507	4.1	1501	3.6
865.000	6.2	666	1221	3.4	1288	3.7	1258	3.5	1206	3.5	1238	2.8	1242	2.7
885.000	6.0	395	808	2.1	848	1.9	834	1.9	799	1.8	815	2.1	821	1.4
900.000	4.7	308	679	1.5	714	1.9	704	1.7	670	1.5	683	1.5	690	1.2
940.000	2.4	203	527	1.3	549	1.5	551	1.2	510	1.1	522	1.3	532	0.9
1020.000	3.9	152	336	0.8	358	1.1	358	0.8	318	0.7	338	0.9	342	0.6

2.5 Geometric Calibration/Validation

2.5.1 OLCI-A

OLCI-A georeferencing performance is compliant since the introduction of MPC Geometric Calibration, put in production on the 14th of March 2018. It has however significantly improved after its last full revision of GCMs (Geometric Calibration Models, or platform to instrument alignment quaternions) and IPPVMs (Instrument Pixels Pointing Vectors) both derived using the GeoCal Tool and put in production on 30/07/2019.

The following figures (Figure 44 to Figure 49) show time series of the overall RMS performance (requirement criterion) and of the across-track and along-track biases for each camera. New plots (Figure 50 and Figure 51) introduce monitoring of the performance homogeneity within the field of view: georeferencing errors in each direction at camera transitions (difference between last pixel of camera N and first pixel of camera N+1) and within a given camera (maximum bias minus minimum inside each camera). The performance improvement since the 30/07/2019 is significant on most figures: the global RMS value decreases form around 0.35 to about 0.2 (Figure 44), the across-track biases decrease significantly for all cameras (Figure 45 to Figure 49), the along-track bias reduces for at least camera 3 (Figure 47) and the field of view homogeneity improves drastically (Figure 50 and Figure 51, but also reduction of the dispersion – distance between the ± 1 sigma lines – in Figure 45 to Figure 49).

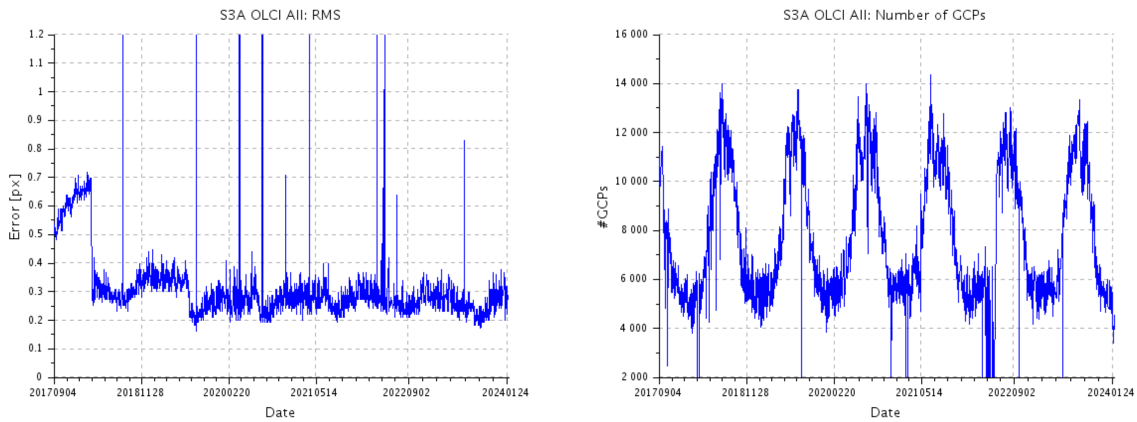

Figure 44: overall OLCI-A georeferencing RMS performance time series (left) and number of validated control points corresponding to the performance time series (right) over the whole monitoring period

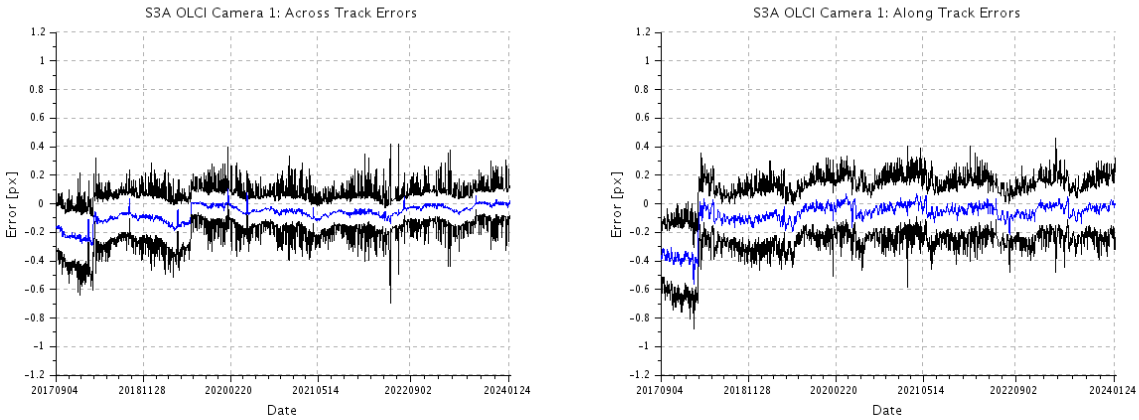

Figure 45: across-track (left) and along-track (right) OLCI-A georeferencing biases time series for Camera 1. Blue line is the average, black lines are average plus and minus 1 sigma.

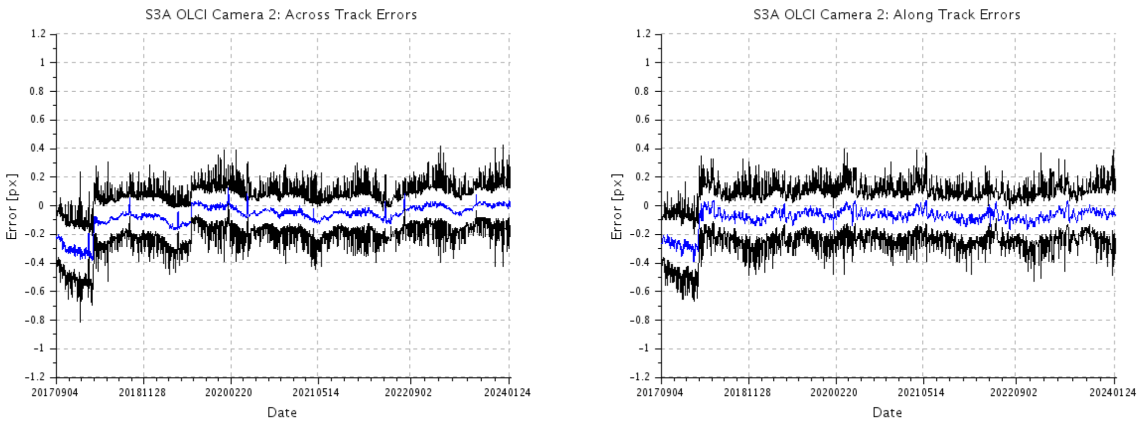

Figure 46: same as Figure 45 for Camera 2.

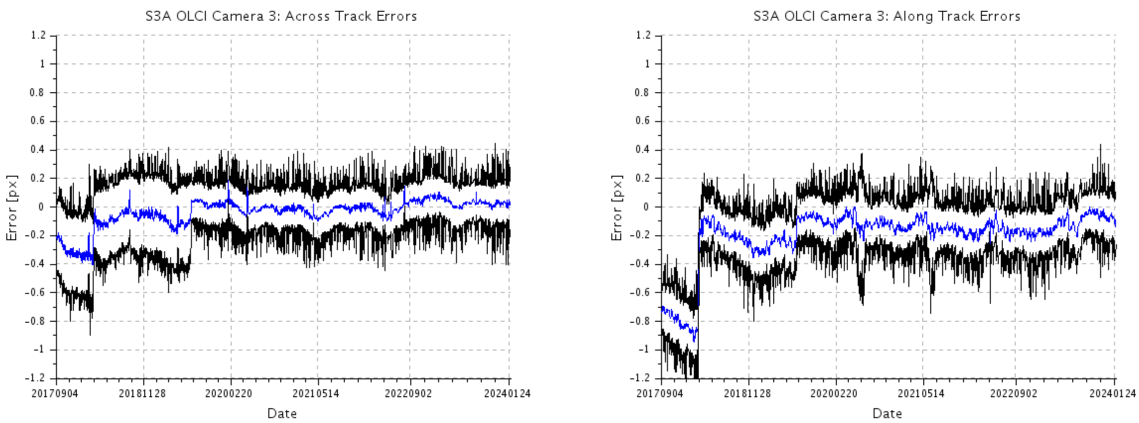

Figure 47: same as Figure 45 for Camera 3.

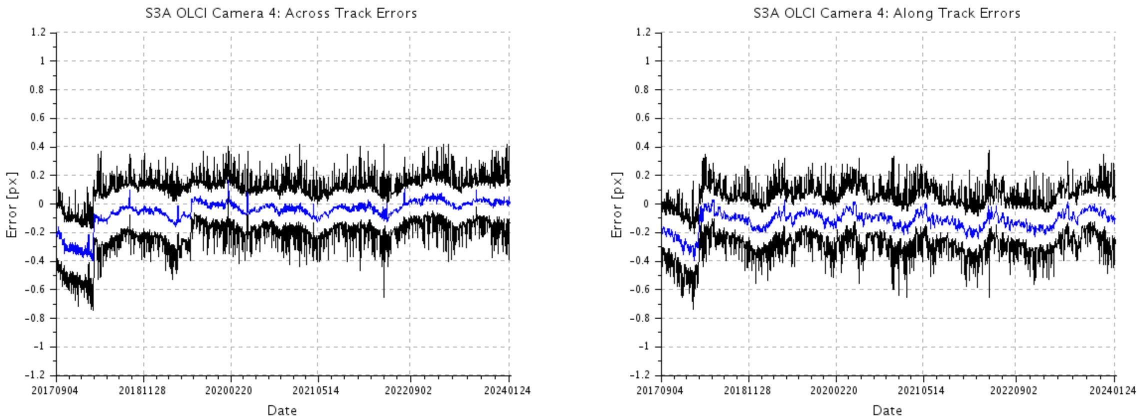

Figure 48: same as Figure 45 for Camera 4.

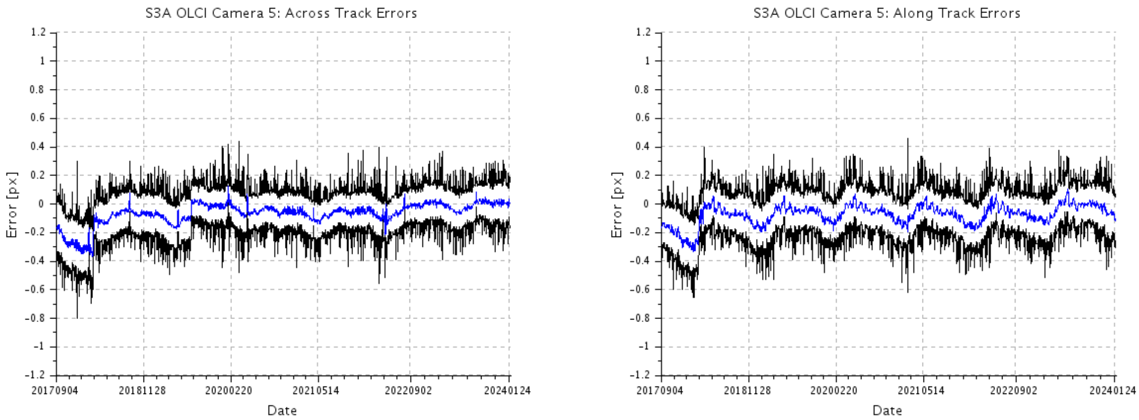

Figure 49: same as Figure 45 for Camera 5.

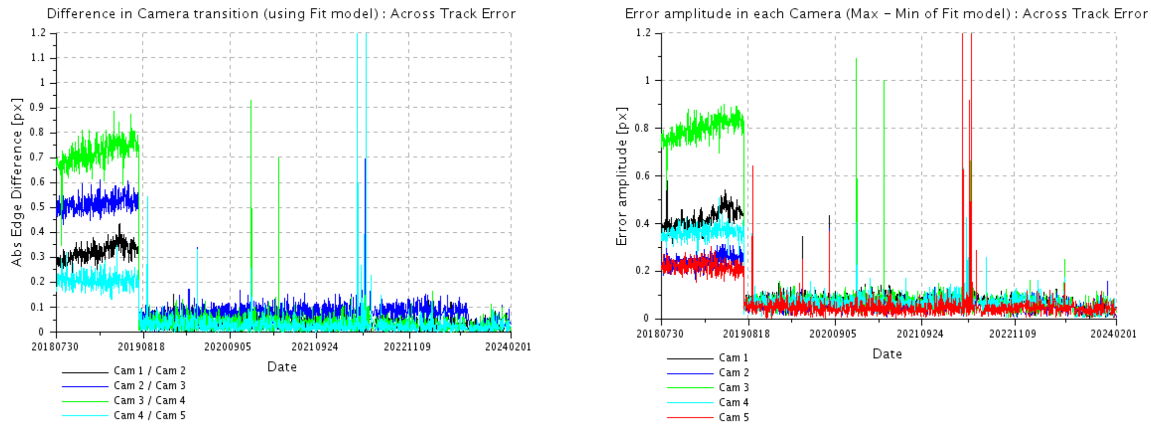

Figure 50: OLCI-A spatial across-track misregistration at each camera transition (left) and maximum amplitude of the across-track error within each camera (left).

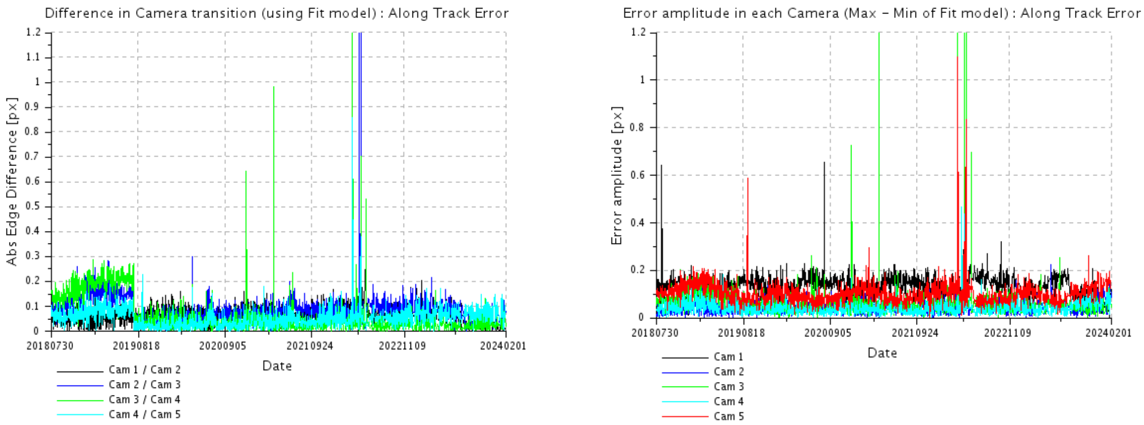

Figure 51: OLCI-A spatial along-track misregistration at each camera transition (left) and maximum amplitude of the along-track error within each camera (left).

2.5.2 OLCI-B

Georeferencing performance of OLCI-B improved significantly with the fourth geometric calibration introduced the 30/07/2019. However, the instrument pointing is still evolving, in particular for camera 2 (Figure 58) and a new geometric calibration has been done and introduced in the processing chain on the 16th of April 2020. Its impact is significant on the along-track biases of all cameras (Figure 53 to Figure 57), but also on the continuity at camera interfaces (Figure 58, left) and on intra-camera homogeneity (Figure 58, right). Since then, further adjustments to the geometric calibration have been introduced, mainly to correct the along-track drifts. The most recent was put in production on 29/07/2021 and its effect can be seen e.g. on left graphs of Figure 54, Figure 55 and Figure 57 (across-track biases of cameras 2, 3 & 5).

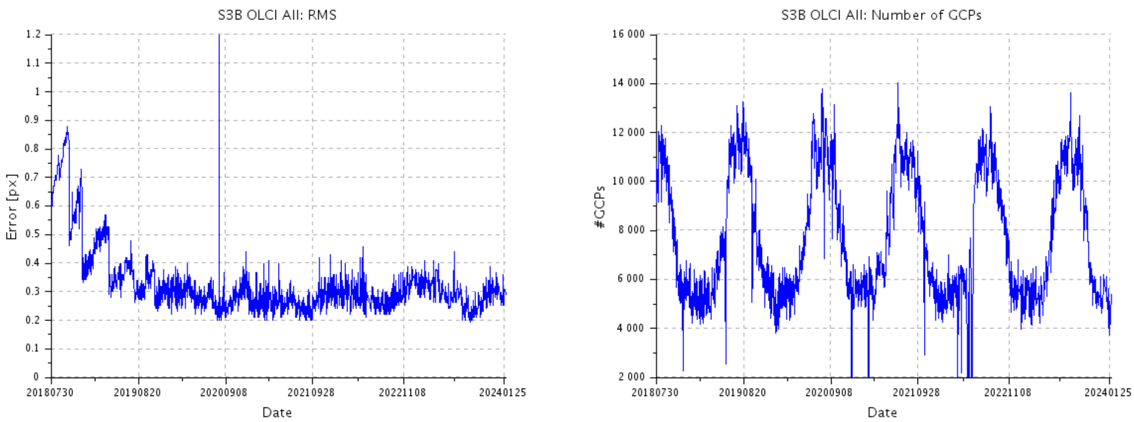

Figure 52: overall OLCI-B georeferencing RMS performance time series over the whole monitoring period (left) and corresponding number of validated control points (right)

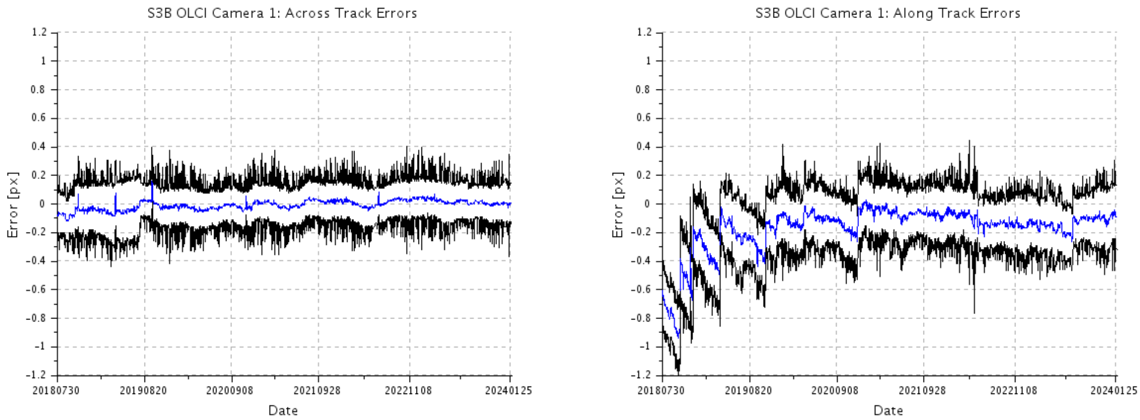

Figure 53: across-track (left) and along-track (right) OLCI-B georeferencing biases time series for Camera 1.

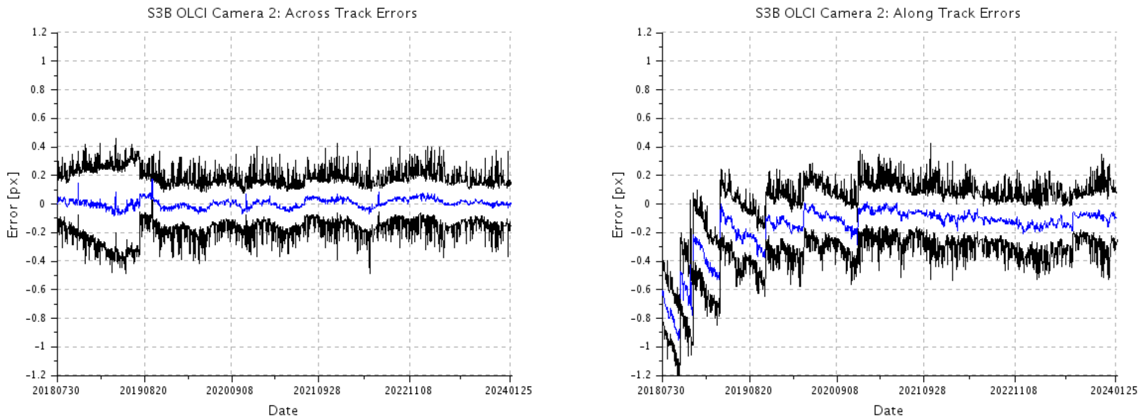

Figure 54: same as Figure 53 for Camera 2.

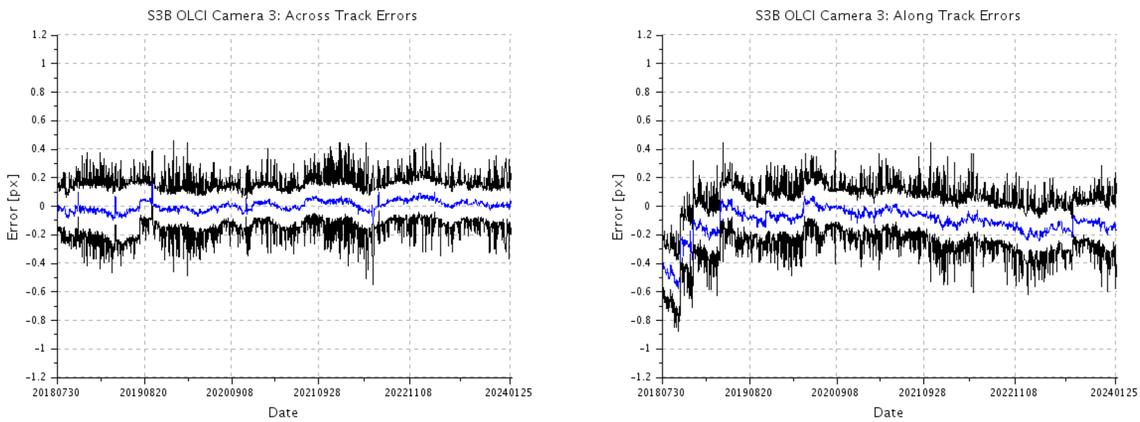

Figure 55: same as Figure 53 for Camera 3.

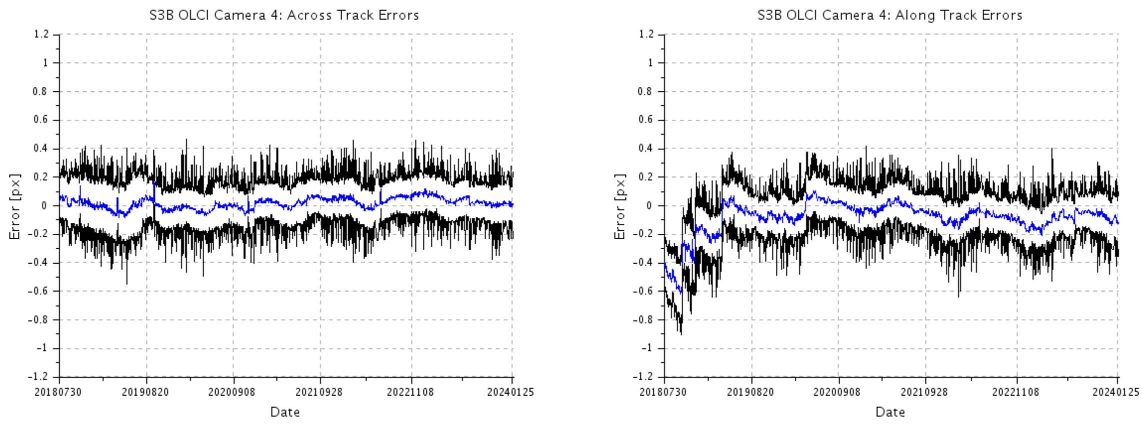

Figure 56: same as Figure 53 for Camera 4.

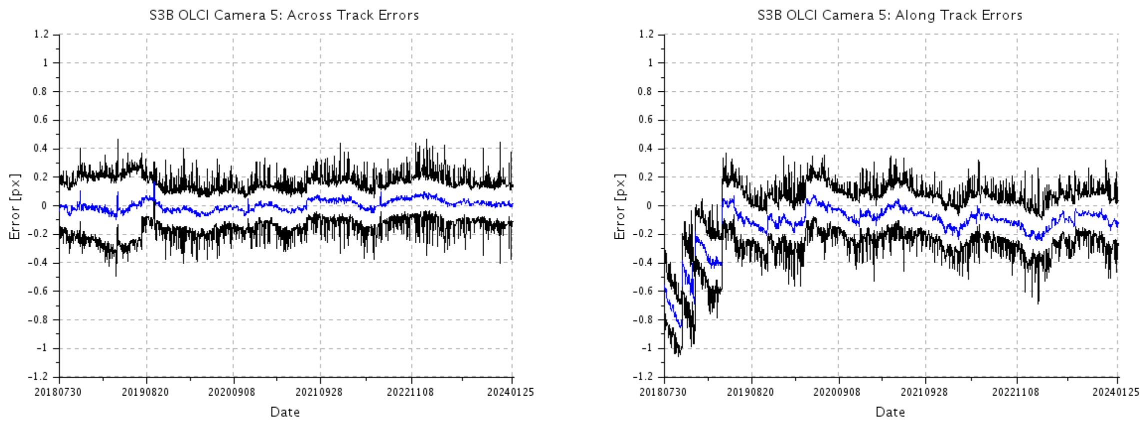

Figure 57: same as Figure 53 for Camera 5.

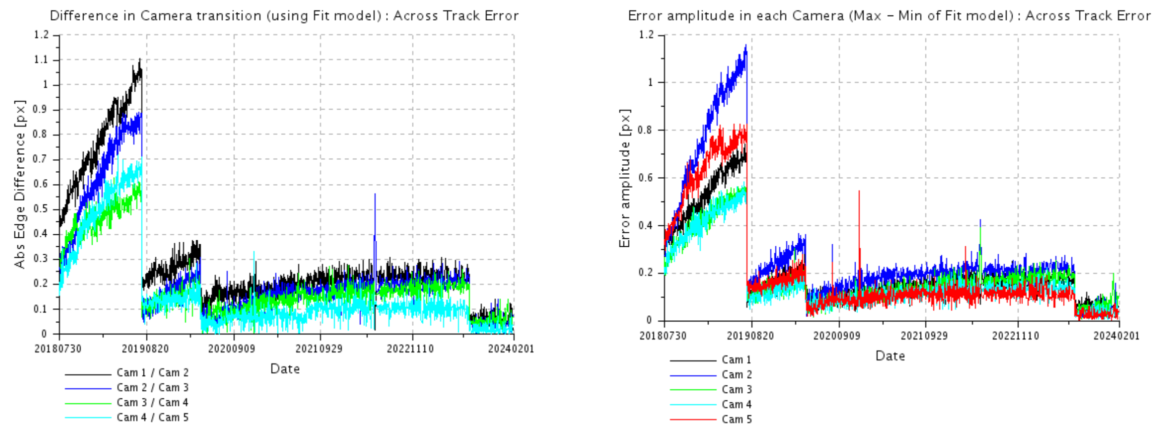

Figure 58: OLCI-B spatial across-track misregistration at each camera transition (left) and maximum amplitude of the across-track error within each camera (left).

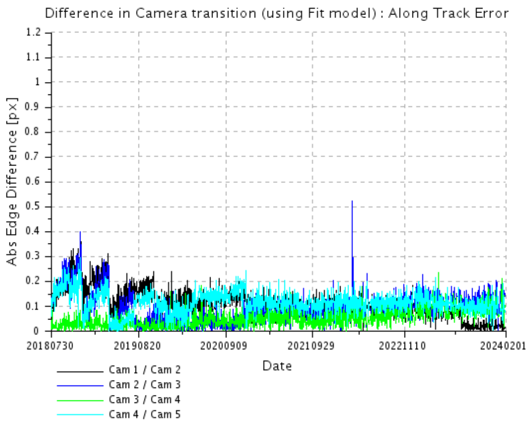

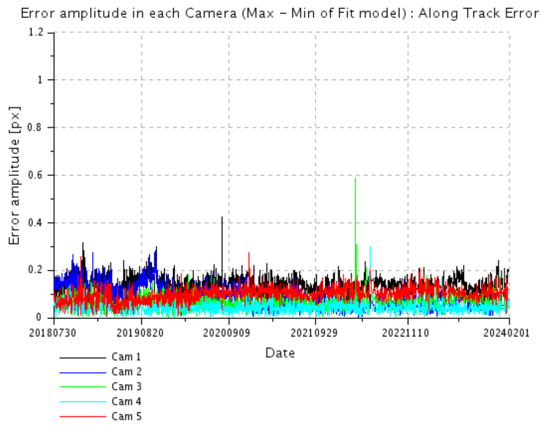

Figure 59: OLCI-B spatial along-track misregistration at each camera transition (left) and maximum amplitude of the along-track error within each camera (left).

3 OLCI Level 1 Product validation

3.1 [OLCI-L1B-CV-300], [OLCI-L1B-CV-310] – Radiometric Validation

3.1.1 S3ETRAC Service

Activities done

The S3ETRAC service extracts OLCI L1 RR and SLSTR L1 RBT data and computes associated statistics over 49 sites corresponding to different surface types (desert, snow, ocean maximizing Rayleigh signal, ocean maximizing sunglint scattering and deep convective clouds). The S3ETRAC products are used for the assessment and monitoring of the L1 radiometry (optical channels) by the ESLs.

All details about the S3ETRAC/OLCI and S3ETRAC/SLSTR statistics are provided on the S3ETRAC website http://s3etrac.acri.fr/index.php?action=generalstatistics.

- Number of OLCI products processed by the S3ETRAC service
- Statistics per type of target (DESERT, SNOW, RAYLEIGH, SUNGLINT and DCC)
- Statistics per sites
- Statistics on the number of records

For illustration, we provide below statistics on the number of S3ETRAC/OLCI records generated per type of targets (DESERT, SNOW, RAYLEIGH, SUNGLINT and DCC) for both OLCI-A (Figure 60) and OLCI-B (Figure 61).

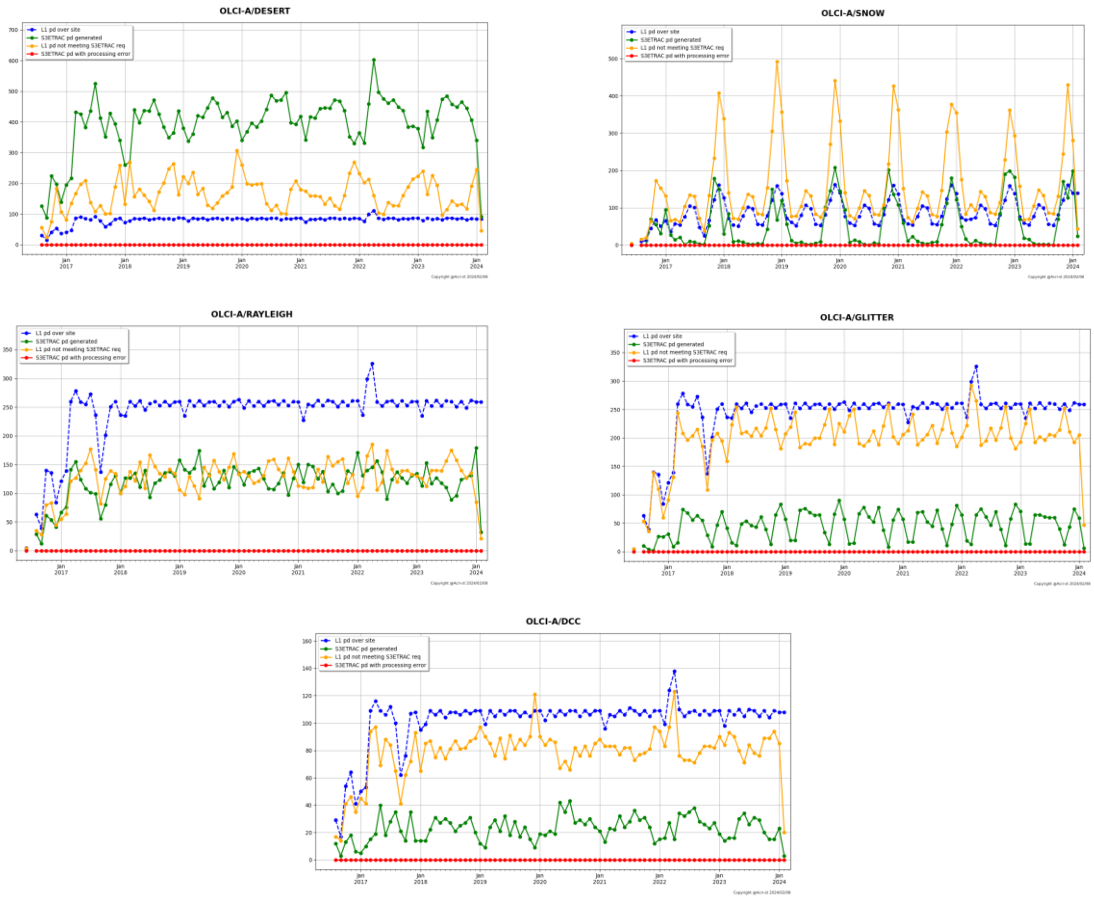

Figure 60: summary of S3ETRAC products generation for OLCI-A
(number of OLCI-A L1 products Ingested, blue – number of S3ETRAC extracted products generated, green – number of S3ETRAC runs without generation of output product (data not meeting selection requirements), yellow – number of runs ending in error, red, one plot per site type).

Figure 61: summary of S3ETRAC products generation for OLCI-B
(number of OLCI-B L1 products Ingested, yellow – number of S3ETRAC extracted products generated, blue – number of S3ETRAC runs without generation of output product (data not meeting selection requirements), green – number of runs ending in error, red, one plot per site type).

3.1.2 Radiometric validation with DIMITRI

OLCI-A and OLCI-B L1B radiometry verification has been processed as follow:

- The verification is performed over Desert-sites **until end-January 2024.**
- The verification is performed over Ocean-sites **until end-January 2024.**
- All results from OLCI-A and OLCI-B over Rayleigh, Glint and PICS are consistent with the previous reporting period over the used CalVal sites.
- Good stability of both sensors OLCI-A and OLCI-B could be observed, nevertheless the time-series average shows higher reflectance from OLCI-A.
- Bands with high gaseous absorption are excluded.

3.1.2.1 Verification and Validation over PICS

1. The ingestion of all the available L1B-LN1-NT products from OLCI-A and OLCI-B over the 6 desert CalVal-sites (Algeria3 & 5, Libya 1 & 4 and Mauritania 1 & 2) has been performed **until end-January 2024**.
2. The results are consistent over all the six used PICS sites (Figure 62 and Figure 63). Both sensors show a good stability over the analysed period.
3. The temporal average over the period **January 2024** of the elementary ratios (observed reflectance to the simulated one) for **OLCI-A** shows gain values between 2-4% over all the VNIR bands (Figure 64). Unlikely, the temporal average over the same period of the elementary ratios for **OLCI-B** shows gain values within 2% (mission requirements) over the VNIR spectral range (Figure 64). The spectral bands with significant absorption from water vapor and O_2 (Oa11, Oa13, Oa14, Oa15 and Oa20) are excluded.

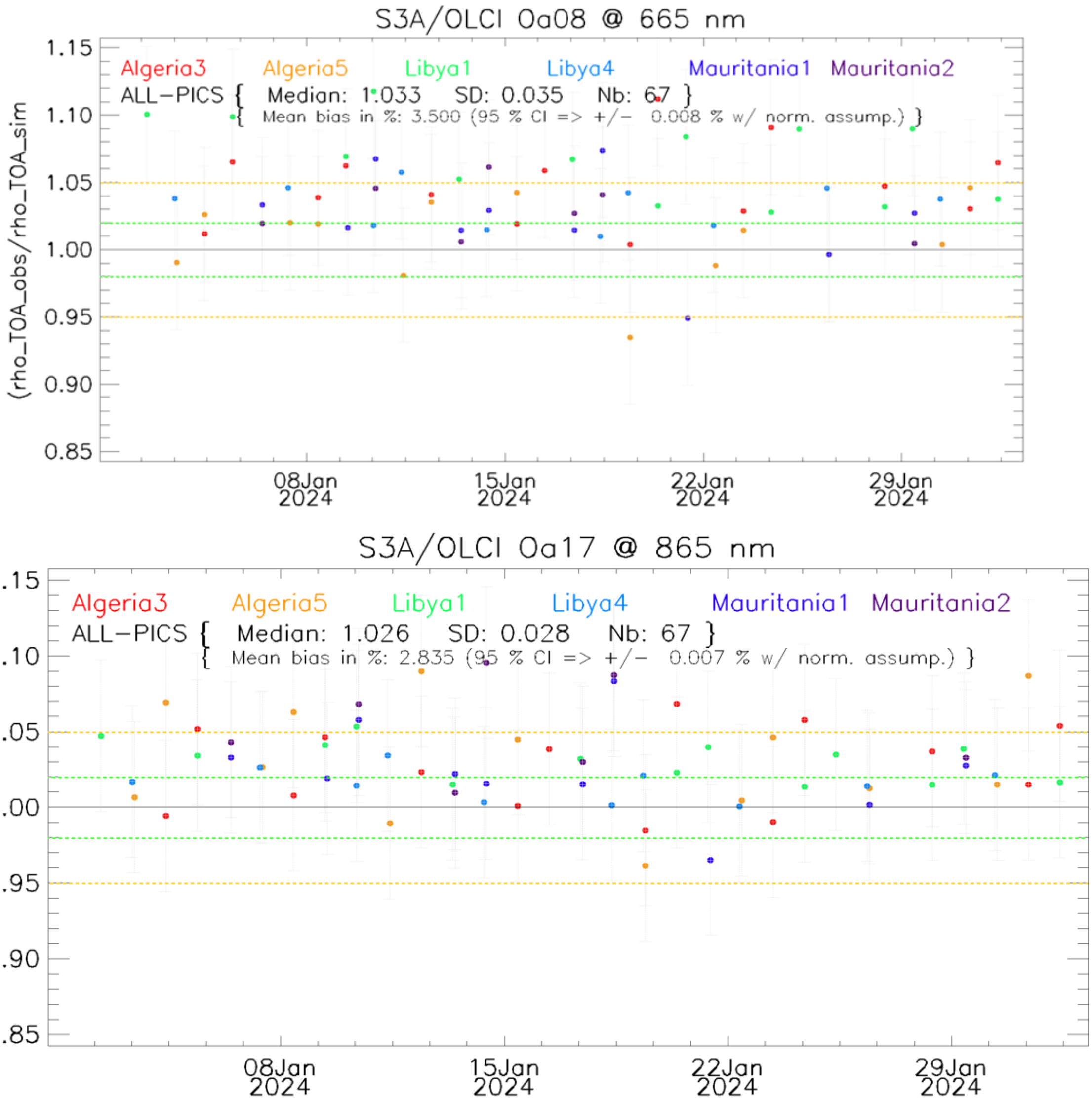

Figure 62: Time-series of the elementary ratios (observed/simulated) signal from OLCI-A for (top to bottom) bands Oa03 and Oa17 respectively over January 2024 from the six PICS Cal/Val sites. Dashed-green and orange lines indicate the 2% and 5% respectively. Error bars indicate the desert methodology uncertainty.

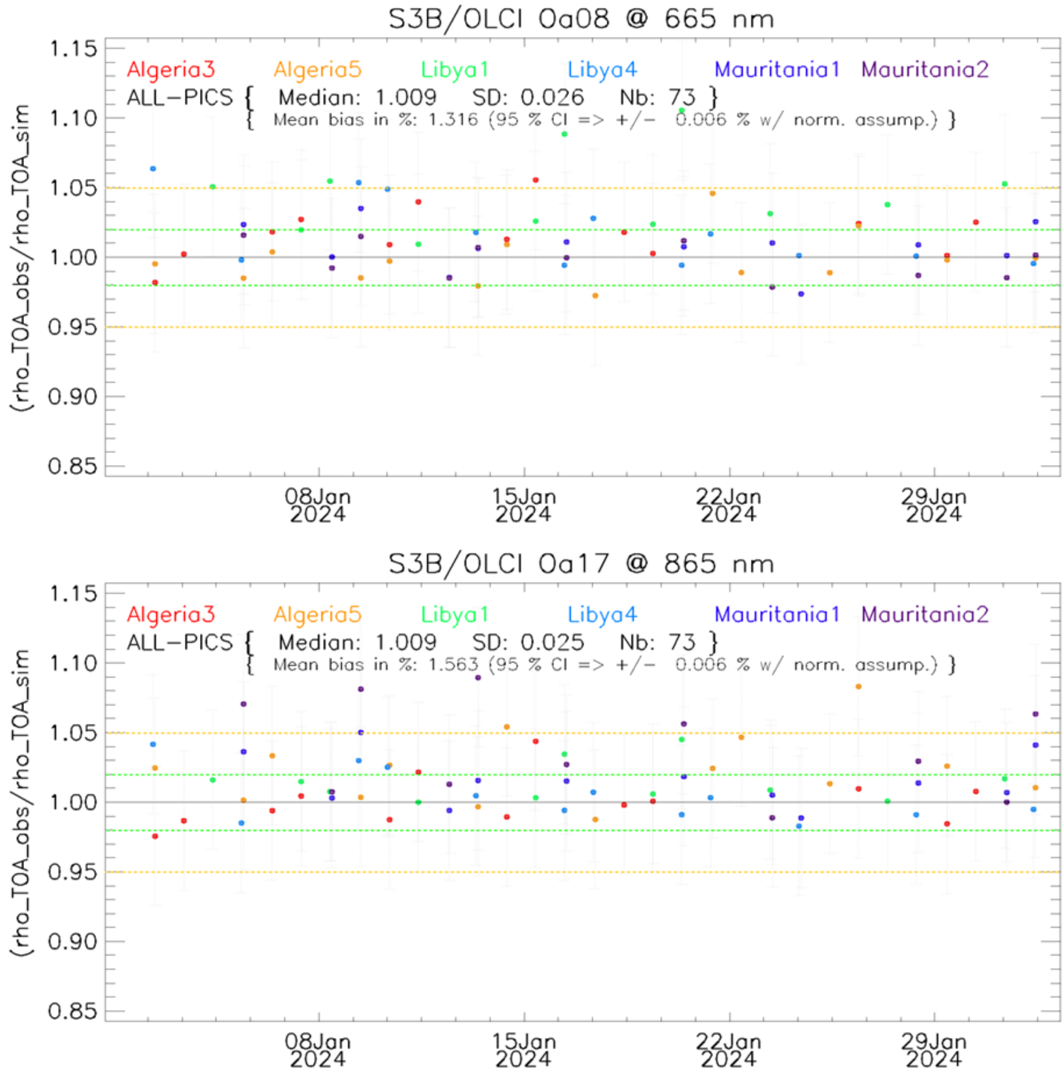

Figure 63: Time-series of the elementary ratios (observed/simulated) signal from OLCI-B for (top to bottom) bands Oa08 and Oa17 respectively over January 2024 from the six PICS Cal/Val sites. Dashed-green and orange lines indicate the 2% and 5% respectively. Error bars indicate the desert methodology uncertainty.

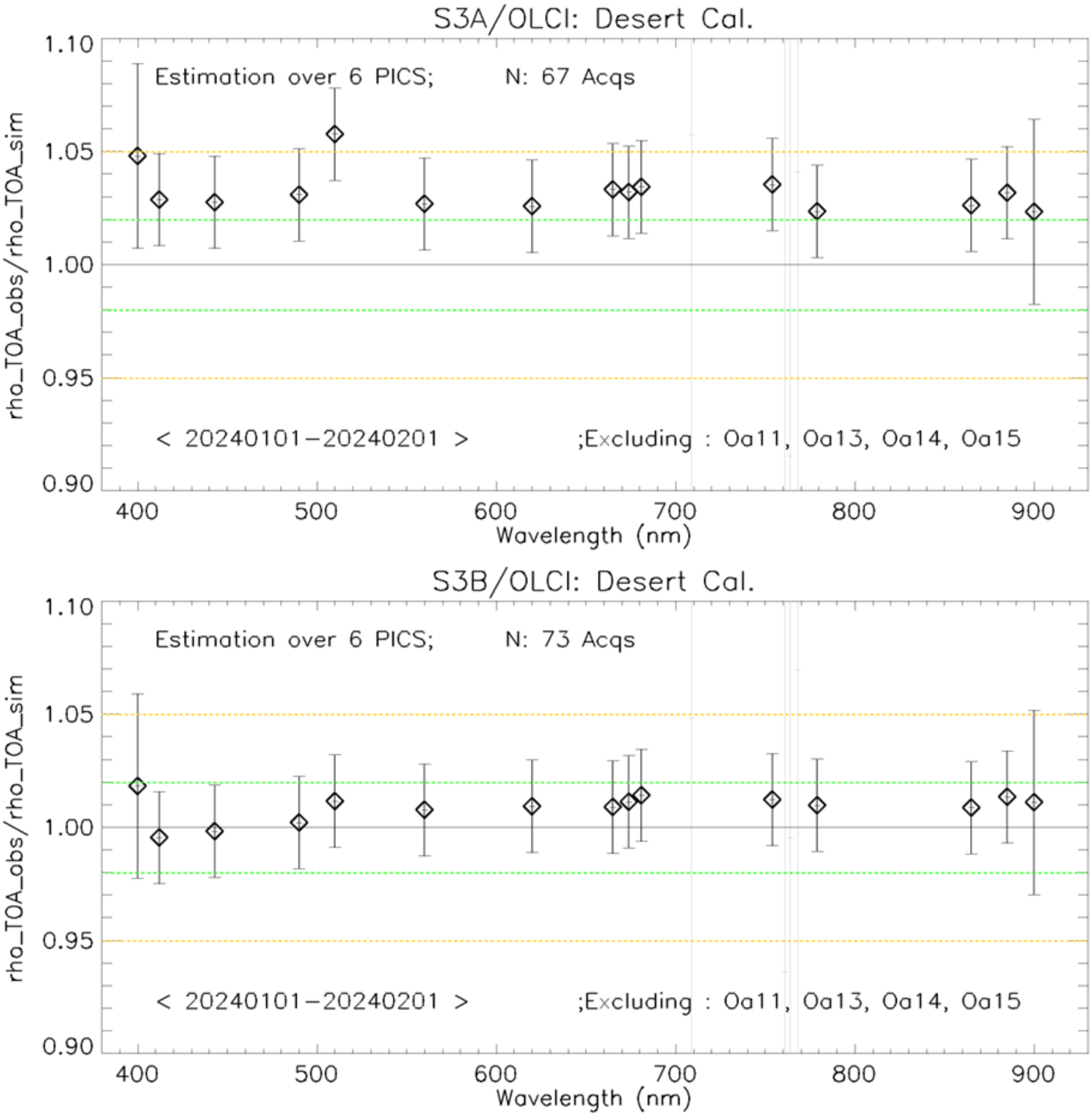

Figure 64: The estimated gain values for OLCI-A and OLCI-B over the 6 PICS sites identified by CEOS over the period January 2024 as a function of wavelength. Dashed-green and orange lines indicate the 2% and 5% respectively. Error bars indicate the desert methodology uncertainty.

3.1.2.2 Validation over Rayleigh

Rayleigh method has been performed from the available mini-files over the period **January 2023- End January 2024** for OLCI-A and OLCI-B. The results were produced with the configuration (ROI-AVERAGE). The gain coefficients of OLCI-A are consistent with the previous results. Bands Oa01-Oa05 display biases values between 3%-5% while bands Oa06-Oa09 exhibit biases about 2%, just within the mission requirement (Figure 65). The gain coefficients of OLCI-B are lower than OLCI-A ones, where bands Oa01-Oa05 display biases values about 2-5%, when bands Oa6-Oa9 exhibit biases within the 2% mission requirement (Figure 65).

3.1.2.3 Validation over Glint and synthesis

Glint calibration method has been performed over the period **January 2023- End January 2024**for OLCI-A and OLCI-B. The outcome of this analysis shows a good consistency with the desert and Rayleigh outputs over the NIR spectral range Oa06-Oa09 for both sensors. Glint results from OLCI-A show that the NIR bands are within 3% (slightly above the 2% mission requirements), except Oa21 which shows higher biases of about 6% and 4% for both sensors respectively (see Figure 65). Again, the glint gain from OLCI-B looks slightly lower than OLCI-A one with most bands within the 2% mission requirement if ignoring the Rayleigh results in the blue-green region and Oa21.

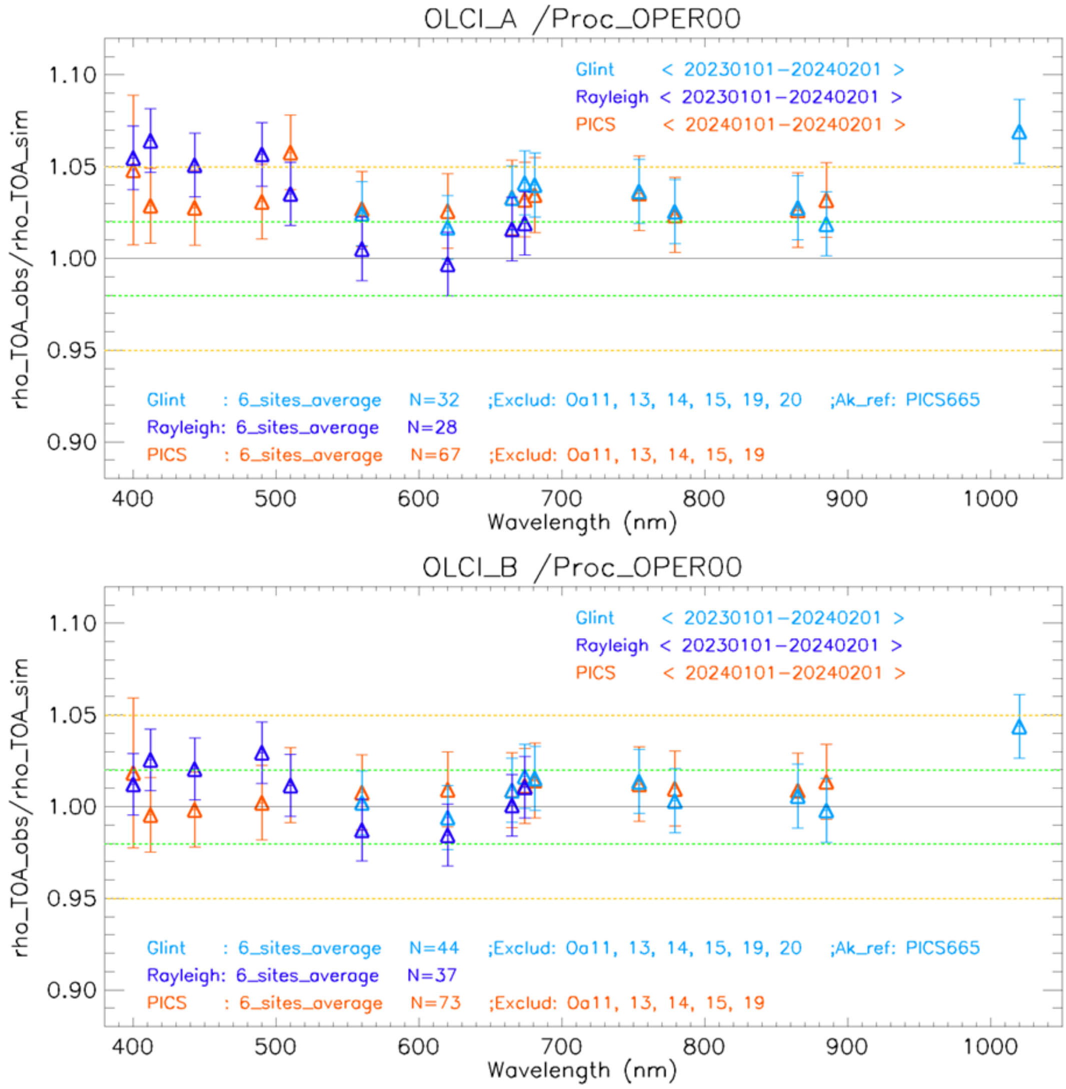

Figure 65: The estimated gain values for OLCI-A and OLCI-B from Glint, Rayleigh and PICS methods over the period January 2022 – end December 2023 as a function of wavelength. We use the gain value of Oa8 from PICS-Desert method as reference gain for Glint method. Dashed-green and orange lines indicate the 2% and 5% respectively. Error bars indicate the method uncertainties.

3.1.2.4 Cross-mission Intercomparison over PICS:

X-mission Intercomparison between MERIS, MSI-A, MSI-B, OLCI-A, OLCI-B, SLSTR-A and SLSTR-B has been performed over the 6 PICS-test-sites.

Figure 66 shows the estimated gain over different time-series for different sensors over PICS. The spectral bands with significant absorption from water vapor and O2 are excluded. OLCI-A seems to have higher gain wrt the other sensors (except SLSTR-A/B), and of about 1-3% higher gain wrt to OLCI-B over VNIR spectral range.

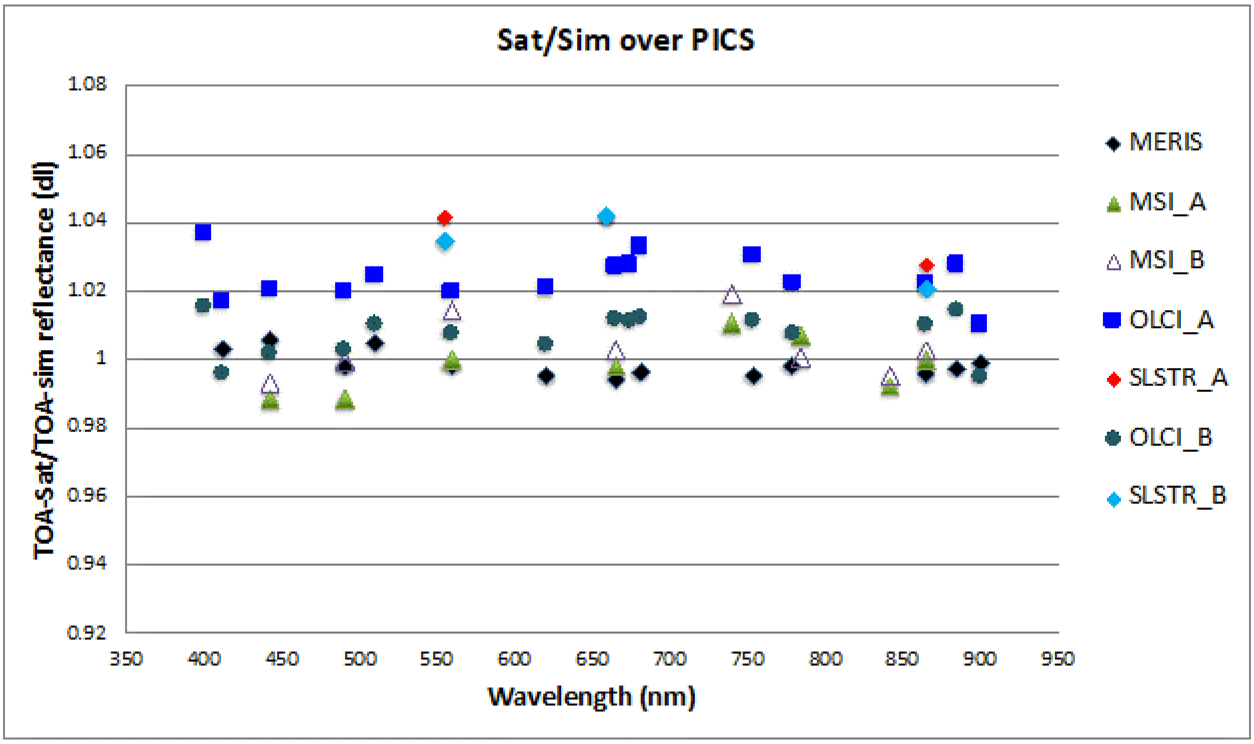

Figure 66: Ratio of observed TOA reflectance to simulated one for (black) MERIS, (pale-green) S2A/MSI, (white) S2B/MSI, (blue) S3A/OLCI, (green) S3B/OLCI, (red) S3A/SLSTR-NADIR, and (cyan) S3B/SLSTR-NADIR averaged over the six PICS test sites over different periods as a function of wavelength.

3.1.3 Radiometric validation with OSCAR

3.1.3.1 OSCAR Rayleigh results

The OSCAR Rayleigh have been applied to the S3A and S3B S3ETRAC data from the 6 oceanic calibration sites (Table 3) using a new chlorophyll climatology which has been derived from the CMEMS OLCI monthly CHL products from considering the years 2017, 2018 and 2019.

Table 3: S3ETRAC Rayleigh Calibration sites

Site Name	Ocean	North Latitude	South Latitude	East Longitude	West Longitude
PacSE	South-East of Pacific	-20.7	-44.9	-89	-130.2
PacNW	North-West of Pacific	22.7	10	165.6	139.5
PacN	North of Pacific	23.5	15	200.6	179.4
AtlN	North of Atlantic	27	17	-44.2	-62.5
AtlS	South of Atlantic	-9.9	-19.9	-11	-32.3
IndS	South of Indian	-21.2	-29.9	100.1	89.5

In Figure 67 the average OSCAR OLCI-A and OLCI-B Rayleigh results are given for January. In Figure 68 and Table 4, the same results are given for all acquisitions of 2023 combined with those of January 2024.

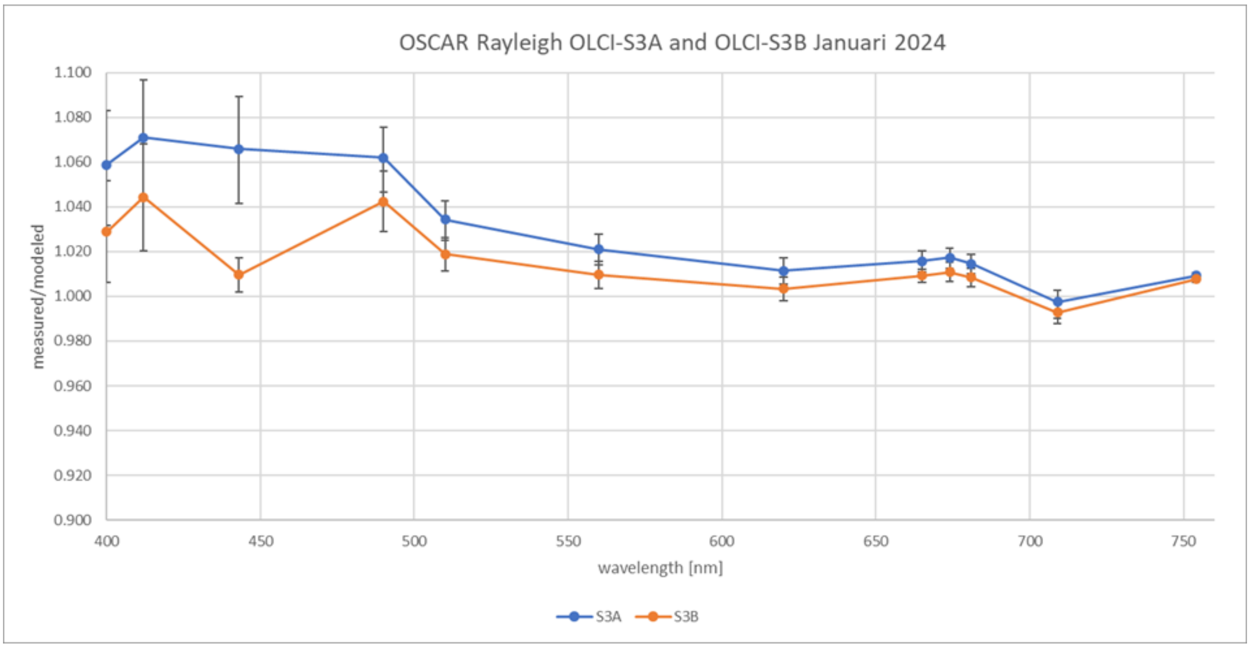

Figure 67: OSCAR Rayleigh S3A and S3B Calibration results as a function of wavelength for January 2024. The results are obtained with a new climatology derived from CMEMS OLCI monthly CHL products.

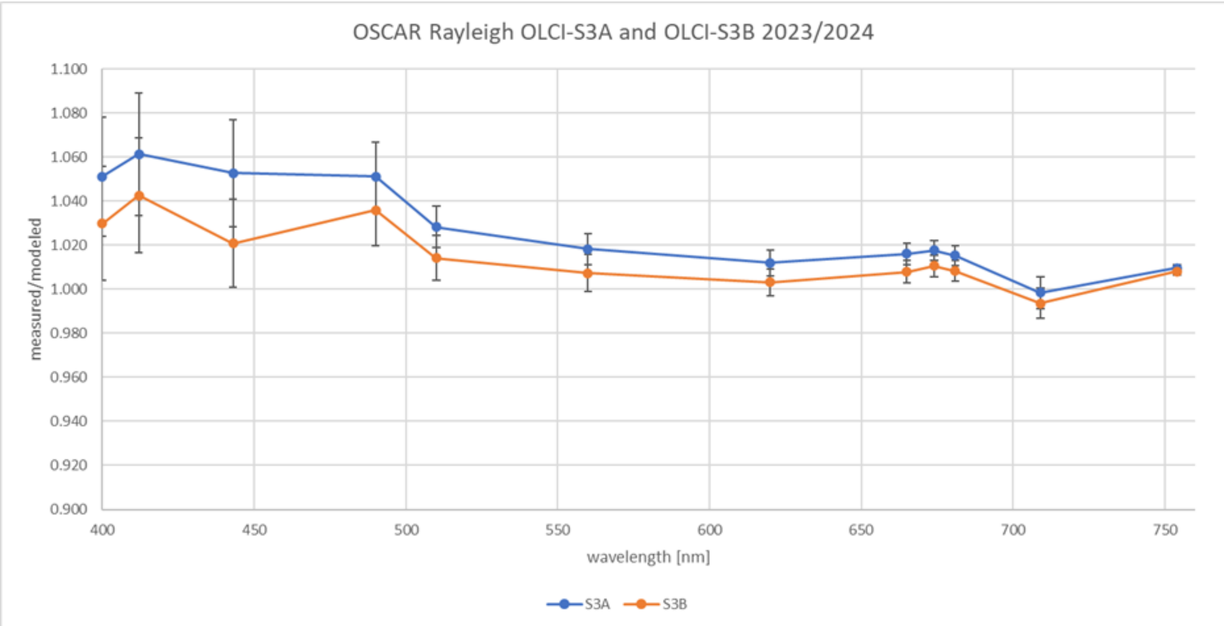

Figure 68: OSCAR Rayleigh OLCI-A and OLCI-B Calibration results as a function of wavelength for all acquisitions of 2023 and January 2024. The results are obtained with a new climatology derived from CMEMS OLCI monthly CHL products.

Table 4. OSCAR Rayleigh calibration results for S3A and S3B (average and standard deviation over all 2023 acquisitions and 2024) over all scenes currently (re)processed with the new climatology and observed difference (in %) between OLCIA and OLCIB

OLCI band	Wavelength (nm)	Oscar Rayleigh OLCIA avg	Oscar Rayleigh OLCIA stdev	Oscar Rayleigh OLCIB avg	Oscar Rayleigh OLCIB stdev	% difference OLCIA and OLCIB
Oa01	400	1.051	0.027	1.030	0.026	2.03%
Oa02	412	1.061	0.028	1.043	0.026	1.77%
Oa03	443	1.053	0.024	1.021	0.020	3.03%
Oa04	490	1.051	0.015	1.036	0.016	1.46%
Oa05	510	1.028	0.009	1.014	0.010	1.36%
Oa06	560	1.018	0.007	1.007	0.008	1.08%
Oa07	620	1.012	0.006	1.003	0.006	0.87%
Oa08	665	1.016	0.005	1.008	0.005	0.79%
Oa09	674	1.018	0.005	1.011	0.005	0.70%
Oa10	681	1.015	0.005	1.008	0.005	0.69%
Oa11	709	0.998	0.007	0.994	0.007	0.47%
Oa12	754	1.010	0.001	1.008	0.002	0.15%

3.1.3.2 OSCAR Glitter results

The OSCAR Glitter have been applied to all S3ETRAC glitter data for January 2024. Both OLCI-A and OLCI-B data was processed. The plots in Figure 69 are the glitter results for OLCI-A and OLCI-B for the period of January 2024 and on Figure 70 for all results of 2023 plus January 2024 (also provided in Table 5). The values are in absolute terms, since all bands are referenced to the Rayleigh result of band Oa8. The glitter method is a relative inter-band calibration method, since the Oa8 band is used to estimate windspeed. By multiplying all band results with the Rayleigh calibration factor for the same period, the results are referenced to the results of this method.

For all results of 2023-2024, the difference between OLCI-A and OLCI-B (Table 5, in %) is below 1% for all bands, except for bands Oa04 and Oa05. It also indicates a brighter OLCI-A compared to OLCI-B.

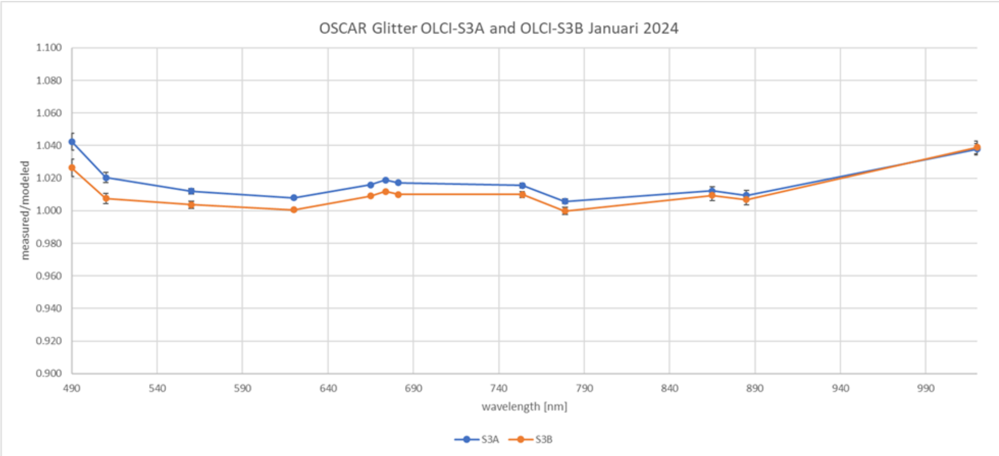

Figure 69: OSCAR Glitter OLCI-A & OLCI-B Calibration results as a function of wavelength for December 2023. The results are obtained with a new climatology derived from CMEMS OLCI monthly CHL products.

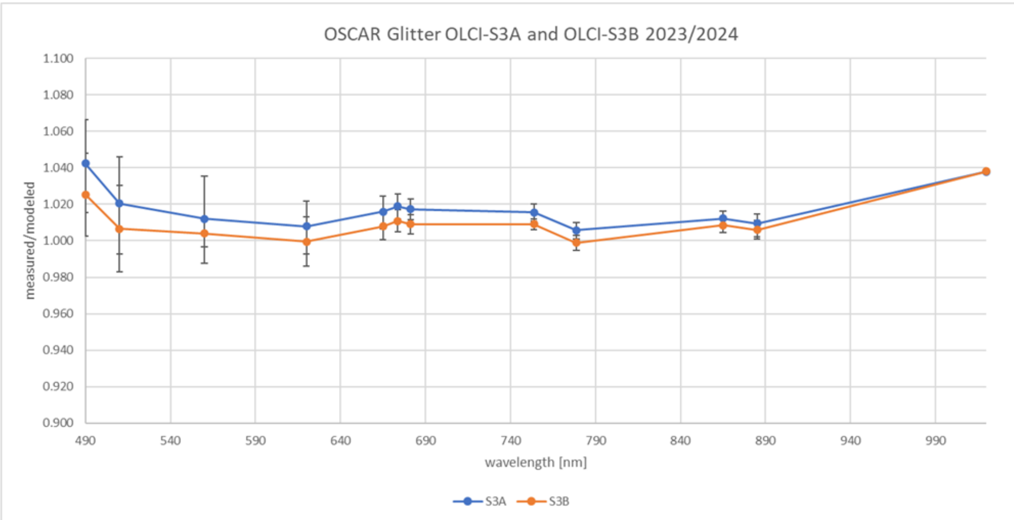

Figure 70: OSCAR Glitter OLCI-A & OLCI-B Calibration results as a function of wavelength for all acquisitions of 2023. The results are obtained with a new climatology derived from CMEMS OLCI monthly CHL products.

Table 5: OSCAR Glitter calibration results for OLCI-A and OLCI-B (average and standard deviation over all acquisitions of 2023) currently processed with the new climatology and observed difference (in %)

OLCI band	Wavelength	Oscar Glitter OLCIA		Oscar Glitter OLCIB		% difference OLCIA and OLCIB
	(nm)	avg	stdev	avg	stdev	
Oa04	490	1.042	0.005	1.025	0.005	1.64%
Oa05	510	1.020	0.003	1.007	0.003	1.35%
Oa06	560	1.012	0.002	1.004	0.003	0.78%
Oa07	620	1.008	0.001	1.000	0.001	0.83%
Oa08	665	1.016	0.000	1.008	0.000	0.79%
Oa09	673.75	1.019	0.001	1.011	0.001	0.79%
Oa10	681.25	1.017	0.001	1.009	0.001	0.81%
Oa12	753.75	1.016	0.002	1.009	0.002	0.63%
Oa16	778.75	1.006	0.002	0.999	0.002	0.69%
Oa17	865	1.012	0.002	1.009	0.003	0.37%
Oa18	885	1.009	0.003	1.006	0.003	0.35%
Oa21	1020	1.038	0.003	1.038	0.004	-0.02%

3.1.4 Radiometric validation with Moon observations: LIME results

There have been no new results during the reporting period. The latter figures (reported in OLCI Data Quality Report covering September 2023) are considered valid.

4 Level 2 Land products validation

4.1 [OLCI-L2LRF-CV-300]

4.1.1 Routine extractions

- The focus for this time period has been on the rolling archive Non Time Critical (NT) data until the 31st of December 2023. More data available for statistical analysis as a concatenation procedure for all available data in the MERMAID processing has been implemented.
- Concatenated time series of OLCI Global Vegetation Index and OLCI Terrestrial Chlorophyll Index have been regenerated on the current rolling archive availability including previous extractions since June 2016 and April 2018 for S3A and S3B respectively.

4.1.1.1 OLCI-A

Figure 71 to Figure 80 below present the Core Land Sites OLCI-A time series over the current period.

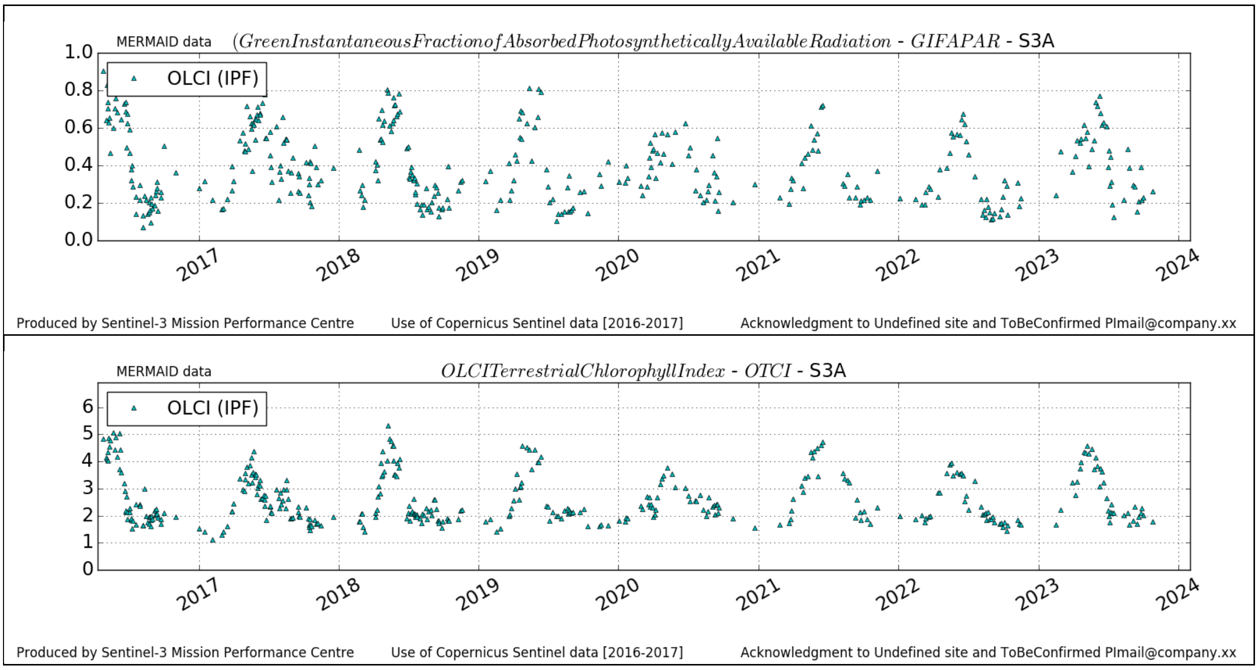

Figure 71: DeGeb time series over current report period

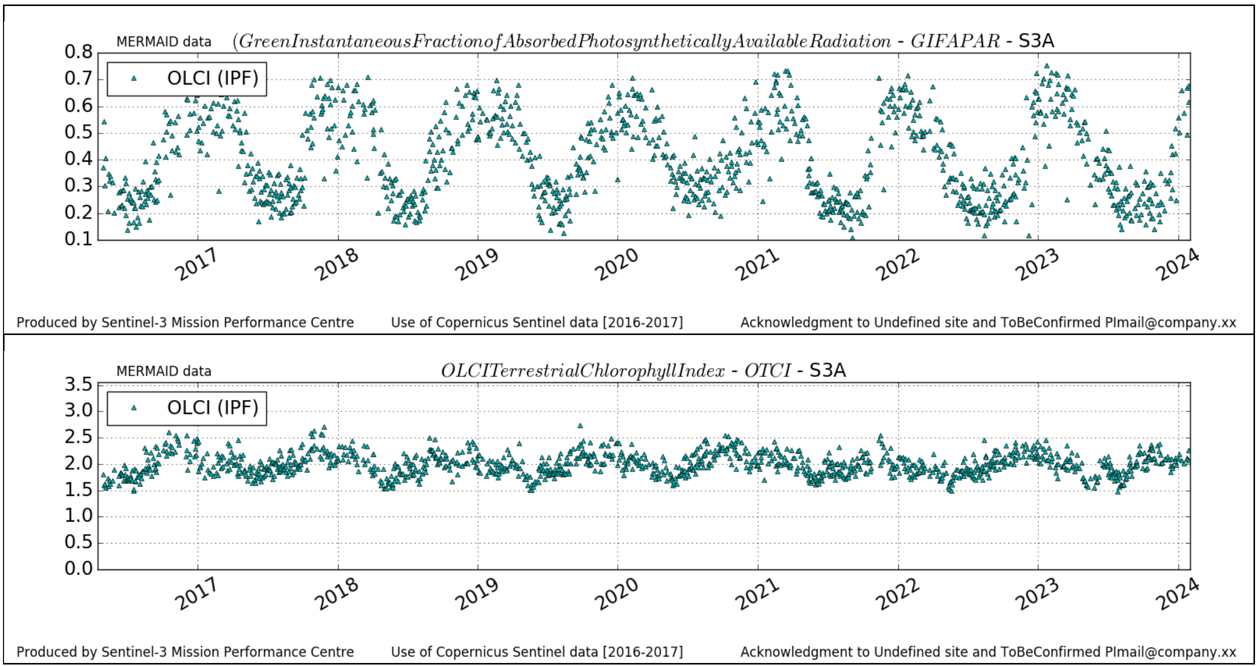

Figure 72: ITCat time series over current report period

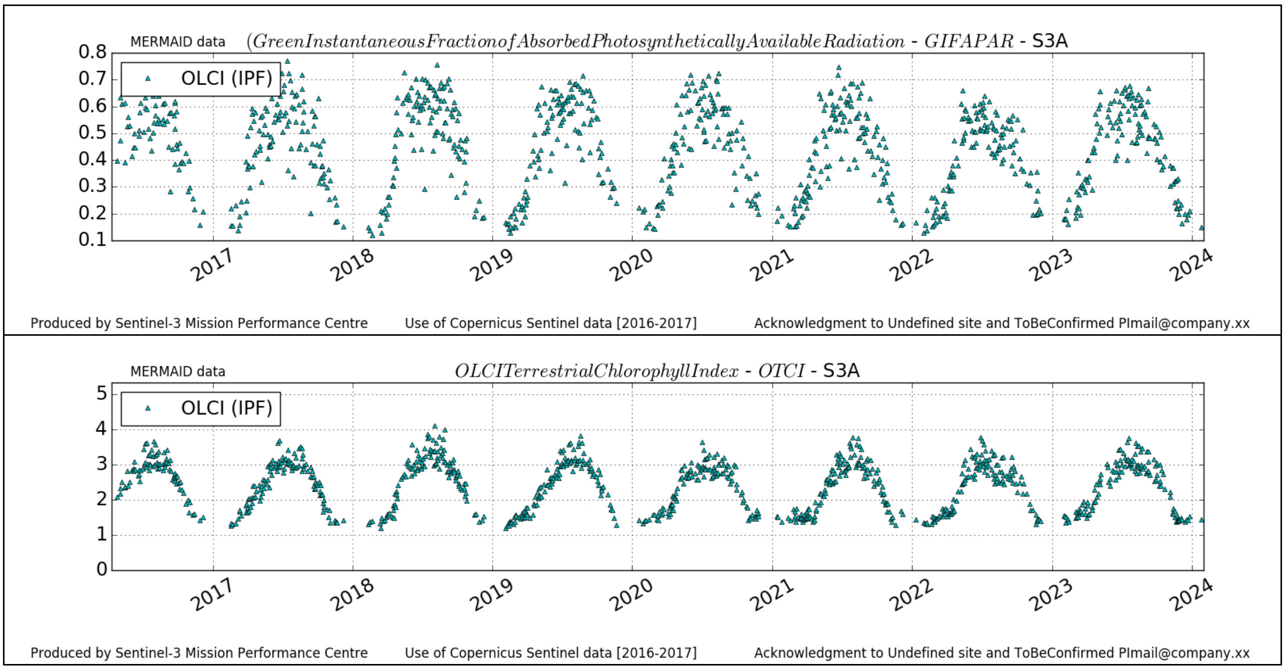

Figure 73: ITIsp time series over current report period

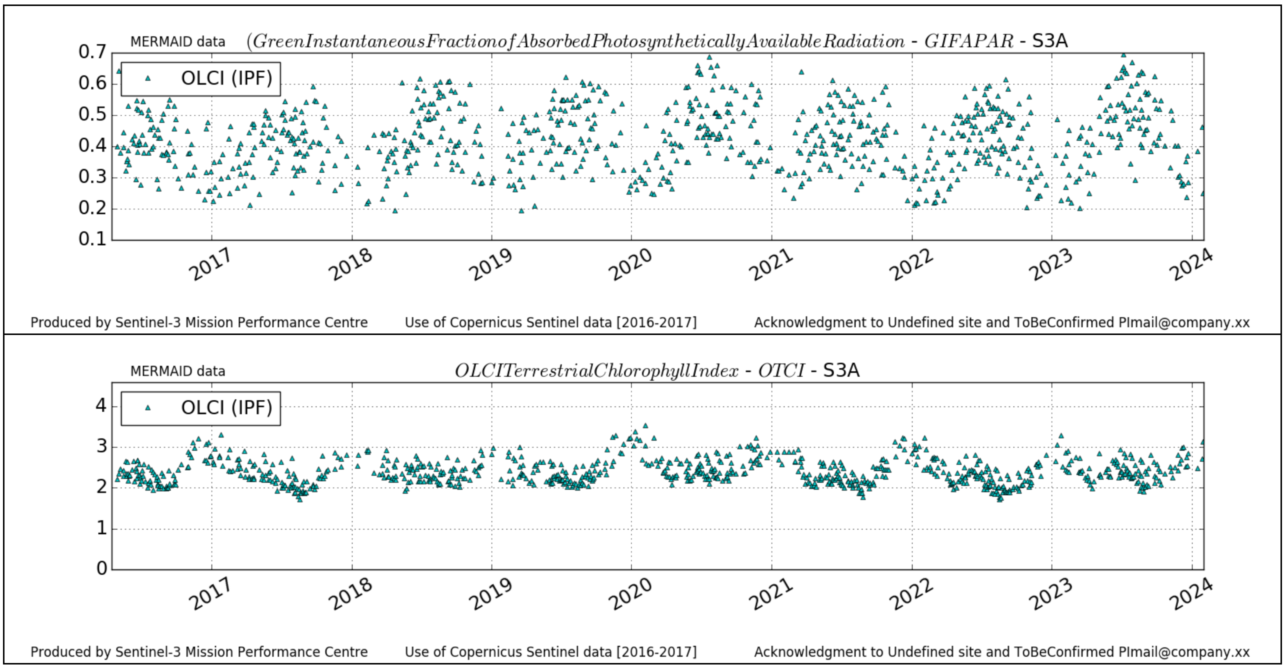

Figure 74: ITSro time series over current report period

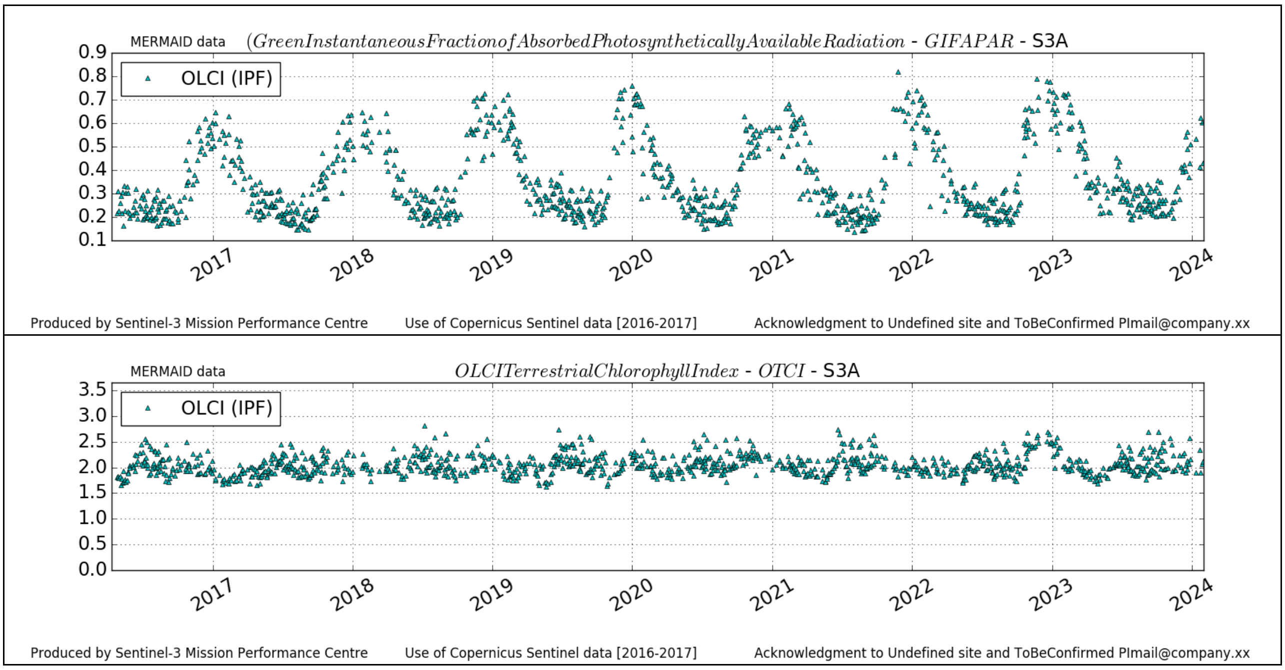

Figure 75: ITTra time series over current report period

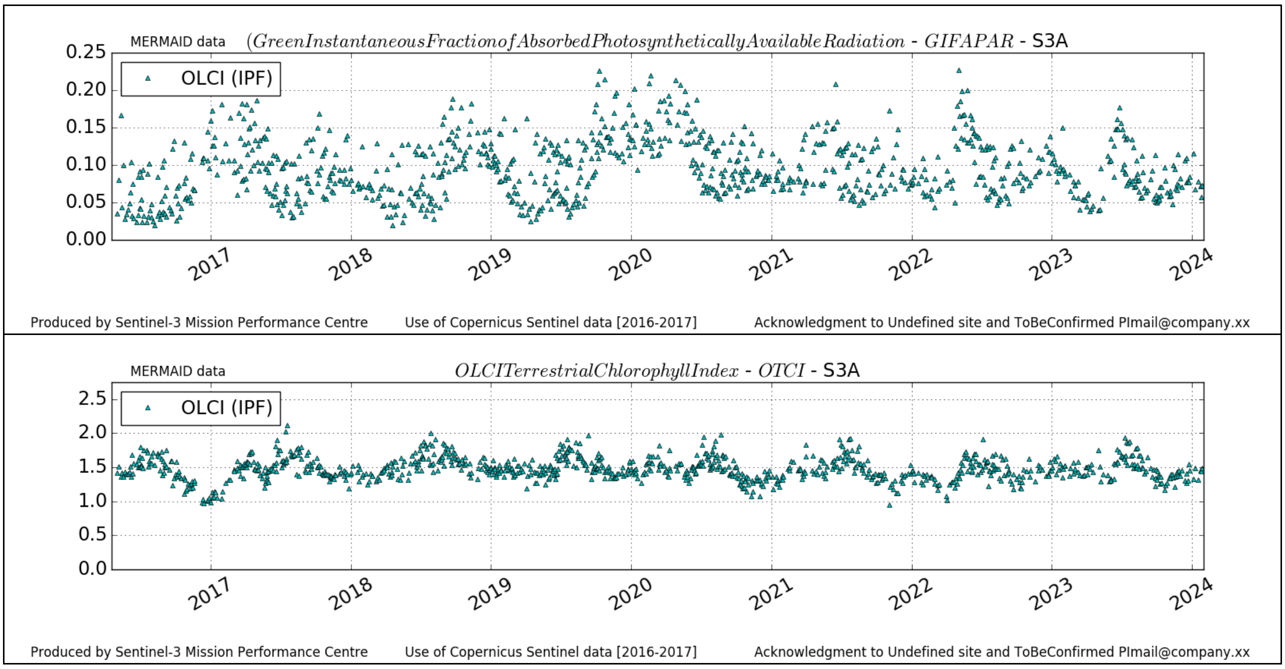

Figure 76: SPAli time series over current report period

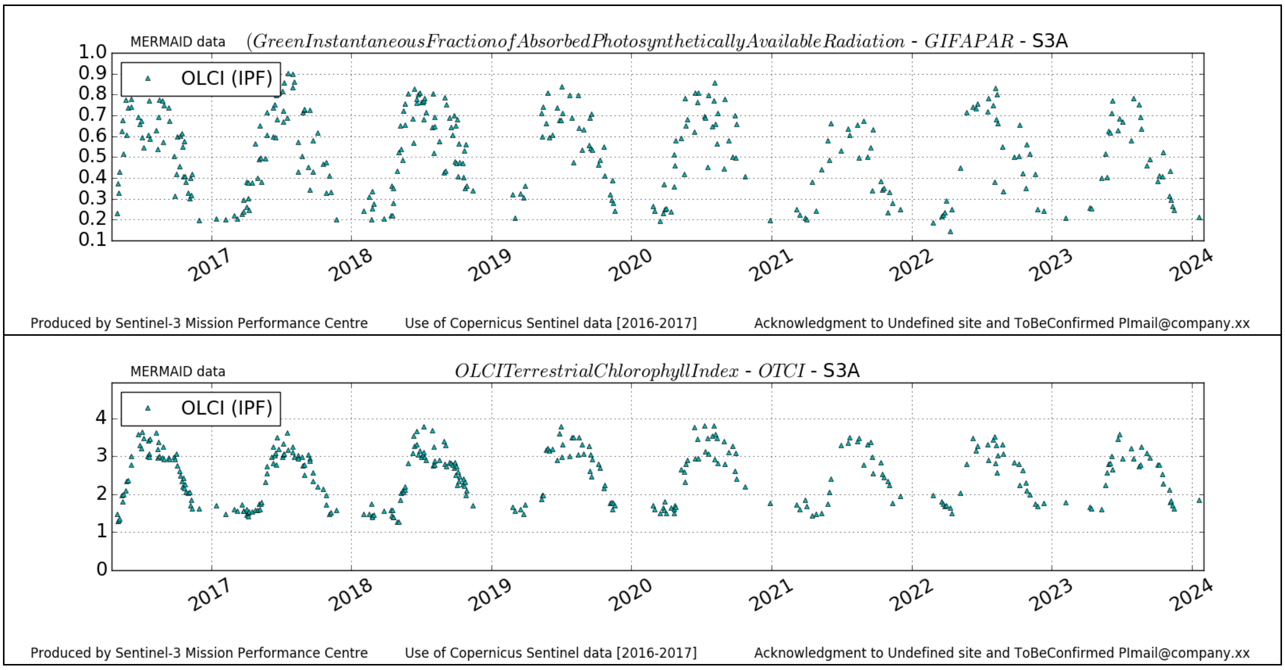

Figure 77: UKNFo time series over current report period

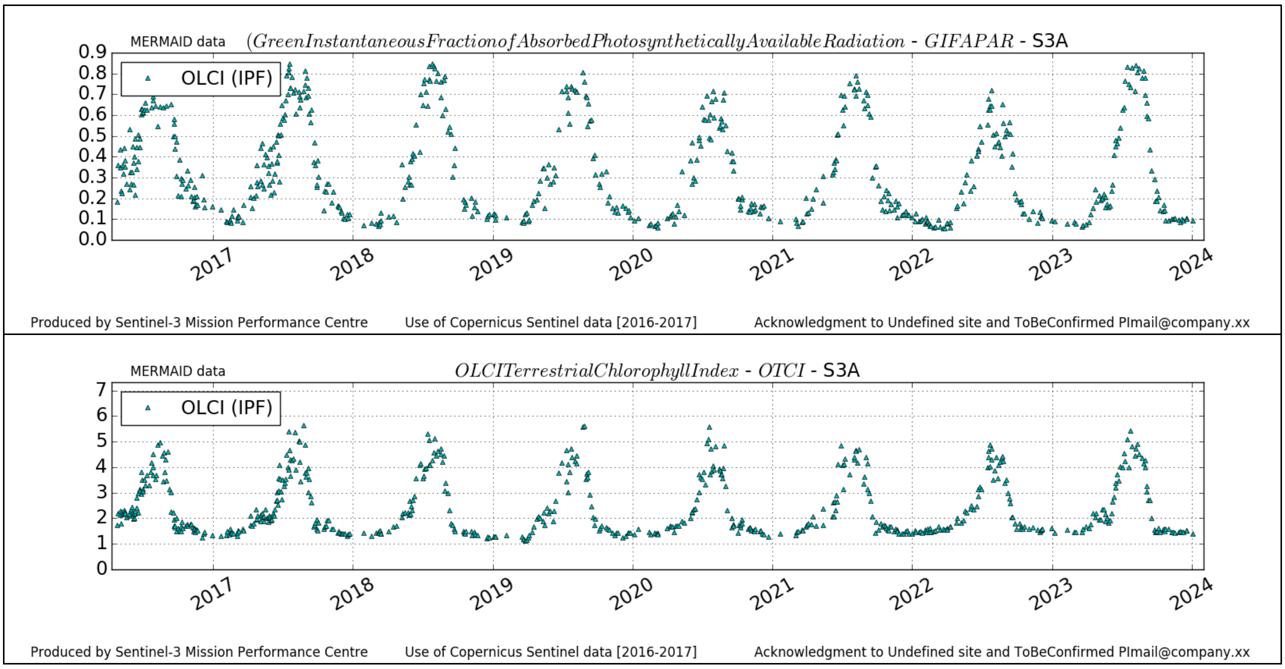

Figure 78: USNe1 time series over current report period

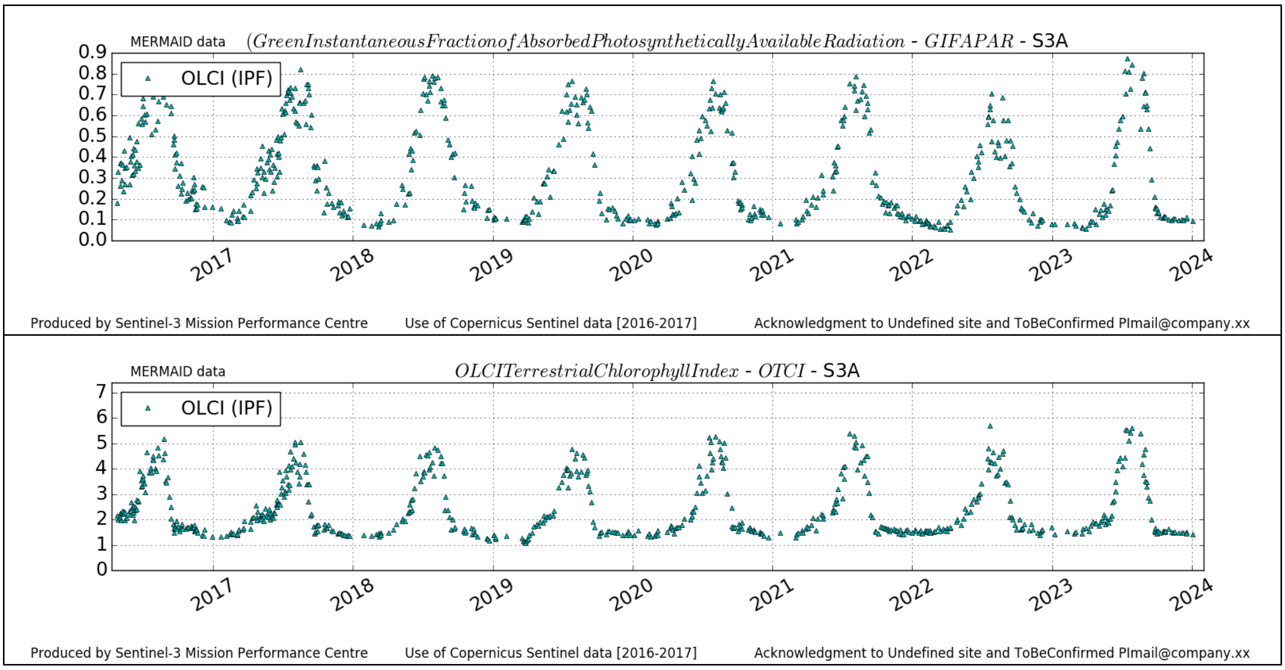

Figure 79: USNe2 time series over current report period

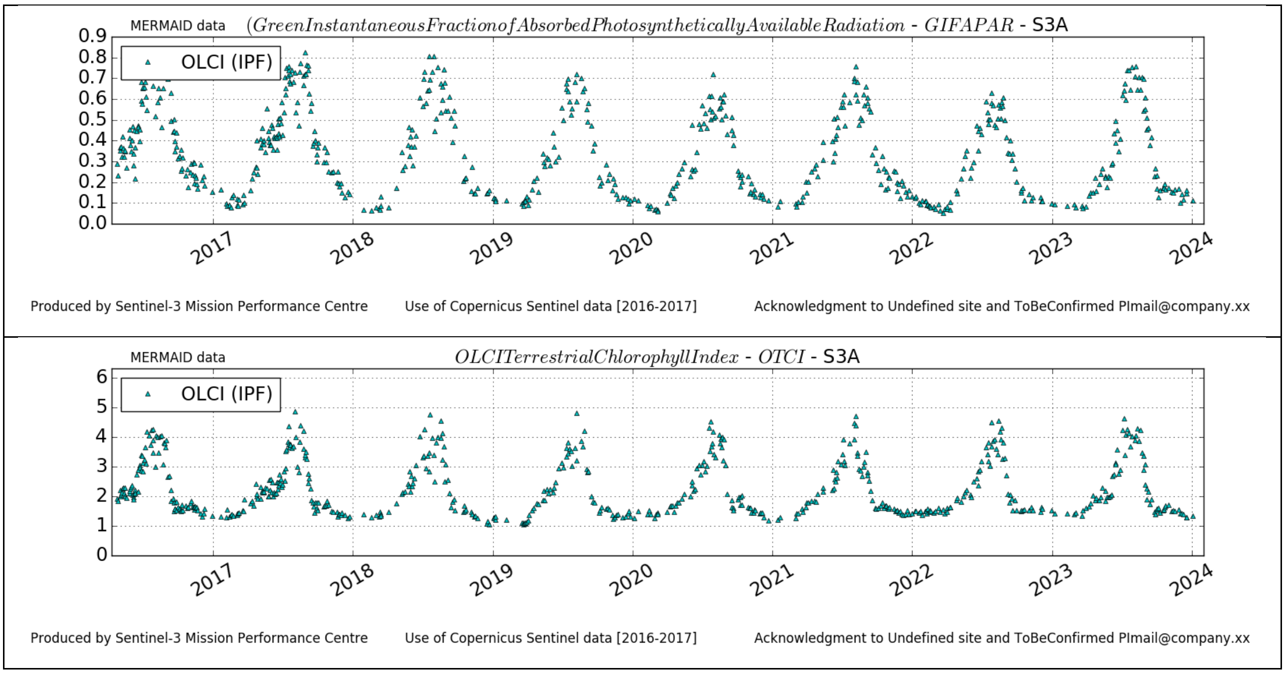

Figure 80: USNe3 time series over current report period

4.1.1.2 OLCI-B

Figure 81 to Figure 90 below present the Core Land Sites OLCI-B time series over the current period.

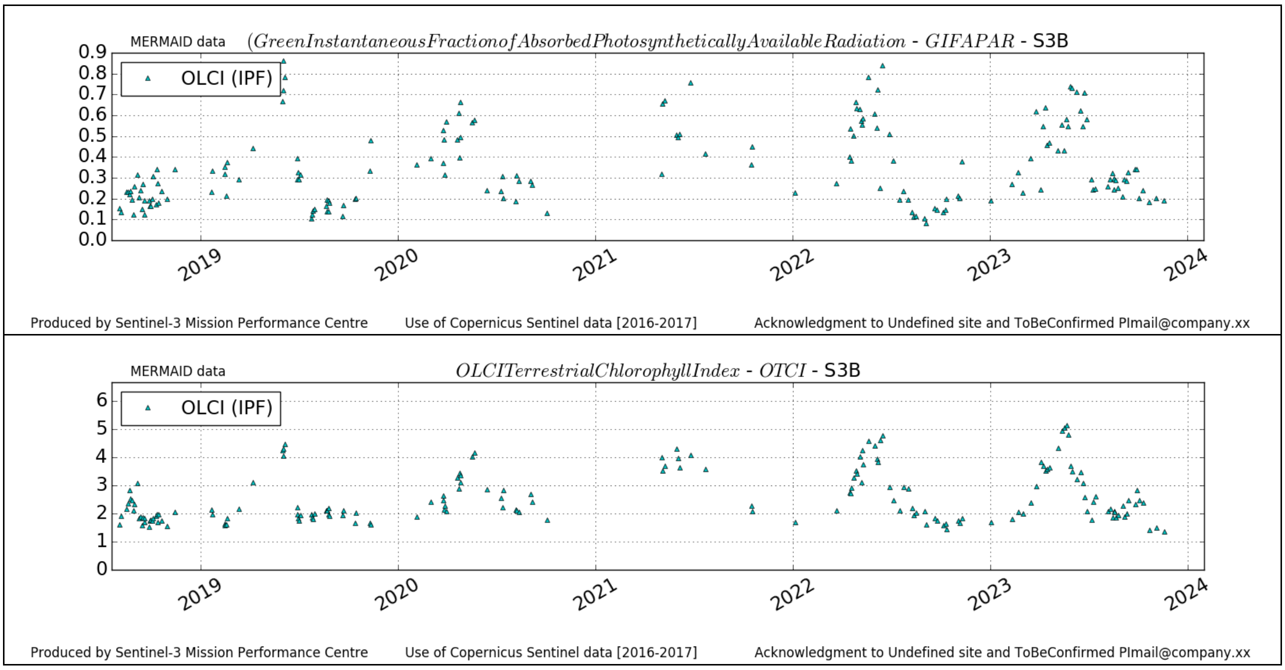

Figure 81: DeGeb time series over current report period

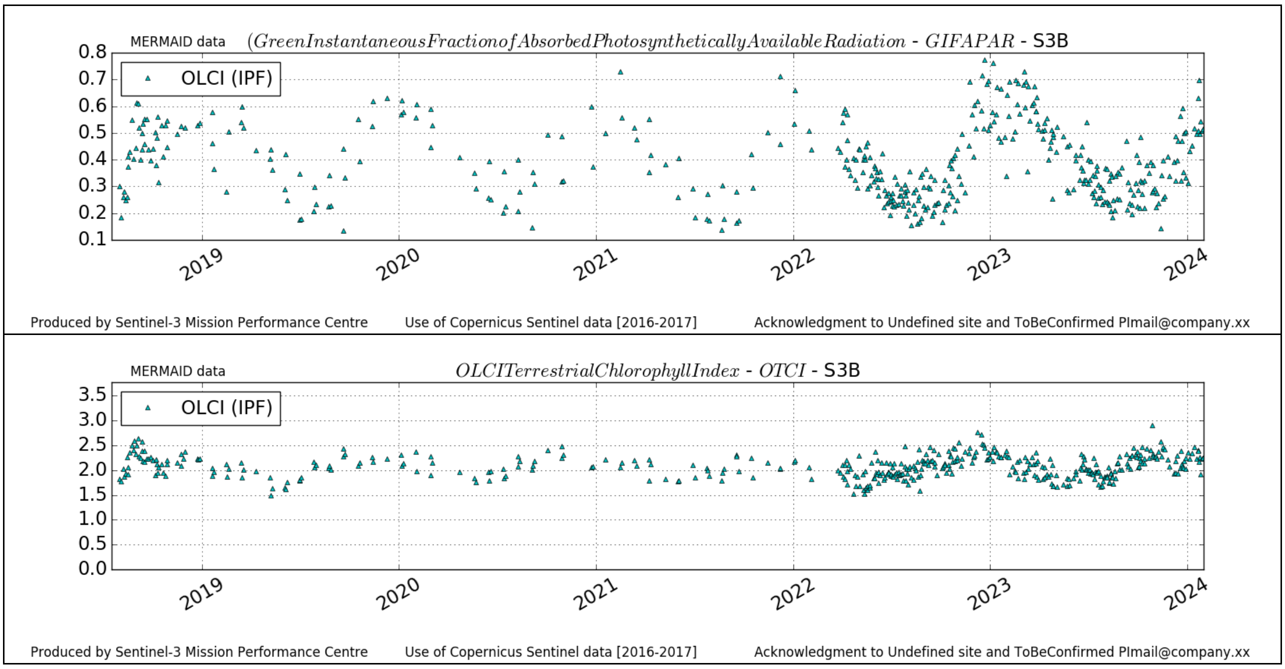

Figure 82: ITCat time series over current report period

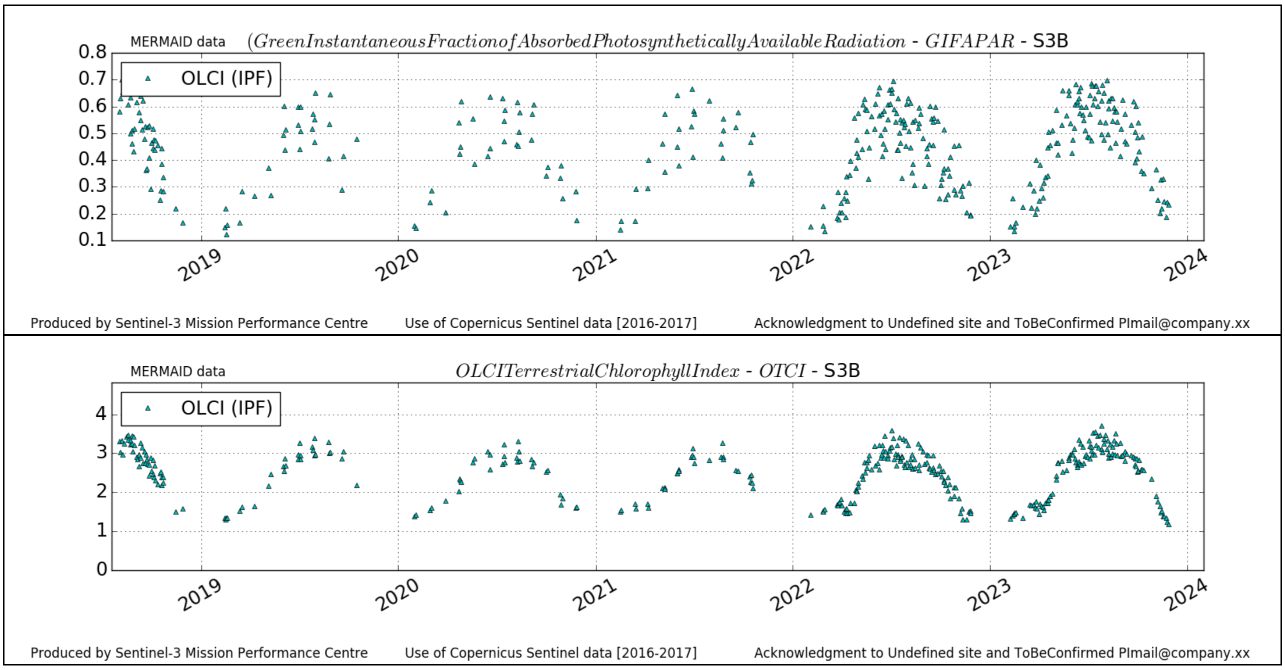

Figure 83: ITIsp time series over current report period

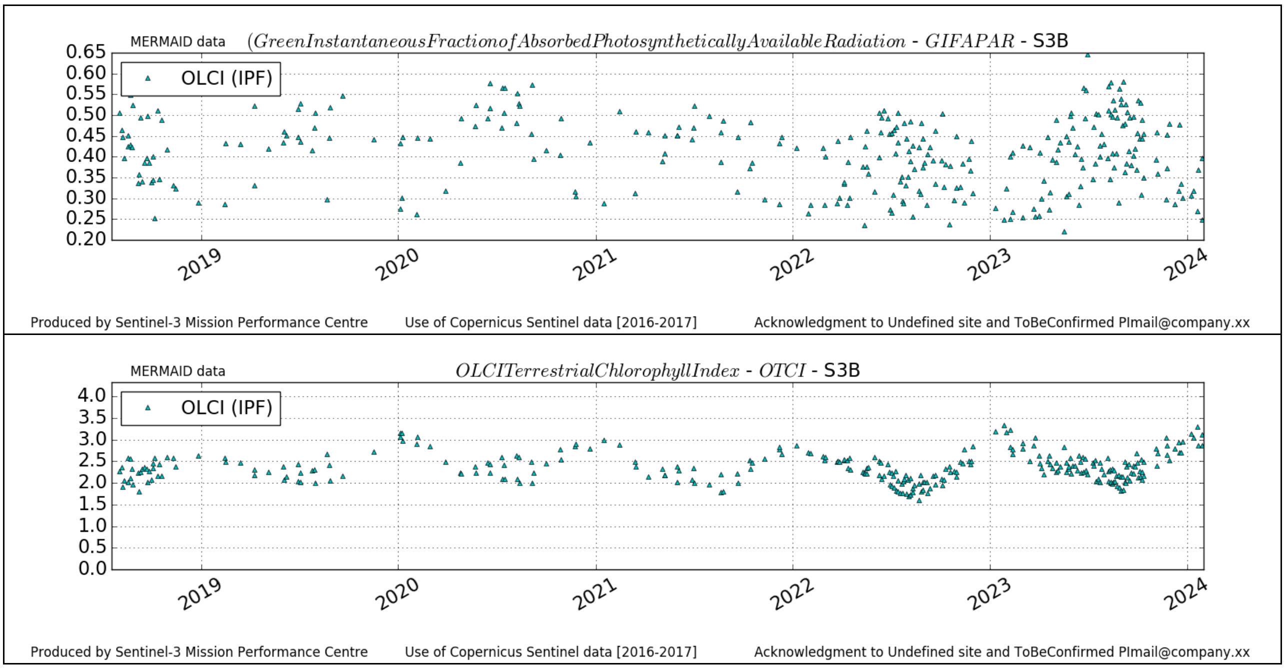

Figure 84: ITSro time series over current report period

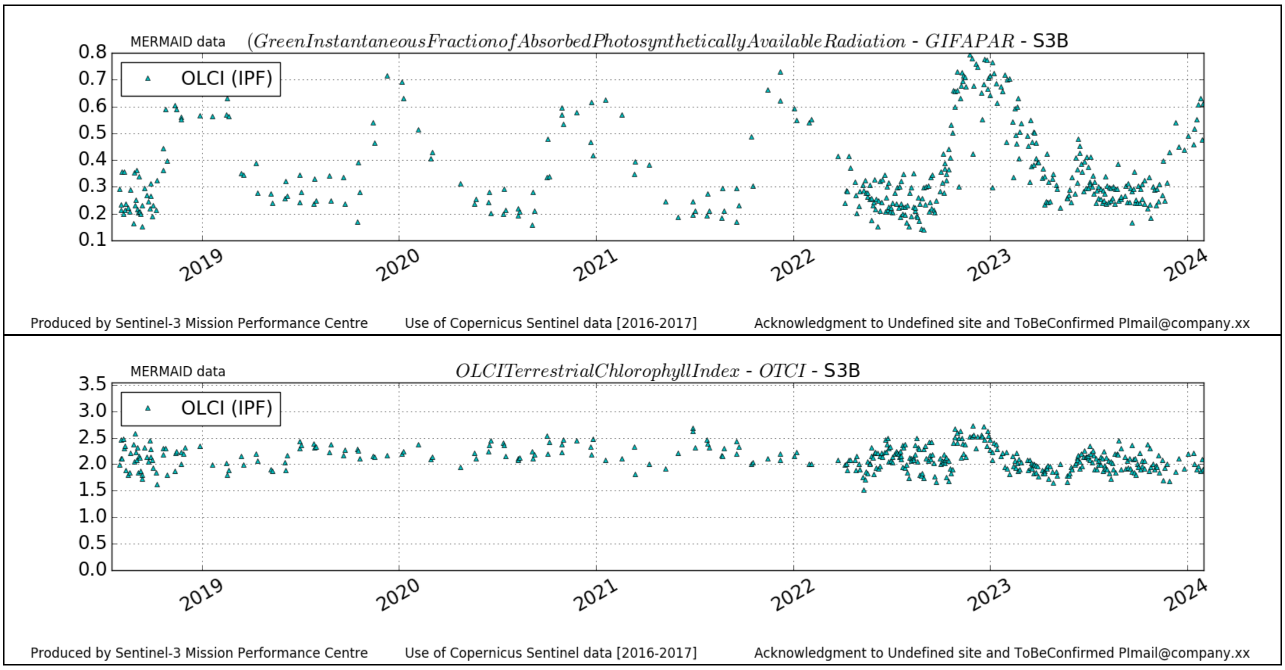

Figure 85: ITTra time series over current report period

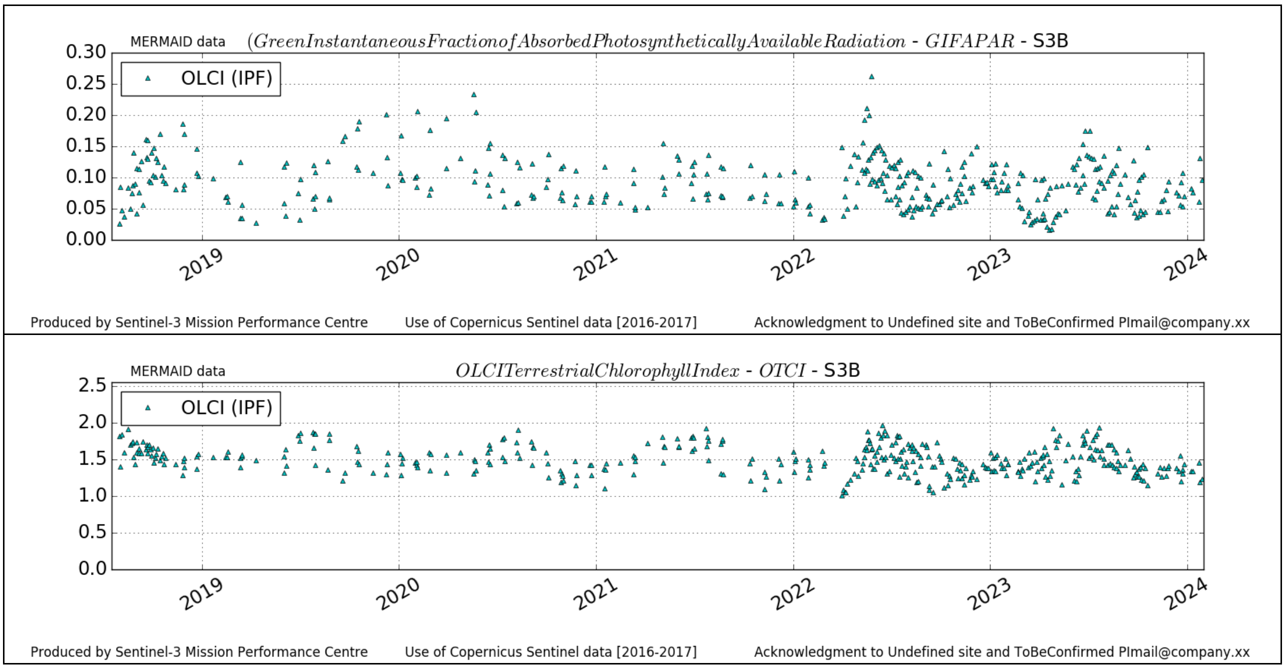

Figure 86: SPAli time series over current report period

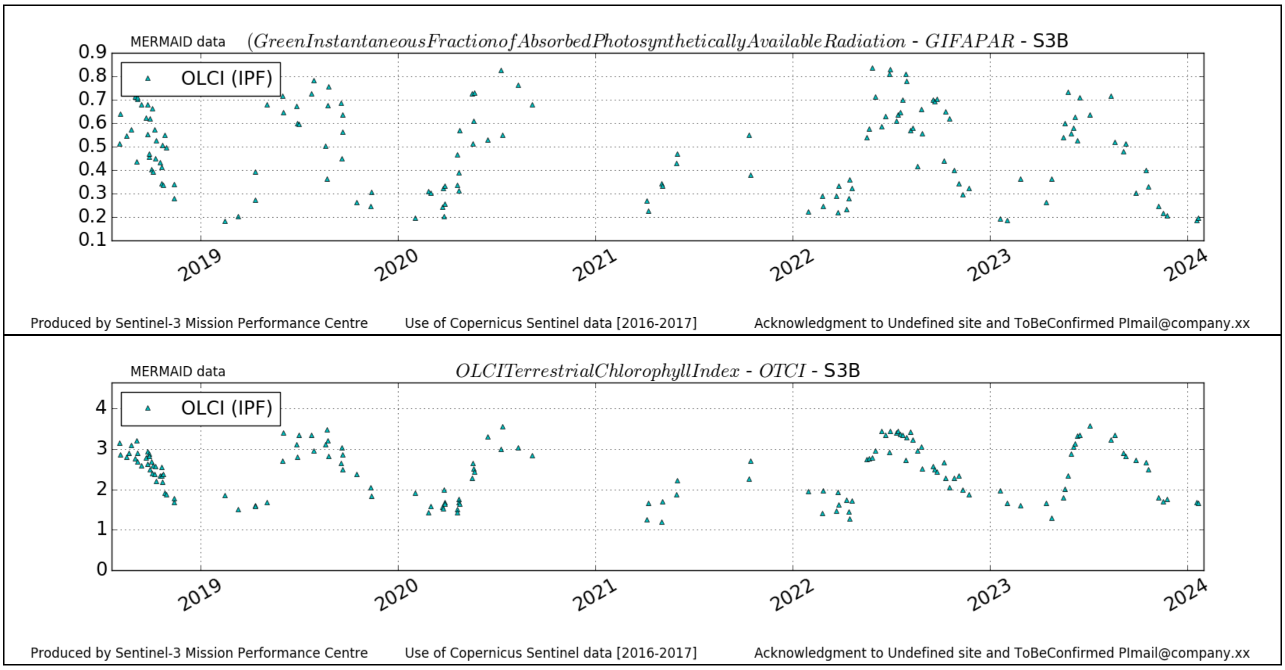

Figure 87: UKNFo time series over current report period

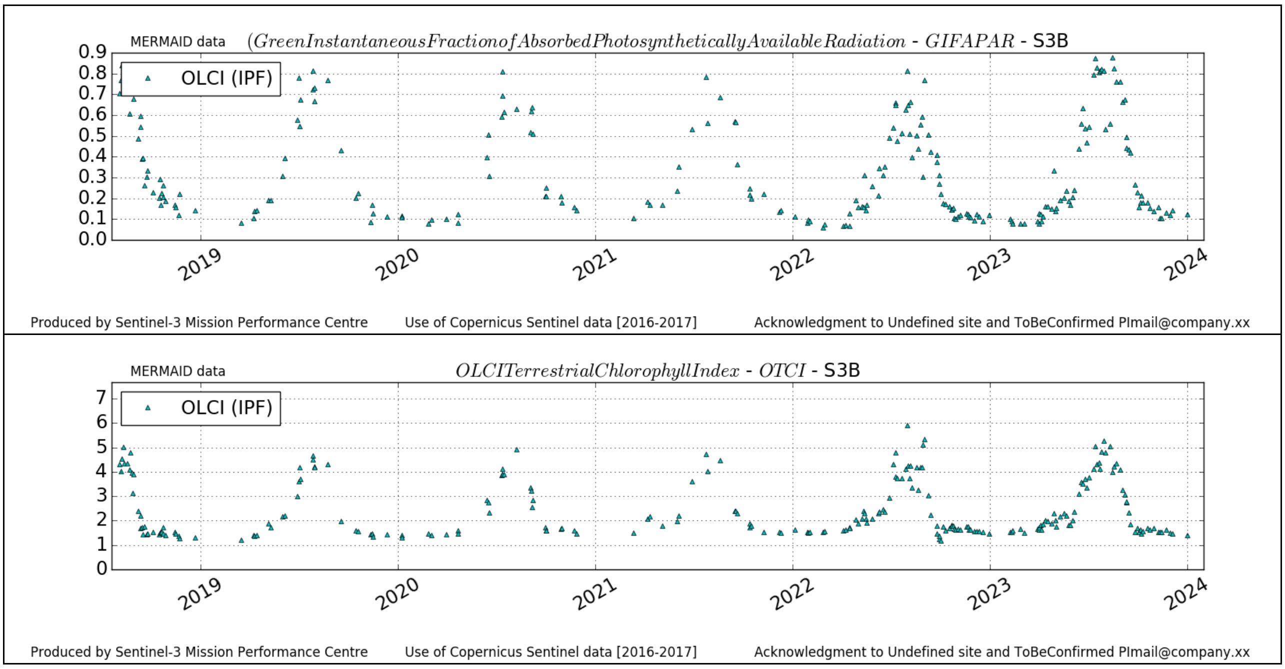

Figure 88: USNe1 time series over current report period

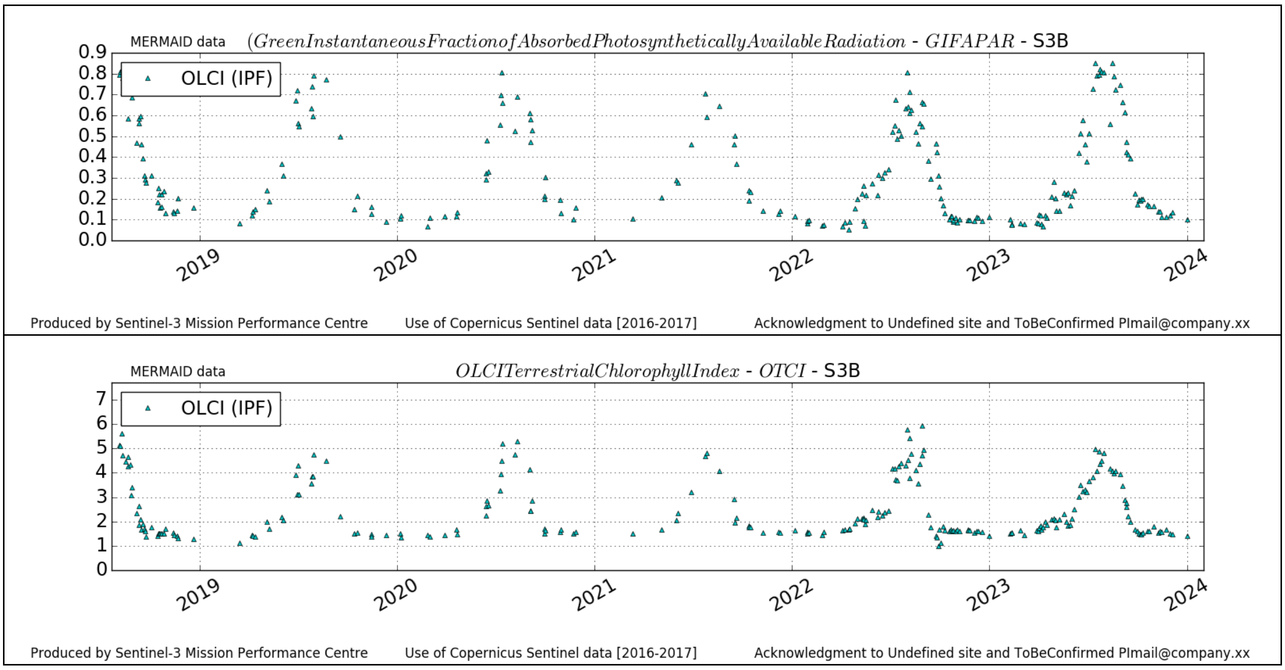

Figure 89: USNe2 time series over current report period

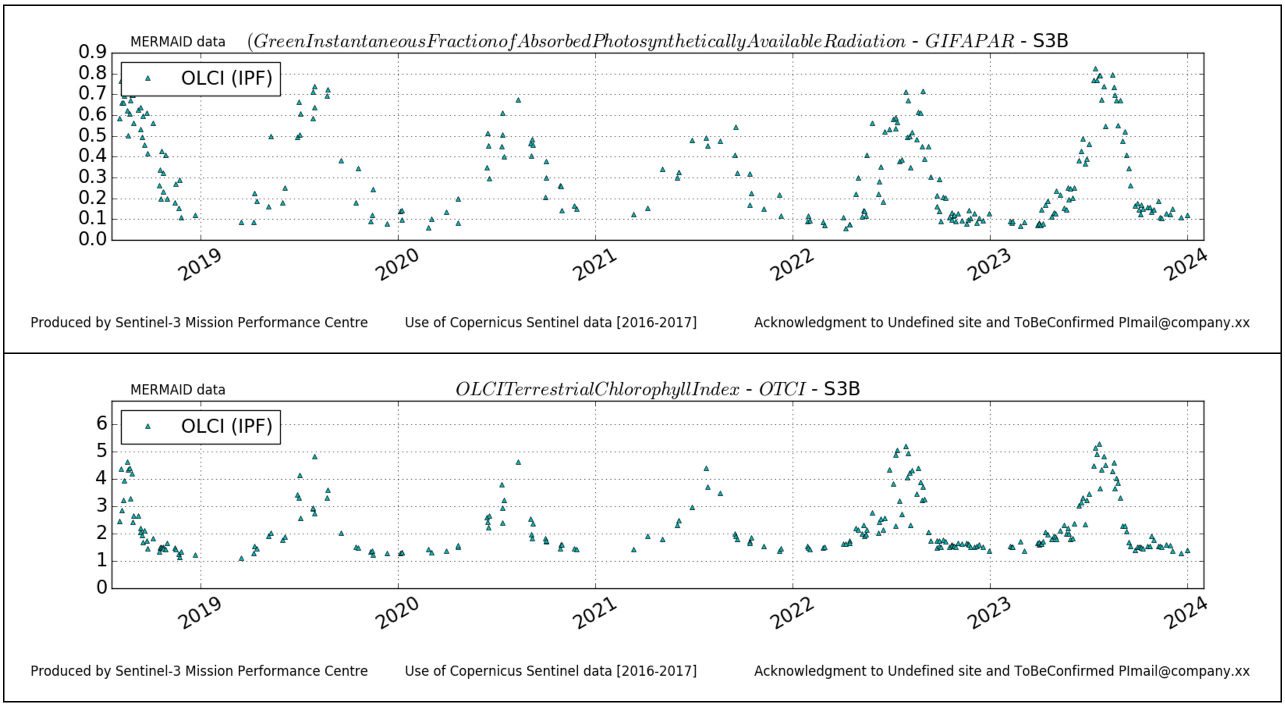

Figure 90: USNe3 time series over current report period

4.1.2 Comparison with MERIS MTCI Climatology

This section presents the comparison between MERIS and OLCI land products (GIFAPAR-*Green Instantaneous Fraction of Absorbed Photosynthetically Available Radiation*- and OTCI -*Terrestrial Chlorophyll Index* -) between 1st January 2023 and 30th January 2024, over a selection of sites from the S3VT (*Sentinel-3 Validation Team*), CEOS (*Committee for Earth Observation Satellites*) and GBOV (*Ground-Based Observations for Validation*) sites (Table 6). OTCI is compared against the L3 Envisat MERIS Terrestrial Chlorophyll Index (MTCI) composites at 1 km spatial resolution, sourced from the UK Centre for Environmental Data Analysis (CEDA). GIFAPAR is compared against MERIS FAPAR climatology (MGVI – MERIS fourth-processing over 2003-2011 at 1.2 km). The 15-day smoothed product from daily data is sourced by the Joint Research Centre (Gobron *et al.,* 2020).

Figure 91 shows seasonal trends and scatterplots of the monthly mean for the period 2002-2012 (grey), 2023 GIFAPAR (blue), and 2024 GIFAPAR (red) at specific sites for S3A and S3B. The profiles indicate a robust alignment between GIFAPAR seasonality and MGVI climatology (R^2>0.38; NRMS<0.22 for nearly all sites). Additionally, OTCI demonstrates strong concurrence with MTCI (Figure 92), R^2>0.34, NRMSD<0.2 for S3A and R^2>0.37, NRMSD<0.18 for S3B. This indicates its capacity to maintain continuity in the 10-year MERIS archive and provide confidence in its performance.

Table 6: S3VT, CEOS and GBOV validation sites analysed.

Name	Country	LAT	LON	IGBP
Sp-Ala	Spain	38.45	−1.06	Semi-arid Mediterranean
AUS-Alice Mulga	Australia	-22.28	133.25	Evergreen Needleleaf
FR-Aurade	France	43.54	1.10	Croplands
US-Bartlett	United States	44.06	-71.287	Mixed Forest
US-Blandy	United States	39.06	-78.07	Deciduous Broadleaf
CZ-Bily Kriz forest	Czechia	49.50	18.53	Evergreen Needleleaf
BE-Brasschaat	Belgium	51.30	4.51	Evergreen Needleleaf
AUS-Calperum Malle	Australia	-34.00	140.58	Shrubland
AUS-Cape Tribulation	Australia	-16.10	145.37	Evergreen Needleleaf
It-Castelporziano	Italy	41.70	12.35	Mixed Forest
It-Cat	Italy	37.27	14.88	Croplands (Orange)
US-Central Plains	United States	40.815	-104.74	Grasslands
IT-CollelongoITALY	Italy	41.84	13.58	Deciduous Broadleaf broadleaved, deciduous, closed
AUS-Cumberland Plain	Australia	-33.61	150.72	Evergreen Broadleaf
US-Dead Lake	United States	32.54172	-87.8039	Mixed Forest
US-Disney	United States	28.12504	-81.4363	Shrublands
FR-Estrees	France	49.87	3.02	Croplands
De-Geb	Germany	51.10	10.91	Croplands
US-Guanica	United States	17.96	-66.868	Mixed Forest
AUS-Great Western	Australia	-30.19	120.65	Shrublands
GE-Hainich	Germany	51.07	10.45	Mixed Forest
US-Harvard	United States	42.53	-72.17	Mixed Forest
FR-Hesse	France	48.67	7.06	Deciduous Broadleaf
DE-Hones Holtz	Germany	52.08	11.22	Deciduous Broadleaf
It-Isp	Italy	45.81	8.63	Mixed Forest
US-Jones	United States	31.19	-84.46	Evergreen Needleleaf
US-Jornada	United States	32.59	-106.84	Open shrubland
US-Konza	United States	39.11	-96.61	Croplands
US-Lajas	United States	18.02	-67.07	Grasslands
IT-Lison	Italy	45.74	12.75	Croplands
AUS-Litchfield	Australia	-13.18	130.79	Evergreen Broadleaf
NE-Loobos	Netherlands	52.16	5.74	Evergreen Needleleaf
US-Moab	United States	38.24	-109.38	Shrublands
FR-Montiers	France	48.53	5.31	Deciduous Broadleaf
US-Mountain Lake	United States	37.37	-80.52	Deciduous Broadleaf
US-Niwot	United States	40.05	-105.58	Evergreen Needleleaf
US-Oak	United States	35.96	-84.28	Mixed Forest
US-Onaqui	United States	40.17	-112.45	Shurblands
US-Ordway	United States	29.68	-81.9934	Evergreen Needleleaf
FR-Puechabon	France	43.74	3.59	Evergreen Needleleaf
AUS-Robson Creek	Australia	-17.11	145.63	Mixed Forest
AUS-Rushworth	Australia	-36.75	144.96	Deciduous Broadleaf
DE-Selhausen	Germany	50.86	6.44	Cropland
US-Smithsonian Conservation Biology (SCBI)	United States	38.89	-78.13	*Mixed Forest*
US-Smithsonian Environmental (SERC)	United States	38.89	-76.56	*Croplands*
US-Steigerwaldt	United States	45.50	-89.58	*Deciduous Broadleaf*
It-Sro	Italy	43.72	10.28	*Pinus Pinea*
US-Talladega	United States	32.95	-87.39	Evergreen Needleleaf
DE-Tharandt	Germany	50.96	13.56	Evergreen Needleleaf
It-Tra	Italy	37.64	12.85	Croplands (Vineyards and olive trees)
AUS-Tumbarumba	Australia	-35.65	148.15	Evergreen Broadleaf
USNe1	United States	41.165	-96.47	Croplands
USNe2	United States	41.16	-96.47	Croplands
USNe3	United States	41.17	-96.43	Croplands
Sp- Valencia	Spain	39.57	-1.28	Croplands
BE-Vielsalm	Belgium	50.30	5.99	Evergreen Needleleaf
AUS-Warra Tall	Australia	-43.09	146.65	Evergreen Broadleaf
AUS-Watts Creek	Australia	-37.68	145.68	Evergreen Broadleaf
US-Woodworth	United States	47.12	-99.24	Grasslands
AUS-Wombat	Australia	-37.42	144.09	Evergreen Broadleaf
AUS-Zig zag	Australia	-37.47	148.33	Evergreen Broadleaf

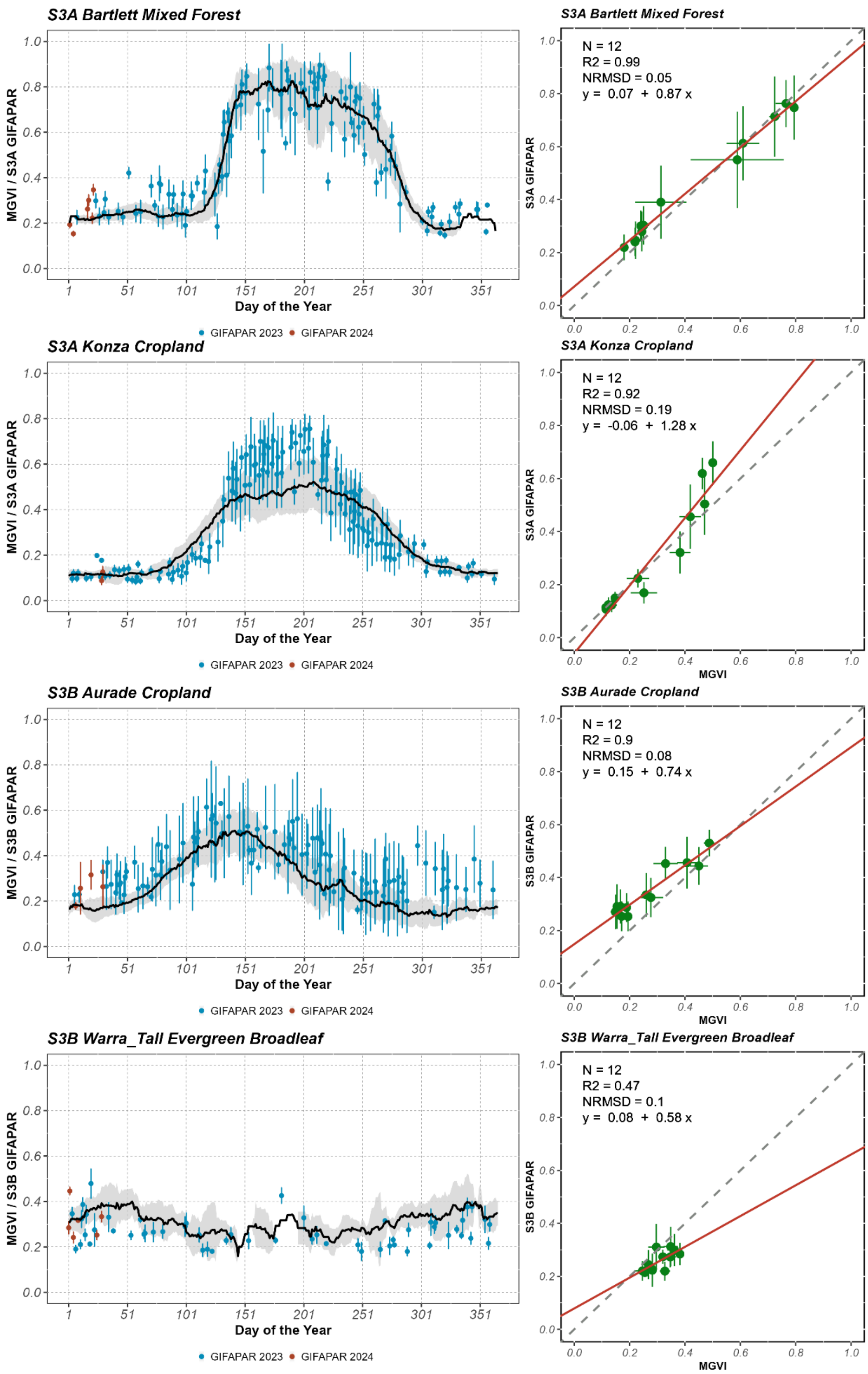

Figure 91: Time series (left) of GIFAPAR and MGVI and a corresponding scatterplot of the monthly mean for site Barlett and Konza (representing S3A) and Aurade and Warra Tall (representing S3B). The climatology of MERIS FAPAR (black and grey colours) is compared against 2023 (blue colours) and 2024(red colours).

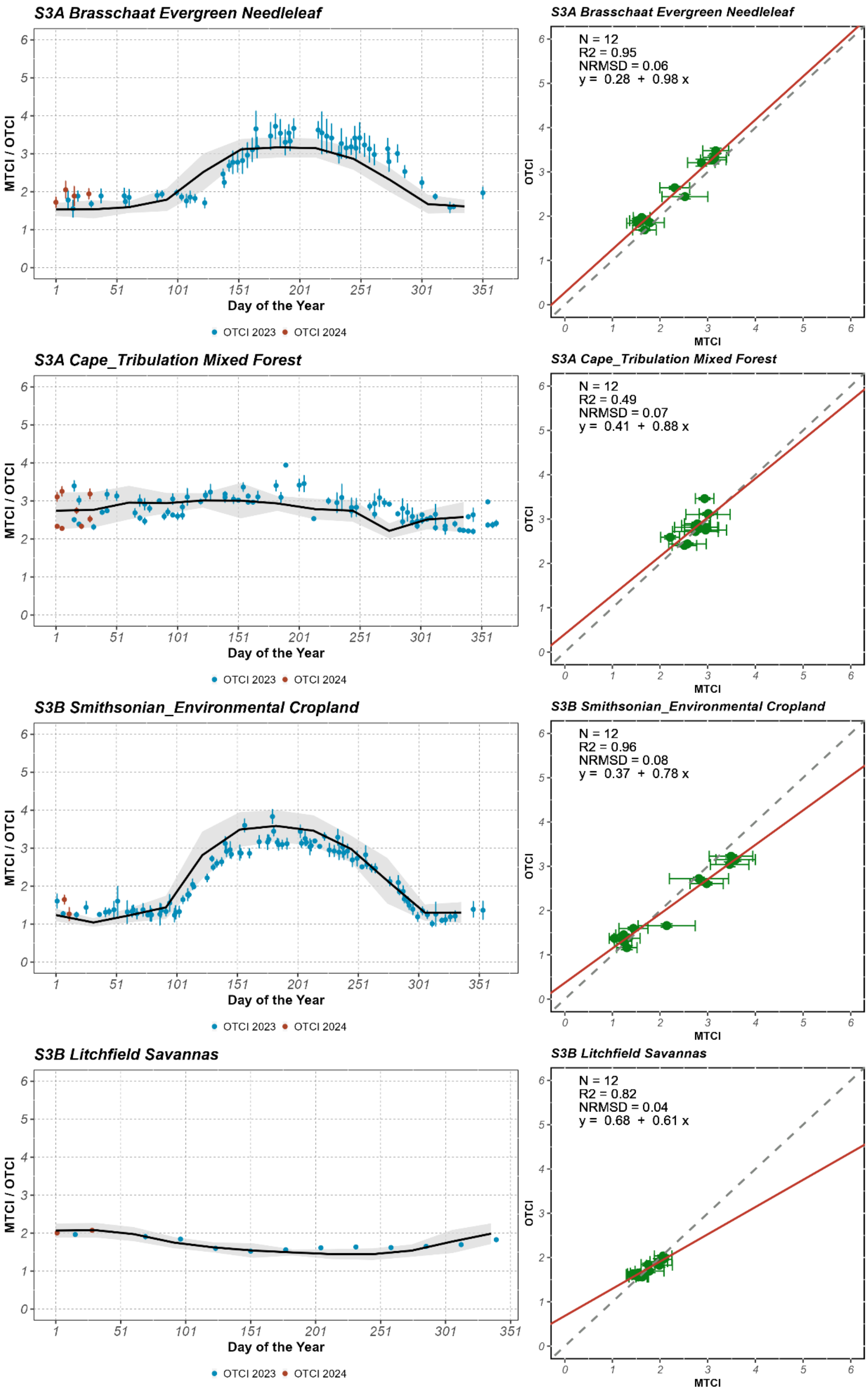

Figure 92: Time series (left) of OTCI and MTCI and a corresponding scatterplot of the monthly mean for sites Brasschaat and Cape Tribulation (representing S3A), and Smithsonian Environmental and Litchfield (representing S3B). The climatology of MERIS MTCI (black and grey colours) is compared against 2023 (blue colours) and 2024 (red colours).

4.1.3 Comparison with GBOV (Ground-Based Observations for Validation) data v3

There have been no new results during the reporting period. The latter figures (reported in the OLCI Data Quality Report covering August 2023) are considered valid.

4.1.4 Sentinel-3A and 3B biophysical variables inter-annual variability results

There have been no new results during the reporting period. The latter figures (reported in the OLCI Data Quality Report covering September 2023) are considered valid.

4.2 [OLCI-L2LRF-CV-410 & OLCI-L2LRF-CV-420] – Cloud Masking & Surface Classification for Land Products

There have been no new results during the reporting period. The latter figures (reported in OLCI Data Quality Report covering October 2023) are considered valid.

5 Validation of Integrated Water Vapour over Land & Water

We continuously investigate the temporal evolution of quality measures of integrated water vapour, when comparing SUOMI NET (Ware et al. 2000) with reduced resolution data of OLCI L2 non-time-critical. All data until March 2022 has been acquired from EUMETSAT CODA, all data from Apr 2022 on has been downloaded from EUMETSAT's datastore (collection id: EO:EUM:DAT:0410). No significant changes since last reporting have been detected. 43297 (OLCI-A) and 27766 (OLCI-B) valid matchups within the period of June 2016 (OLCI-A) January 2019 (OLCI-B) to end of January 2024 have been analysed.

For the cloud detection, the standard L2 cloud-mask has been applied (including the cloud ambiguous and cloud margin flags). The comparison of OLCI and GNSS shows a very high agreement (Figure 93). The correlation between both quantities is around 0.98. The root-mean-squared-difference is 1.9 -2.1 kg/m^2. The systematic overestimation by OLCI is 11%-12%. The bias corrected *rmsd* is around 1.3-1.4 kg/m^2.

The temporal evolution of several quality measures (Figure 94), indicates small seasonal variations, which are certainly related to retrieval assumptions.

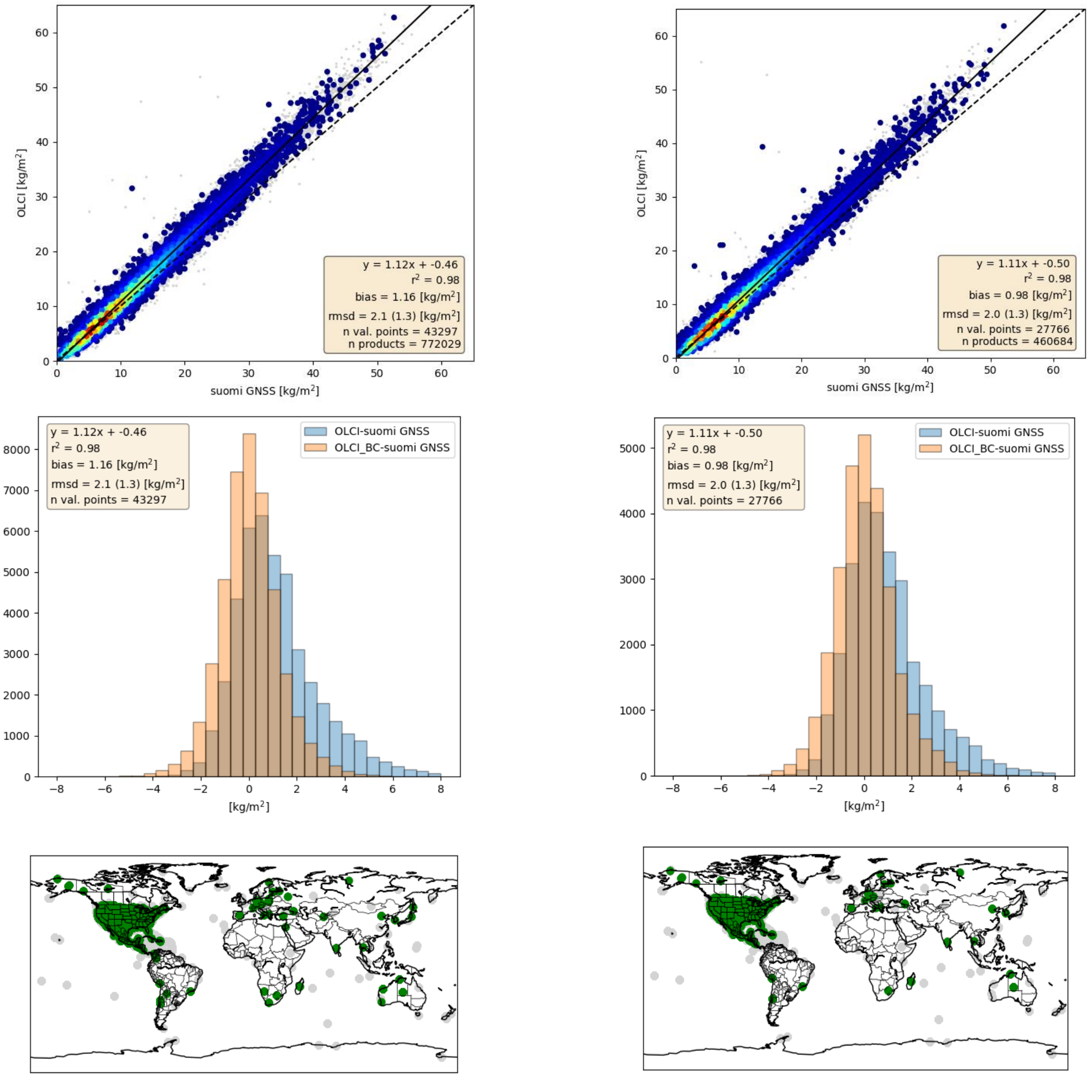

Figure 93: Upper: Scatter plot of the IWV products, derived from OLCI (A left, B right) above land and from SUOMI NET GNSS measurements. Middle: Histogram of the difference between OLCI (A: left, B: right) and GNSS (blue: original OLCI, orange: bias corrected OLCI). Lower: Positions of the GNSS (A: left, B: right).

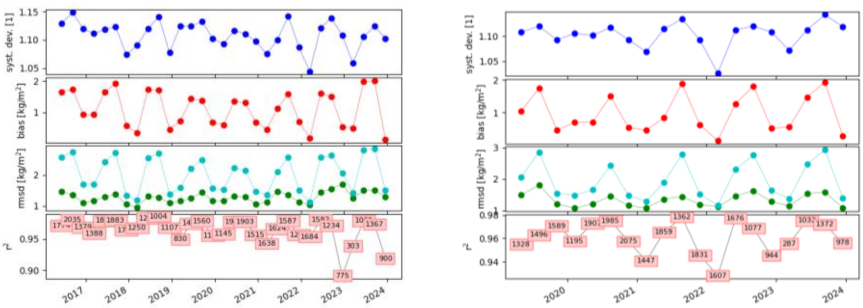

Figure 94: Temporal evolution of different quality measures for OLCI A (left) and OLCI B (right) with respect to SUOMI Net. From top to bottom: systematic deviation factor, bias, root mean squared difference (with and without bias correction), explained variance (number in boxes are the numbers of matchups)

6 Level 2 SYN products validation

6.1 SYN L2 SDR products

There have been no new results during the reporting period. The latter figures (reported in OLCI Data Quality Report covering December 2023) are considered valid.

6.2 SY_2_VGP, SY_2_VG1 and SY_2_V10 products

The similarity of SYN VGT like products with the PROBA-V archive is evaluated through intercomparison of 10-daily composites extractions over LANDVAL [1] sites. Since there is no overlap with the PROBA-V nominal operational phase and no PROBA-V Collection 2 climatology is available yet, direct comparison is done by comparing the SY_2_V10 NTC products starting January/2021 with PROBA-V S10-TOC products since January/2017.

The temporal evolution of statistics results below are based on intercomparison over the entire periods up to January/2024. The scatterplots are based on intercomparison between SY_2_V10 products of January/2024 with PROBA-V Collection 2 S10-TOC products of January/2020.

Products availability

Availability of SY_2_VG1 and SY_2_V10 products is checked through an automated query and download via the Copernicus Data Space Ecosystem feeding the products database of the Belgian Collaborative Ground Segment (Terrascope, www.terrascope.be). For the month January/2024, there are no missing data or empty files.

Statistical consistency

The scatter density plots with geometric mean regression equation, coefficient of determination (R^2) and APU statistics based on intercomparison between SY_2_V10 products of January/2024 with PROBA-V Collection 2 products of January/2020 are shown in Figure 95. The APU statistics are defined as: Accuracy (A) or average bias, Precision (P) or the standard deviation of the bias, and Uncertainty (U) or the Root Mean Squared Distance. Accuracy is best for BLUE (< 1%) and slightly less good for the other bands (up to 2%). The relatively large values for Precision (large scatter, low R^2) are caused by the fact that acquisitions of two different years are compared.

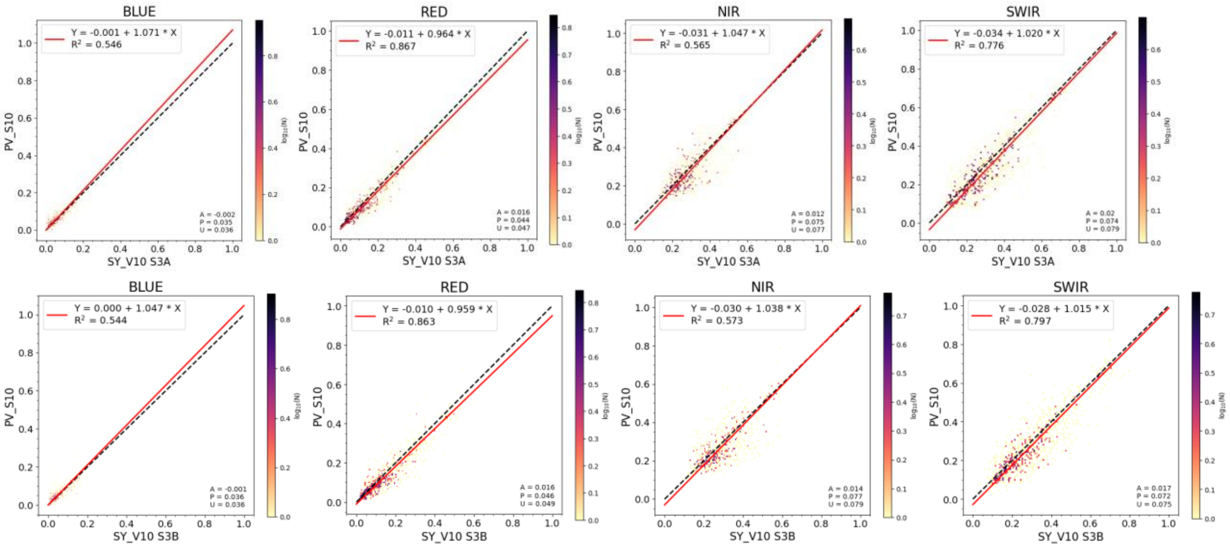

Figure 95: Scatter density plots between SY_V10 S3A (top) or S3B (bottom) and PROBA-V C2 S10-TOC for BLUE, RED, NIR and SWIR bands (left to right), January/2024 vs. January/2020

Temporal consistency

The temporal evolution of APU statistics derived from intercomparison of SY_2_V10 NTC products January/2021 – January/2024 with those of PROBA-V S10-TOC January/2017 – January/2020 (Figure 96). The APU statistics show stable evolution over time, although some seasonal pattern is observed for the mainly the SWIR channel, and to a lesser extent the RED and NIR channel. The temporal behaviour is stable, except for a strong discontinuity for the SWIR band, with improved statistics at the end of July/2023. From 18/07/2023 (for S3B) and 25/07/2023 (for S3A) an updated processing baseline is in operations, including application of SLSTR calibration factors, and aligning the spectral resampling to PROBA-V. As a result, the statistical consistency for RED, NIR and SWIR has improved in comparison to previous periods, which were affected by erroneous spectral resampling and the SLSTR calibration offset (in bands S5 and S6).

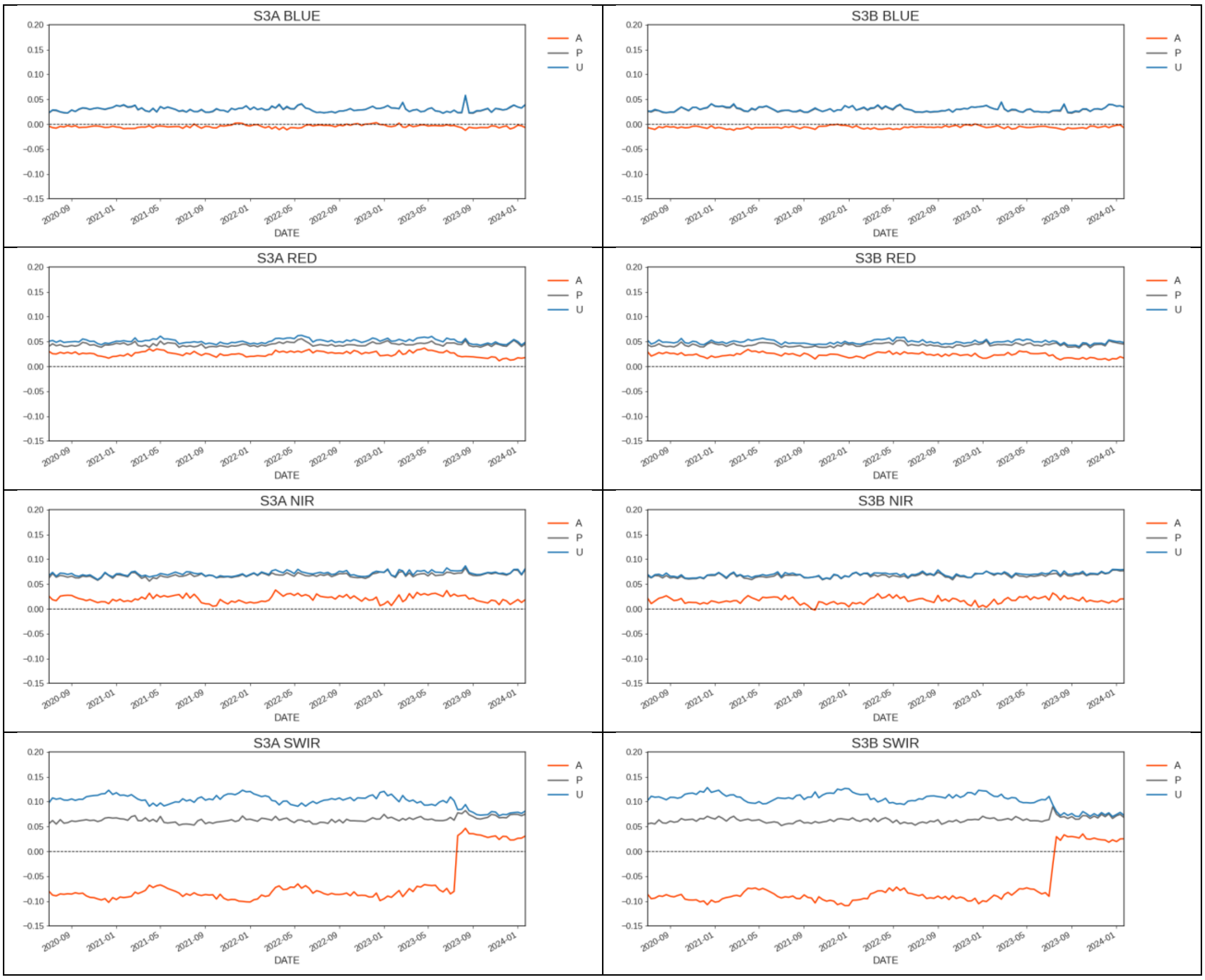

Figure 96: Temporal evolution of APU statistics between SY_2_V10 S3A (left) or S3B (right) and PROBA-V S10-TOC for BLUE, RED, NIR and SWIR bands (top to bottom), January/2021 – January/2024 (S3 SYN VGT) vs. January/2017 – January/2020 (PROBA-V)

Figure 97 shows the temporal evolution of APU statistics derived from the intercomparison of SY_2_V10 NTC products based on S3A with those based on S3B January/2021 – January/2024. The APU statistics show a stable temporal evolution, except for a strong discontinuity for SWIR, related to the different timing of the processing baseline update for S3A resp. S3B (see above).

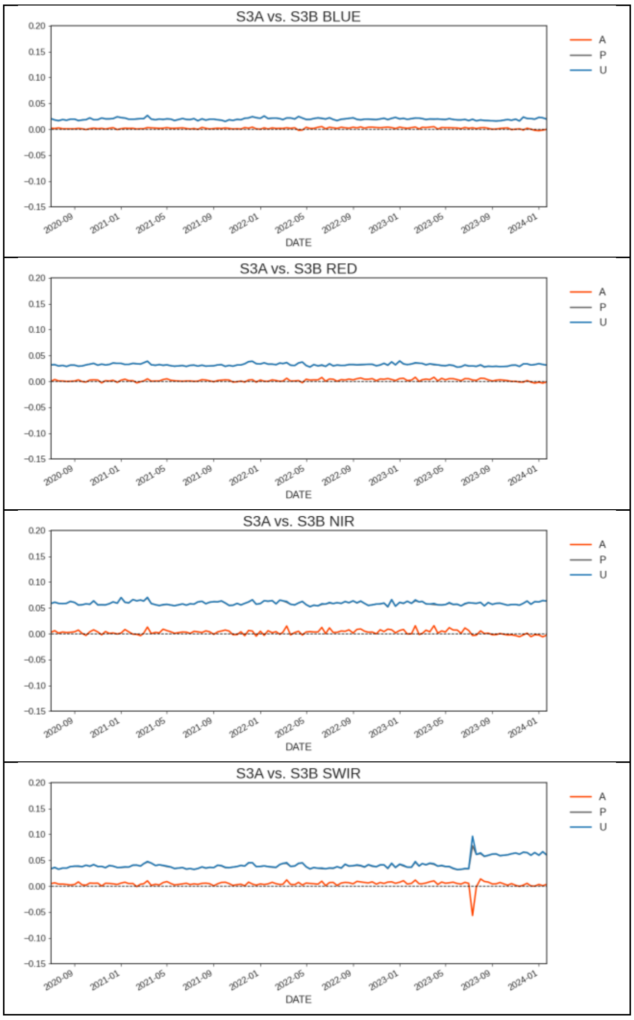

Figure 97: Temporal evolution of APU statistics between S3A_SY_2_V10 and S3B_SY_2_V10 for BLUE, RED, NIR and SWIR bands (top to bottom), January/2021 – January/2024

References

[1] B. Fuster *et al.*, “Quality Assessment of PROBA-V LAI, fAPAR and fCOVER Collection 300 m Products of Copernicus Global Land Service,” *Remote Sens.*, vol. 12, no. 6, p. 1017, Mar. 2020, doi: 10.3390/rs12061017.

6.3 SYN L2 AOD NTC products

Adjustment of the FMI matchup tool for Sy_2_AOD validation

The FMI matchup tool for AOD validation with AERONET was adjusted for Sy_2AOD product validation to fulfil the need to use this tool in cloud screening (cloud post-processing) exercise.

Macro-pixel created by FMI includes all pixels within radius of 0.25° (a surface of ca. 50 km × 50 km in the low and middle latitudes) around AERONET station. Measure in degrees is chosen because FMI matchup tool has been developed to be adjustable for satellite products with different spatial resolution. Thus, the potential number of pixels in FMI matchups is slightly changing. It may be as high as 140 (Figure 98: histogram of the number of satellite pixels enclosed in the 0.25° area of the match-up process) if the matchup area is fully within the satellite overpass, or lower on the edges of the swath.

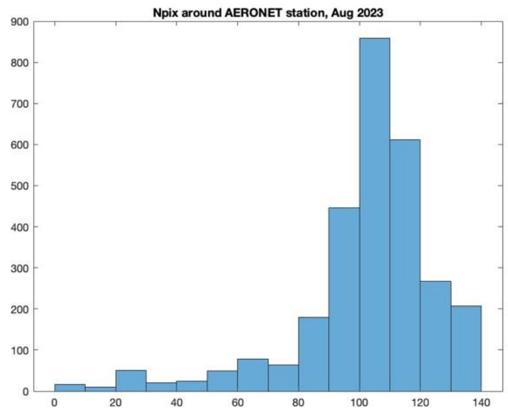

Figure 98: Histogram of number of satellite pixels in FMI matchups (±0.25°) with AERONET, for August 2023

Presence (within a matchup) of cloud-screened pixels, as well as not retrieved pixels (flagged for another reason than cloud contamination) lower considerably the number of Sy_2_AOD pixels (per matchup) classified for validation (Figure 99).

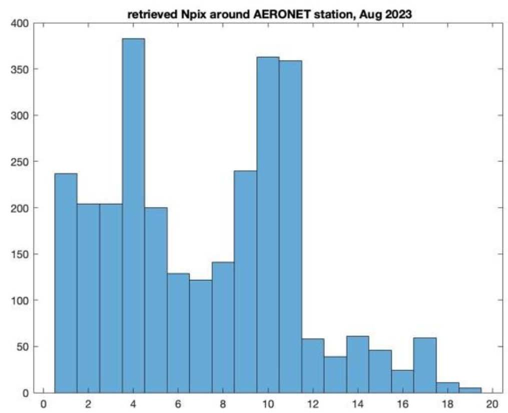

Figure 99: Histogram of valid satellite pixels retrieved in FMI matchup (+- 0.25°) area. For August 2023

Analysis of the number of pixels per matchup has been performed for FMI matchups.

In August 2023, number of the retrieved SY_2 AOD pixels per matchup did not exceed 20. For 12% of all matchups, the number of the retrieved SY_2 AOD pixels per matchup was between 12 and 19, for 64% the number of the retrieved SY_2 AOD pixels per matchup was below 10 (for ca 15% - below 3).

Such an unexpectedly low number of retrieved (per matchup) pixels brought an alarm to consider a lower limit (number to be tested) of the retrieved pixels per matchup in order to improve representativeness of the SY_2 AOD and remove matchups with low Sy_2 AOD coverage from the validation exercise.

How number of retrieved (per matchup) pixels influence validation statistics

For Aug-Dec 2020 we tested how a number of retrieved (per matchup) pixels influence validation statistics. A clear improvement in validation statistics is seen when the lower number of retrieved pixels per matchup is set to 3 (Figure 100).

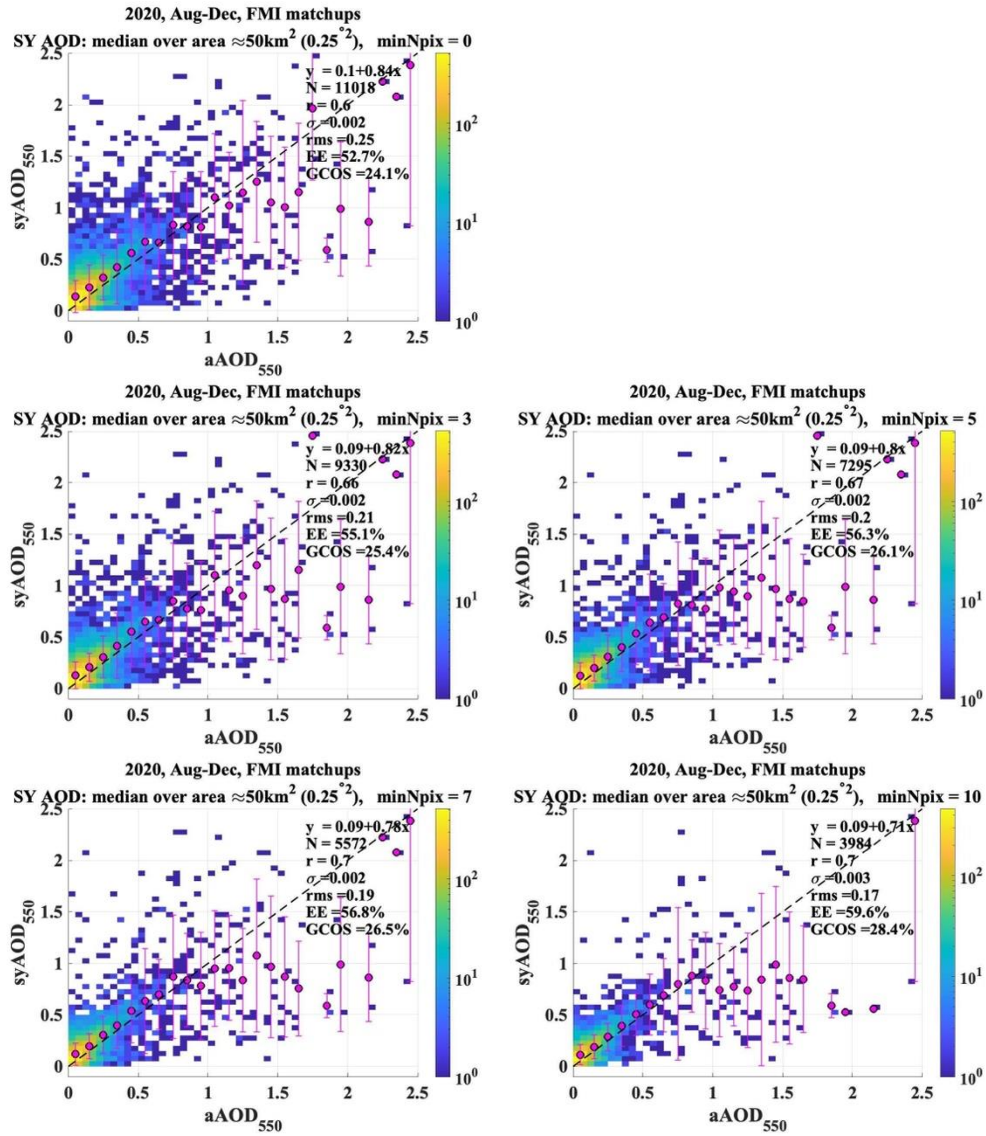

Figure 100: Dependence of validation results on minimum number of required Sy_2 ADO pixels (minNpix in each figure title) around AERONET matchup. For 2020, Aug-Dec, FMI matchups. Note that density (number of matchups per bin) is shown in logarithmic scale. Validation statistics are provided (offset and slope from the linear fit, N – number of matchups, r – correlation coefficient, σ- standard deviation, rms – root mean square error, EE – number of pixels in the MODFIS error envelope defined as ±0.05±0.2*AOD, GCOS – fraction of matchups which satisfy GCOS requirements of 0.03 or 10% of AOD).

Correlation coefficient (r) increased from 0.6 to 0.66; rms lowered by 0.04, bias lowered by 0.01, number of pixels which fit to MODIS error envelope (EE) and satisfy GCOS requirements increased.

With applying minNpix = 3 criteria, the number of matchups has decreased by 16% (from 11018 to 9330) and became close to the number of ACRI matchups (9965).

Visual inspection shows that application of minNpix criteria influence more the removal of the overestimated syAOD, while “cloud” of underestimated syAOD remains unchanged. This allows to conclude that minNpix criteria exclude possibly cloud contaminated cases, where syAOD is overestimated.

An increase of minNpix criteria (to 5, 7, and 10, Figure 100) slightly improves validation statistics, but at the same time leads to decreasing the number of matchups and representativeness of the validation results. Thus, minNpix=3 seems to be reasonable to be applied in the validation exercise. On the other hand, improvement in cloud screening (i.e. removal of cloud contaminated pixels) will make an application of this criteria less important.

<u>Inter-comparison of the Sy_2_AOD product before and after implementation of TOA corrections coefficients.</u>

TOA corrections coefficients were included in the retrieval chain in summer 2023.

Here we intercompare validation results for three periods: Aug-Dec 2020, Aug-Dec 2021, Aug-Dec 2023 (Figure 101). For all three periods, validation was performed by utilising matchups created at FMI; minNpix criteria discussed above was not applied in this exercise.

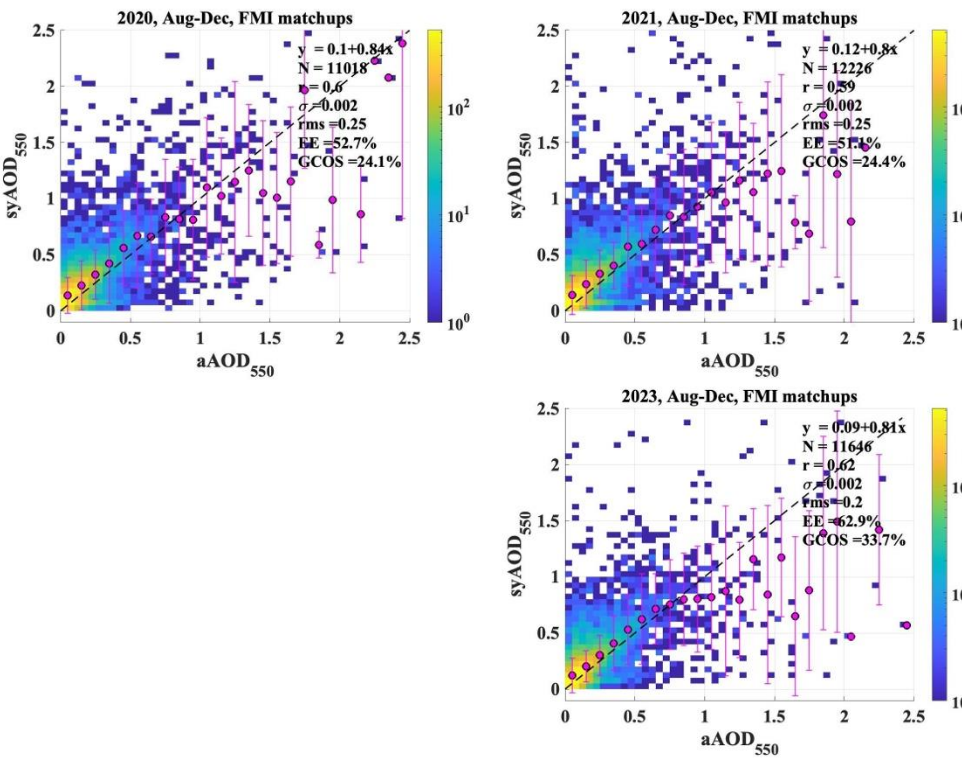

Figure 101: Scatter density plots for syAOD vs aAOD for years 2020, 2021 and 2023, months Aug-Dec. Note that density (number of matchups per bin) is shown in logarithmic scale. Validation statistics are provided (offset and slope from the linear fit, N – number of matchups, r – correlation coefficient, σ- standard deviation, rms – root mean square error, EE – number of pixels in the MODFIS error envelope defined as ±0.05±0.2*AOD, GCOS – fraction of matchups which satisfy GCOS requirements of 0.03 or 10% of AOD).

Application of the TOA correction coefficients allowed to improve SY_2_AOD product.

R increased from 0.60/0.59 (for years 2020/2021) to 0.62 (2023); bias lowered from 0.1/0.12 to 0.09; rms lowered by 0.5. Number of pixels which fit to MODIS error envelope (EE) and satisfy GCOS requirements increased by ~10%.

Lowering of the syAOD has twofold effect. In the low AOD range (most of the retrieved pixels fit to this range), where syAOD offset to aAOD was positive, lowering of AOD lead to decreasing of the syAOD offset (Figure 102, left). In the high AOD range, where syAOD offset to aAOD was mostly negative, lowering of AOD lead to increasing of the syAOD offset (Figure 102, right).

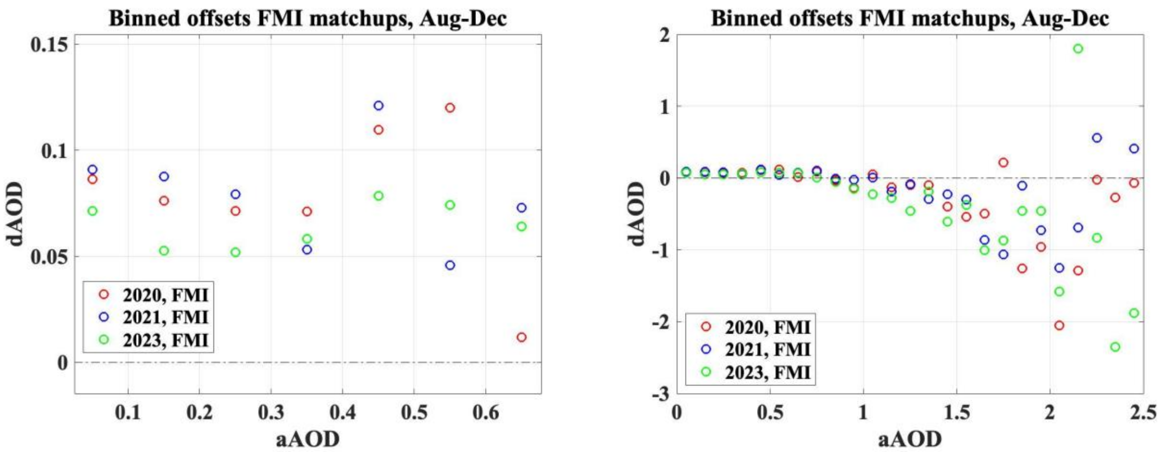

Figure 102: For Aug-Dec of 2020 (red), 2021 (blue) and 2023 (green), Sy AOD offsets (dAOD, binned to Aeronet AOD, aAOD) for matchups created by FMI. Left : results for aAOD ∈ [0, 0.65]. Right : aAOD ∈ [0, 2.5].

7 Events

For OLCI-A, three Radiometric Calibration sequences have been acquired during the reported period:

- S01 sequence (diffuser 1) on 11/01/2024 20:21 to 20:22 (absolute orbit 41153)
- S01 sequence (diffuser 1) on 26/01/2024 13:47 to 13:49 (absolute orbit 41363)
- S05 sequence (diffuser 5) on 26/01/2024 15:28 to 15:30 (absolute orbit 41364)

For OLCI-B, one Radiometric Calibration sequences has been acquired during the reported period:

- S01 sequence (diffuser 1) on 13/01/2024 15:27 to 15:29 (absolute orbit 29785)

8 Appendix A

All Data Quality Reports, as well as past years Data Quality Reports and Annual Performance Reports, are available on dedicated pages in Sentinel Online website, at:

- https://sentinel.esa.int/web/sentinel/technical-guides/sentinel-2-msi/data-quality-reports
- https://sentinel.esa.int/web/sentinel/technical-guides/sentinel-3-olci/data-quality-reports
- https://sentinel.esa.int/web/sentinel/technical-guides/sentinel-3-slstr/data-quality-reports
- OPT Annual Performance Report Year 2022 (PDF document)

End of document